LOW VELOCITY TRANSVERSE IMPACT OF FILAMENT WOUND E-GLASS/EPOXY RESIN PIPES.

Thesis submitted in accordance with the requirements of the University of Liverpool for the degree of Doctor of Philosophy.

by Kim Ainsworth April 1990.

ABSTRACT.

Transverse low velocity (up to 30m/s) impact tests have been performed on filament wound E-glass/epoxy resin pipes with a winding angle of ±55° over a range of impact energies and velocities. The majority of these were drop-weight tests performed on 150mm internal diameter pipes either floor-supported along the pipe's length or supported in specially designed cradles. The damage caused was analysed both non-destructively and destructively to characterise the failure process.

Equivalent static tests were performed in both support geometries to see if any correlations existed, which would allow simple static tests to be used to predict the impact performance of the pipes. This was possible over the majority of the energy range considered for the cradled geometry but not for the floor-supported geometry, due to the different degrees of transverse deformation induced in these specimens.

Tests were conducted on 400mm internal diameter pipes, with static tests providing additional information on the failure processes and pipe drop impact tests producing similar failure patterns to those seen in the drop weight tests.

Tests on pipe sections were conducted to see if correlations between them and full pipe tests existed, leading to a possible further simplification of the testing process. This work has indicated that this may be possible, with very small pipe sections showing similar trends to the cradled full pipes. This should be

investigated further.

Experimental information has been complemented by use of finite element analysis and simple mass-spring models. These techniques have allowed the displacement in the pipe up to the end of elastic behaviour and the transient load/time behaviour to be well predicted.

ACKNOWLEDGEMENTS.

I would firstly like to thank my supervisor Dr. K. E. Evans for all his considerable help and patience throughout the duration of this project and also Mr. P. R. Marks, my industrial supervisor, for his help in the large pipe testing and computing. I acknowledge the financial support of the SERC and of Shell Research through a CASE award.

Many friends and colleagues have helped me during this work, but I would especially like to thank the following. I have received considerable help from the workshop and from Mr. Chris Jackson in the Department of Materials Science and Engineering. From the Impact Research Centre, Dr. Bob Birch wrote the software for the analysis of the impact data and helped during the tests, as did Mr. Chris Worrall, who also did as much of the heavy lifting in the project as I could persuade him to do! The single bounce mechanism was designed by Mr. John Curren, also from the Impact Research Centre. I would also like to thank Mr. Willy van Laar and Mr. Mike Fitton of Shell Research for their help in performing the experimental work and Shell's Photographic Department for figs. 5.2, 5.6 and 5.13.

On a more personal note, I would like to thank all my family for their love and encouragement over the last 24 years and my fiancé Andy, who had to put up with me during the drawing of the diagrams - no mean feat! Liverpool has been a wonderful city to study and live in and I have thoroughly enjoyed my time here. I would also

like to acknowledge the role of Liverpool football team, who have inspired me when research couldn't.

Finally, the first half of 1989 was not a particularly good time for me and I would like to mention here the people whose love and support enabled me to finish this thesis. Thanks are due to Ken, Patsy, Anne and Geoff, Mark, all my family and especially to Andy.

This Thesis is dedicated to the memory of
the 95 who died at Hillsborough
April 15th, 1989.
"You'll Never Walk Alone."

AUTHOR'S PUBLICATIONS.

1. Ainsworth, K.L. and Evans, K.E.: "Transverse impact of filament-wound pipes", Composite Structures 5, Elsevier, (1989), p333-345. (Ed. by I.H. Marshall).
2. Ainsworth, K.L. and Evans, K.E.: "The measurement and modelling of filament wound pipes undergoing transverse impacts", Proc. 4th International Conference on Fibre Reinforced Composites, Inst. Mech. Eng., (1990), p143-148.

LIST OF CONTENTS.

Page no.

LIST OF FIGURES.

Page no.

Chapter 2.

Chapter 3.

Chapter 4.

Chapter 5.

Chapter 6.

Page no.

Chapter 7.

Page no.

Chapter 8.

LIST OF TABLES.

Page no.

Chapter 4.

Chapter 5.

Chapter 6.

Page no.

Chapter 7.

1. INTRODUCTION.

Prior to 1967, most cargo and ballast piping aboard marine crude oil and cargo vessels (1) was fabricated from statically cast, grey flake cast iron. This system did work well, but the need for cheaper, large diameter piping led to it being replaced by spun-cast spheroidal graphite (SG) cast iron piping. However, problems soon arose with the new SG iron piping due to the very hostile environment in which it was used, with continual exposure to extremes of temperature, direct sunlight, severe weather conditions, salt spray and green seas (2). These led to both internal and external pitting, which in turn led to progressive weakening and leakage from the pipe systems (3), causing the SG iron pipe to need replacing within two service years. Thus a new pipe system was required.

Three alternative piping systems were considered as replacements (1):-

a) painted steel - this can be used without corrosion but is very dependent on the standard of steel, the paint application and the care taken to avoid coating damage during transport and fitting. Once fitted, painted steel pipes must be checked regularly as when the coating fails, leakage occurs.

b) 1% chrome spun-cast steel - these are less susceptible than spun SG iron to pitting attack, but are not immune.

c) glass fibre reinforced plastic (GRP) - this is considered a better prospect than both the above, with the following being the two main advantages of using GRP pipes:-

i) they are lightweight and highly durable, which leads to improved economics, i.e. reduced maintenance costs, easier and cheaper installation and increased cargo dead weight capacity.

ii) they show very good corrosion resistance, which reduces the rate of leakage and thus reduces environmental pollution. This improved corrosion resistance also results in improved safety, since emergency services are not rendered inoperable by undetected corrosion.

Although the discussion so far has concerned only shipboard use of GRP pipes, the advantages listed above have led to increased usage of GRP pipes in many industrial areas. These include the chemical processing industry, tunnel and pipe linings, sewage and drainage and pressure piping, including water distribution (4).

The pipes selected for shipboard trials - and thus used in this project - were filament wound E-glass/epoxy (epikote 828) resin pipes with a winding angle of ±55°, and were fabricated by Wavin Repox B.V.(5). All these materials and conditions were specially selected to enhance the pipe properties, and the reasons for their choice are given below. E-glass rovings are the most common type of reinforcement and were used because of their good water corrosion resistance and reasonable costs (6). Epoxy resins, basically any molecule containing more than 1 α-epoxy group capable of being converted to a useful thermoset form, are the strongest of the common polymers and the first choice of matrix for most high-pressure fibreglass pipes, especially when accompanied by high temperature requirements (6). This is due to their properties, such as low viscosity, low shrinkage, high adhesive strength, mechanical properties and electrical resistance and good chemical resistance (7). The latter is superior with alkalis and solvents, but is also good with acids. Filament winding was used as the manufacturing method as it is the most important way of producing low-cost, high-strength corrosion resistant equipment. The filament winding process (2) begins with the glass fibres, which are soaked in epoxy resin, being wound at an angle round a large, smooth steel mandrel. When the required number of layers have been wound, the mandrel is moved into an oven and the wet pipe is cured. On cooling, the finished pipe slides freely from the steel former, its inside being extremely smooth. For these pipes, a winding angle of ±55° was used. This is used to give the pipe twice the hoop strength compared with axial strength, which is the normal stress condition under biaxial pressure and is a highly efficient use of fibreglass reinforcement (8).

Once the pipes had been constructed, the next stage was to assess their performance aboard ship. Such trials have been underway since May 1975 (1), covering applications such as part of the stripping system (May 1975) and part of the cargo-ballast system (1977). The former trial worked well, with the pipes remaining in perfect condition during a service life of 30 months, whilst the latter also worked well after initial failure due to inadequate wall thicknesses was encountered. This led to implosion, but was overcome by ring-stiffening and subsequent respecification.

The next step (1984-5) was to assess the performance of GRP pipes on deck. The purpose of this was to determine if the structures were able to withstand green-sea forces ("sea-slap") experienced during bad weather (2). This system - which was all GRP except for stainless steel securing bolts and bracket strap end fittings - was successfully on trial for 6 months on the upper deck of a shuttle tanker, Norissa, operating in the exposed waters of the northern North Sea. This initial trial worked very well, and only needed in situ maintenance (3).

The final stage was to fabricate and assess an all GRP piping, support and walkway system, which was designed in-house. Guiton (3) reports that at the time of writing his paper, this system had been used at sea for 6 months with no problems. However, it should be noted that at that stage, there had been no green-sea loadings.

Although the maintenance of structural integrity under green sea loading conditions is an essential requirement for pipes and support systems (3), other requirements of equal importance are adequate fire (9) and low velocity impact resistance. This project is concerned with the latter. At this stage, it is worth explaining what is meant by a low velocity impact. This is defined as one with a velocity low enough to justify static analysis of the response of the structure (10) and thus does not have a standard velocity range, being very dependent on the particular impact system under test. As will be seen, for this project the term low velocity impact covers impacts with speeds less than 30m/s.

Low velocity impacts are of importance since they arise from situations such as accidental dropping of the pipe itself or of hand tools onto the pipe. A dropped spanner, for example, leads to localised areas of damage such as delamination, matrix cracks and fibre fracture. These are often difficult to detect with the naked eye and can lead to premature catastrophic failure, with reductions in residual tensile and compressive strength of up to 50% (11), (12). It is, therefore, important to assess the extent of such damage and its effect on pipe properties and this forms the basis of the aims of this project. The possibility of correlations between static and impact tests is also considered. Such correlations, if they do exist, will allow simple static tests to be used to predict the performance over a range of impact velocities and energies. The damage is also quantified by using finite element modelling to predict the displacements in the pipe up to the end of elastic behaviour on the basis of a quasi-static approximation and by simple mass-spring systems which model the transient load/time behaviour, and comparisons of both these methods with experimental results is also considered.

This first chapter serves as a brief introduction to the project. Chapter 2 reviews the literature concerned with the techniques involved, with particular emphasis on low velocity impact testing of composite materials. Chapter 3 explains the experimental methods common to a majority of the tests carried out (i.e. static testing, impact testing, both destructive and non-destructive damage analysis and quality assessment). The next three chapters look at the individual test details and results from testing pipe sections (chapter 4), large diameter pipes (chapter 5) and small diameter pipes (chapter 6), where large diameter pipes had an internal diameter of 400mm and small diameter pipes an internal diameter of 150mm. Chapter 7 is concerned with the two modelling methods i.e. finite element and dynamic analysis, as already discussed above. Chapter 8 acts to draw together all the information gathered both experimentally and analytically and discusses the results, leading to the conclusions and indications for future work listed in chapter 9.

2.LITERATURE REVIEW.

This chapter begins with a review of the literature concerned with the techniques involved in this project (i.e. impact testing, non-destructive testing in the form of X-ray radiography and backlighting, and both analytical and computer modelling), all applied to composite materials. This is followed by a study of previous work on low velocity impact testing of composite plates and cylinders, the particular concern of this work.

2.1 Impact testing.

2.1-1 Charpy and Izod tests.

Until recently, the tendency in impact testing was to perform Charpy or Izod tests on standard specimens fabricated from the composite under test. For example, Charpy tests have been conducted on standard specimens by Novak and DeCrescente (13) and Yeung and Broutman (14), who performed instrumented tests on unnotched specimens to relate the glass-resin interfacial strength to the transverse impact strength of the laminate. Chamis, Hanson and Serafini (15) and Therberge and Hall (16) used Izod tests, the latter also performing tensile-impact tests.

However, Charpy and Izod tests have been strongly criticised since the 1960's (17), with the following being examples of the general objections raised:-

i) the specimen contains a sharp notch and so the results are strongly dependent on the energy for crack propagation. In practise, behaviour depends more on the energy needed for crack initiation.

ii) the results depend on details of the test method and therefore the test may be inaccurate and have poor reproducibility.

iii) the test is arbitary. The rate of tests, specimen shape and method of stressing are all held constant and there is no reason to expect that the results will represent behaviour under different conditions.

iv) Charpy and Izod tests give no indication of the residual properties after impact (18).

v) particularly with glass/epoxy composites, Charpy tests are noted as being unsuitable (19) since the material may not be sensitive to notches.

A further objection in the case of testing pipes by Izod or Charpy tests is that testing a standard specimen taken from a pipe is not necessarily representative of the effects of impacting an entire pipe.

Therefore, other impact techniques are now employed and these are discussed below.

2.1-2 Drop weight impact testing.

The impact technique now most frequently used is to conduct drop weight tests. A variety of materials have been tested by different groups of workers. Considering firstly tests conducted on flat laminates and plates, the following are examples of the work carried out. Boll, Bascom, Weidner and Murri (20), Cantwell and Morton (21) and Cantwell, Curtis and Morton (22) all studied low energy or low velocity impact tests on carbon fibre laminates and all used a spherical impactor nose. Caprino (23) also studied the impact of carbon fibre laminates, but modified the falling weight rig so that the tup was caught on its first rebound to ensure single bounce impacts were carried out . In this case, the tup had a hemispherical nose. Dorey, Sidey and Hutchings (24) studied the impact properties of a carbon fibre/Kevlar 49 fibre hybrid composite using both drop weight impact tests and gas guns, and compared the two techniques (see section 2.1-3). Drop weight impact tests carried out on glass fibre laminates and plates have been performed by Verpoest, Marien, Devos and Wevers (25) and Myers (26).

Other groups of workers have compared impact damage induced by drop weight tests on different composite systems. For example, Rotem (27) looked at the differences between impact on carbon/epoxy and glass/epoxy laminates, whilst Caprino, Crivelli Visconti and Di Ilio (11) compared three different types of composite plates - glass cloth/polyester, carbon cloth/polyester and nylon cloth/polyester.

Although the above is of interest, the geometry required in this work is cylinders, pipes and tubes. There are two standards which deal with the impact of these specimens. The British standard (28) deals with the design and performance requirements of GRP pipes and fittings for use in the water and sewage industries, and is concerned with weepage through the pipe wall when the impacted pipe is under internal pressure. The pipe is impacted eight times (at 300mm intervals) at two different internal pressures and then the pressure is increased up to 1.5 times the maximum service pressure for 168 hours before the pipe wall is examined for weepage. The American standard (29) gives the test method for determining the impact resistance of thermoplastic pipes and fittings by means of a tup. Failure in this standard is defined as shattering or any crack or split created by impact and seen by the naked eye, e.g. creases visible on the surface do not constitute failure. It should be noted that this test is considered to be neither precise nor accurate unless very large numbers of specimens are used (between 120 and 170 is suggested!), which is a distinct disadvantage in the use of this method.

In contrast to the testing of flat laminates and plates, very little research work has been conducted on impact of composite pipes, even though as long ago as 1963 JM Cann was investigating the impact resistance of rigid PVC pipes. He assessed two falling weight test methods (namely the probit and staircase methods) (30) as well as investigating the effects of varying the temperature, speed of impact and specimen geometry (31). More recently, Lloyd and Knight (32) looked at low velocity impact of carbon fibre filament wound pressure vessels. They used a drop weight impact tester with a 12.7mm diameter hemispherical head, achieving impact energies in the range 0·96 to 2·36J (and thus velocities varying from 1.07 to 2.74m/s).

The most relevant research to this project was carried out by Christoforou, Swanson, Ventrello and Beckwith (33) and by Christoforou and Swanson (34). They examined lateral drop impact tests on carbon/epoxy cylinders supported completely along their lengths by specially designed wooden cradles. The cylinders had diameters of 96.5mm, wall thicknesses of 1.52mm and masses of 0.32kg whilst the impactor had a mass of 5kg. Both experimental and related modelling work was carried out and will be discussed in section 2.4 (as indicated above).

2.1-3 Other impact techniques.

Although the drop weight method is the most widely used, other techniques are also documented which achieve low velocity impact, and some of these are considered in the following.

A large number of workers have used gas guns, which fire a projectile at the specimen under test. The projectile shape is varied according to the requirements of the particular tests and the capabilities of the gas gun systems. Sharma (12) and Joshi (35) both used spherical projectiles with a diameter of 12.7mm to impact sandwich structures and carbon/epoxy laminates respectively. Malvern, Sun and Liu (36) impacted Kevlar/epoxy and carbon/epoxy laminated plates with a flat-ended steel cylinder of length 25.4mm, diameter 9.5mm and mass 14.6g. The above were all blunt impactors, thought to best simulate dropped tool damage (see chapter

1) and Sheldon (37) compared the effects of such impactors with very sharp projectiles on graphite/epoxy laminates. As already mentioned above, Dorey, Sidey and Hutchings (24) compared the impact damage induced in a carbon fibre/Kevlar 49 fibre hybrid composite using drop weight and gas gun apparatus. They performed equivalent energy tests in the two cases, with their gas gun projectile being a 6mm diameter steel ball. After test, the residual flexural strength of the specimens was measured and was found to be greater in the specimens initially tested by the gas guns. This they explained by saying that the drop weight tests produce more compressive damage on the front surface of the specimen whereas in the gas gun tests, the smaller ball moving at higher velocities causes less bending and dissipates more energy in multiple fractures parallel to the fibres, therefore having less effect on the flexural strength.

Another technique in common use to perform low velocity impacts involves using a swinging pendulum of known kinetic energy. Sjöblom, Hartness and Cordell (10) used this apparatus to compare the impact properties of graphite with both an epoxy and a thermoplastic matrix, and list the following advantages of the system. Single bounce impacts are very simply achieved, it is easy to accurately control and vary impact energies at low velocities, small energy drops can be achieved and velocities can be predicted easily to an accuracy of 1%. Maass and Hoon (38) also used this type of system to assess the survivability of glass reinforced lightweight man-portable tactical direction finding antennae. Their impactor was a 12.7mm diameter steel ball and they were able to achieve energies up to 11·60J and velocities up to 4.87m/s.

Two further techniques which have been used are "bump" and "punch" tests. Bump tests were performed on (amongst other geometries) filament wound glass fibre pipes by Peraro (39). The impact tester used consisted of a horizontal hydraulic ram with a velocity range from 0.0127m/s to 12.7m/s and the impactor was a 12.7mm diameter hemispherically tipped rod. Peraro says this apparatus is more flexible than the traditional falling-weight machines as far as achieving low velocities is concerned. The tests also allowed one impact to be carried out without the problem of rebound which is found in the single bounce tests. Graves and Lagace (40) performed punch tests on pressurised graphite/epoxy cylinders with dimensions of 610mm (length) by 305mm (diameter) with a wall thickness of 1.4mm. The test procedure was to pressurise the pipe and then, using a guillotine mechanism, puncture it with a blade of known size. If the cylinder did not fail, it was depressurised, patched up and then repressurised. The next largest blade was then used to puncture the cylinder away from the original region and the procedure was repeated until failure. This procedure could be easily adapted to simulate dropped tool damage by using a blunt indentor in place of a blade.

At this point, it is worth mentioning work carried out by various groups at the University of Surrey (41), (42), (43) who have developed a method of simulating impact damage in filament wound GRP tubes. They found that the deformation and damage caused by slow indentation tests was identical to that produced by low velocity (up to 10m/s) drop weight impact testing and so used a fully instrumented slow indentation method to monitor deformation. The procedure used was to measure the strain distribution on the tube wall by means of electrical resistance strain gauges. An indentation grid was drawn up and then systematically a full strain distribution built up.

Many of the above pieces of research work used instrumentation in conjunction with the impact apparatus so that data could be obtained during the test. The most widely documented technique is laser-doppler velocimetry, which provides a direct method of measuring the changing velocity of the projectile with respect to time (44). After the initial velocity/time signal has been filtered to separate the specimen response from the electronic noise and impactor response (45), it is then possible to use the data to obtain force/time, force/displacement and energy/displacement plots (46). The major error in this technique is the possibility of energy transfer to the anvil of the machine rather than to the specimen. However, this is not considered significant for low energies and velocities.

2.2 Non-destructive testing techniques.

Once the composite has been tested, there are several difficulties associated with the detection and identification of flaws (in this case delamination, fibre fracture and matrix cracks) which may be introduced. These difficulties have three main causes:-

i) the heterogeneous and layered nature of the material

ii) the sensitivity of the material to out of plane stresses (47)

iii) the process by which composites accumulate damage (which is by the initiation of a myriad of small matrix cracks).

The matrix cracks lead ultimately to the development of delaminations and this point is defined by Proulx, Roy and Zimcik (48) as the end of the useful life of the composite.

There are several non-destructive techniques which can be used to detect and monitor developing damage and to assess the effects of the damage on the capabilities of the material to maintain its design stiffness, strength and lifetime properties (49). The two techniques best suited to this project are considered below, although it should be noted that no single technique as yet gives a complete picture of the damage sustained (50) so in practise a combination of techniques should always be used to fully assess the damage.

2.2-1 X-ray radiography.

This provides a good overall view of the fibre reinforced composite under consideration and it can be used for detecting features such as porosity, foreign objects, translaminar cracks and general fibre orientation (51). Normally, a commercially available low voltage beryllium window X-ray generator is used. A high tube voltage between cathode and anode causes electrons to accelerate and strike the target, thereby causing emission of X-rays (52). The beam of penetrating radiation is typically directed perpendicularly towards the part under inspection at a fixed-focus film distance. A portion of the energy is absorbed as it passes through and a portion is scattered (depending on the material composition, thickness and density). The currents are usually held to a few milliamps and the exposure to about a minute.

To get the maximum amount of information from the test specimens, the material can be impregnated with a solution of a high atomic number compound. Then, differential absorption of the X-rays will improve the contrast on the resultant radiograph and greater resolution of the structure will be obtained. The steps involved in the impregnation process are listed by Rose and Shelton (53) as follows:-

i) prepare the specimen by removing surface contamination (e.g. use a hair drier)

ii) soak or brush on the X-ray opaque fluid for a period of time significant to allow penetration into cracks or pores

iii) X-ray the impregnated specimen

iv) remove the impregnant from the specimen

The first solution to be used as an impregnant was tetrabromoethane (TBE) (53), (54). Although this works very well, it is a severe poison and is classed as a potent mutagen. Also, TBE is a possible solvent for the resin matrix (55). Therefore, it was necessary to find another X-ray opaque fluid.

The next fluid to be tried was 1-4 diiodobutane (DIB) (56). This is less X-ray opaque than TBE but has the advantage that it is safer to use. However, DIB is still not ideal, being classed as an irritant.

In 1980, Rummel, Tedrow and Brinkerhoff (57) developed a zinc iodide based solution for use on graphite/epoxy specimens. This was an improvement on the organic fluids used since no specific handling precautions are needed. Other advantages for its use are its surface wetting properties, image contrast properties, ease of mixing, capillary properties and ease of removal (i.e. it is necessary only to soak the specimen in water to remove the penetrant). The solution used consists of 60g of zinc iodide dissolved in 10ml of water, 10ml isopropyl alcohol and 1ml photoflo. The alcohol and photoflo are added to improve the penetration, as the alcohol means the solution has both polar and non-polar solvent properties, whilst the photoflo is a linear alcohol alkoxylate used as a wetting agent to reduce the surface tension of the solution.

The series of tests Rummel, Tedrow and Brinkerhoff conducted was very extensive. They began by making a comparison with other X-ray opaque fluids which showed favourable results for the new zinc iodide solution. Then, they conducted a series of impact tests using energy levels varied from 0·05 to 0·9J and also a series of fatigue tests (the latter to study damage accumulation), observing the enhancing power of the zinc iodide penetrant throughout these two sets of tests. Finally, they conducted 6 weeks of tests to show that no change or degradation of any of the specimens could be attributed to exposure to the penetrant.

Other groups have used a zinc iodide solution (49), (58), (59) and found it to be suitable as an aid to damage detection. Elber (60) also used a zinc iodide penetrant and to make sure the composite plates he used were completely penetrated, he added the solution before testing to ensure reduction of the number of air pockets formed. Although Stone and Clark (61) say the zinc iodide is the only feasible inorganic penetrant, there are a few mentions in the literature of other X-ray opaque fluids under development e.g. Henneke and Russell (49) mention a gold chloride solution, Scott and Scala (62) say that lead oxide in gelatine has been used and Shelton and Marks (63) used saturated barium chloride.

There are some problems associated with using an enhanced X-ray radiographic technique. Stinchcombe (58) explains the difficulties which may be associated with interpreting the X-ray data:-

i) the penetrant may not infiltrate all the matrix cracks and delaminations. This can be remedied by using an additive in the fluid to reduce its surface tension (i.e. the photoflo in the zinc iodide solution)

ii) large delaminations may not be completely resolved even though the penetrant can wet the debonded regions. The delamination surfaces open leading to capillary action driving the penetrant to the boundary of the delamination. This leaves a large debonded region void of penetrant and means that the radiograph shows only the boundary of the delaminated regions.

iii) the orientation of the defects is crucial which is an added complication in interpreting the radiograph.

However, the main problem with the technique is that although detailed information is obtained on the nature and planar distribution of the material damage, no information is obtained on the through-the-thickness distribution of the damage.

2.2-2 Backlighting technique.

This is a very useful technique which simply involves placing a strong light source behind the damaged surface. It is able to detect the presence of opaque foreign material and small air bubbles as well as mapping the damaged area. Murphy and Mitchell (50) list the following principal advantages of the technique:-

i) there is a fair degree of success in the detection of defects

ii) interpretation is easy

iii) there is a low probability of labelling as defective a non-defective area

iv) it is quick and can be used in the field

v) the cost is very low

Caprino, Crivelli Visconti and Di Ilio (64) investigated the capabilities of the technique at low levels of damage on impacted glass cloth/polyester panels and saw evidence of failure even at their lowest impact velocity of 1m/s. This is an improvement on the penetrant-enhanced X-ray radiography technique detailed above which is poor at detecting low levels of damage. This is because the specimen surface has to be damaged enough to allow penetration of the penetrant for internal damage to be clearly seen. A further advantage of the backlighting technique is that it does provide through-the-thickness information by revealing delamination patterns formed between the different layers of the specimen under test. Backlighting has also been successfully used on glass/epoxy plates (65), (66), filament wound glass fibre pipes (39) and Kevlar/epoxy plates (36), although it is unsuitable for use with carbon fibre composites.

2.3 Modelling.

This section reviews attempts to model both the stress distributions in fibre reinforced composites under various relevant loading conditions and the transient load/time behaviour in composites during impact.

2.3-1 Modelling the stress distributions.

Before progressing to investigate analytical work carried out on the cylindrical geometry, some of the more interesting and relevant work on modelling laminates is worth considering. Gosse and Mori (67) looked at low velocity, transverse impact damage in graphite/epoxy laminated plates. In particular, they were interested in the application of the relationship between strain and material organisation to relate crack initiation to subsequent delamination development and propagation. This relationship is refered to as the K-rule. To understand this proposed mechanism of delamination initiation, qualitative stress analysis was employed to see how the resolved shear stresses and strains create damage, the stress and strain distribution being used to describe the resultant internal damage. Using this analytical method, Gosse and Mori found that their K-rule predictions of internal damage patterns agreed well with the actual damaged state determined experimentally. Tiu, Gott and Breckell (68) investigated whether static finite element analysis coupled with the appropriate failure criterion could predict the values of the impact threshold energy of IM6/6376 composite laminates. They hoped to use this model to predict both the extent of damage after impact and the residual strength of the laminate. The laminate was modelled using thick plate elements which can handle bending and shear, but the energies obtained from the finite element modelling were lower than the experimental values. They say this is because, unlike experiment where a certain critical value must be reached, in the model, buckling instability occurs as soon as the laminate is damaged. Finally, Ross, Malvern, Sierakowski and Takedo (65) aimed to determine analytically the interlaminar shear stress of a $[0_5/90_5/0_5]$ glass/epoxy 15.24cm square plate when subjected to a central impact of 45.7m/s. The impactor was a cylindrical steel projectile 0.97cm in diameter and 2.54cm long. Their analysis was performed using SAPIV (a finite element package) which includes a 3-D elastic-orthotropic material model with dynamic analysis capabilities, which allows calculation of the transverse shear stress directly. Among the successes of their analytical model was the prediction of the non-symmetrical nature of the delamination.

Turning now to the modelling of cylinders, much of the work has been carried out on orthotropic shells (which are a special case of anisotropic shells where the planes of orthotropy correspond to the geometric axes) (69). Chao, Tung and Lee (70) looked at the problem of the impact responses of orthotropic shells subjected to special forms of loading suddenly applied to the outer surface of a cylinder, which was simply supported at both ends. Having developed the equations for general dynamic response, they considered six forms of impact loading, i.e. a concentrated load, a line load along a longitudinal segment, a line load along a circumferental segment, a load over a small area, an impulsive load and moving a load across the span. They then used the dynamic response to get the stress levels in the cylinder via strain components. To assess their model, they reduced it to the isotropic case and found it compared favourably with theory. Work by Chang and Kutlu (71), (72) and Christoforou et al (34), (73) has investigated including non-linear effects of failure into modelling. Chang and Kutlu developed a progressive model to analyse cylindrical shells subjected to out-of-plane loadings. This model consisted of structural analysis (for examining the global deformations of the cylinders) and failure analysis (for evaluating the damage resulting from external loadings). Therefore, the interaction between deformations and local damage could be evaluated simultaneously and the effect of such interaction on the stability and mechanical responses of the cylinders could be determined. The model was first applied to a long cylindrical tube subjected to transverse compressive loading between two rigid blocks. It showed excellent agreement with existing analytical predictions and very good agreement with experimental data up to the final stages where a deviation of less than 15% was found, which is an improvement on using models not considering the effects of damage. Christoforou et al (34), (73) looked at the lateral impact of composite cylinders. Their analysis was originally intended for single layer orthotropic shells but was modified by replacing the in-plane and bending stiffness terms with those calculated from laminated plate theory. It was based on the expansion of displacements, rotations and localised loadings in a double Fourier series, which satisfied the end boundary conditions of simple support. Initially, the predictions of stiffness were much lower than experiment, due to non-linear effects. However, once the non-linear effects of delamination crack propagation and crack initiation, among others, were introduced to the model, it was found to work well, giving good agreement with experiment.

Very little has been published on the use of commercially available finite element packages to model filament wound cylinders undergoing impact, although the problems with their use - especially the large number of elements required and the length of computer time (and associated high cost) have been documented (74). The main problem lies with the use in packages such as ANSYS, SAPIV and NASTRAN of orthotropic elements. The computer modelling in this project was carried out using a commercially available finite element package, NISA2 (75) (see chapter 7). This has several advantages over the above packages, especially its low price, availability on a wide variety of computers and its speed (76). NISA2 is particularly suitable for composite analysis, with features including no restriction on the lamination and the possibility of delamination, edge effects and interlaminar stress predictions (77). Although little has been published using NISA2 (78), a detailed evaluation of the program has been undertaken (79) and favourable comparisons with other packages (i.e. NASTRAN, ANSYS, MARC, PAFEC, ASAS, LUSAS, SUPERTAB, BERSAFE and ABAQUS) have been obtained by the National Agency for Finite

Element Methods and Standards (80).

2.3-2 Modelling the transient load/time behaviour.

Low velocity impacts have been shown to predominantly excite only the low frequency response of structures under test, meaning that the structural response of both the impactor and the structure being impacted may be modelled as a mass-spring system (33), (46). In its simplest state, this is a single degree of freedom model which considers the structure under impact as a massless linear spring being impacted by a mass i.e. the tup. This approach has been very widely and successfully used, for example by Sjöblom, Hartness and Cordell (10) on graphite/epoxy and graphite/thermoplastic plates and by Caprino, Crivelli Visconti and Di Ilio (64) on glass cloth/polyester panels. Christoforou, Swanson, Ventrello and Beckwith (33) refined the single degree of freedom model by inputing the non-linear (as opposed to linear) bending stiffness of the cylinders they tested obtained from experimental data. This gave very good agreement with experiment. Other groups of workers have further refined the mass-spring models to help analyse the higher modes of frequency. This they did by introducing a second degree of freedom i.e. the model now consisted of two masses and two springs. This introduced oscillations due to the inertial forces of the two masses. This approach was used by Shivakumar, Elber and Illg (81) on isotropic graphite/epoxy composite laminates, Elber (60) on graphite/epoxy plates and Suaris and Shah (82) on cementitious composites. The former two groups report good agreement with experiment, but Suaris and Shah do comment on the use of a linear stiffness (i.e. linear spring) resulting in the analytical model predictions being away from the experimental values. Perhaps the approach of Christoforou et al (33) could have improved their predictions.

2.4 Low velocity impact testing.

The following takes a more detailed look at the damage caused by low velocity impacts and the effects of this on the structural properties for both plate and cylindrical geometries. The degree of equivalence between static and dynamic testing is also examined.

2.4-1 On plates.

Several groups of workers have looked very closely at damage accumulation in composite plates undergoing low velocity impacts, with the favoured approach being to section through the damage area, polish the surface and then observe the microstructure. Boll, Bascom, Weidner and Murri (20) looked at low velocity impact damage on low fracture energy carbon/epoxy laminates of thickness 5mm. They found that crack initiation appeared to result from shear stresses developed during the early stages of impact. Then, a network formed by the growth of delaminations away from the impact centre. These are redirected into transverse cracks due to local conditions which cause transverse cracks to be energetically favoured. Interlaminar cracks were further favoured by the apparent low energy path along the fibre/resin interface. They also note that microsectioning confirmed that the damage through the laminate was not symetrically distributed. However, Cantwell and Morton (21) report that tensile stresses generated at the periphery of the area of contact in their 2mm thick carbon/epoxy laminates subjected to low velocity impact cause failure at the fibre/matrix interface at sufficient impact velocities. From these cracks, the damage progression is as described above by Boll, Bascom, Weidner and Murri, resulting in the shear cracks caused by the large shear stresses radiating outwards in a conical fashion from the periphery of contact, see fig. 2.1. As the impact area changes during the penetration process, the location of these large shear stresses changes, resulting in a myriad of shear cracks all extending approximately parallel to each other. This conical pattern has also been observed by Sjöblom, Hartness and Cordell (10) and by Verpoest, Marien, Devos and Wevers (25), but neither group comment on whether the damage was initiated by tensile or shear stresses.

On a more macroscopic level, Caprino (23) performed single bounce tests on carbon fibre laminates and identified that damage initiated at an energy of 0.8J. At this point, a first tensile failure occurred resulting in fibre splitting on the back face. [N.B. McQuillen, Gause and Llorens (83) also identify first failure as a tensile failure in the bottom surface when testing graphite/epoxy laminates at low velocities]. The front face of the laminate had a small indentation mark

Fig. 2.1 Schematic representation of damage progression due to contact stresses.

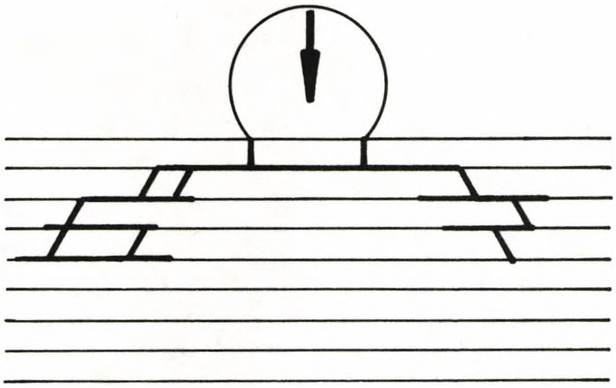

(from ref. 21)

on it. As the impact energy increased, an elliptical damage zone with major axis parallel to the 0° fibres was observed on the back face until an impact energy of 2.1J was found to result in complete penetration. Liu (84) performed subperforation (i.e. low velocity) impacts on glass/epoxy, Kevlar/epoxy and carbon/epoxy laminates, which he reports caused severe delamination in the internal interfaces but no serious surface damage. Damage observations resulted in the discovery of a peanut shaped delamination, which he refers to as a fundamental unit of delamination in all three investigated materials. The area of this shape depends on the impact energy and laminate layup, with the axis of every delamination coinciding with the fibre orientation of the lamina beneath the interface.

The effect on the structural material properties of low velocity impact has been assessed by several groups of workers, who mainly used the impact energy as opposed to the total delamination area, as the damage parameter. Caprino (23), Cantwell, Curtis and Morton (22) and Rotem (27) measured the strength after impact (i.e. residual strength) of carbon fibre laminates, with Rotem also studying glass/epoxy laminates. They all found that the residual strength did not fall significantly until well after visible damage was observed, with Cantwell, Curtis and Morton quoting an impact energy of 8J before the tensile strength fell. At this point, the strength fell to about 75% of its undamaged value, which they say is possibly due to the fracture of the load-bearing 0° fibres. All found after this initial drop, the curve decayed roughly exponentially until a constant value was approached. Rotem also looked at stiffness and modulus degradation as a result of impact. He found that the stiffness decreased with increasing impact energy even before visible damage was observed. As far as modulus degradation is concerned, he notes that for glass/epoxy laminates, there is no connection between this and the degradation in strength, unlike the ductile material case. Here, a degradation of, say, 10% in modulus means an equivalent degradation in strength. In the glass/epoxy case (which is a brittle material), a modulus degradation of greater than 10% does lead to a degradation in strength, but this is less than 10%.

Although the above all use residual properties as a function of impact energy to look at the effects of low velocity impact, this approach did not find universal approval. Sjöblom, Hartness and Cordell (10) comment on the total impact energy as not being a very good parameter, favouring energy loss during impact. They also object to the use of residual properties to assess the "impact threat", saying that there is no grounds to believe that residual properties are a linear function of the damage and that damage in their case was a far from linear function of impact energy. However, Liu (84) disagrees with the latter comment, finding that the total delamination area of the impacted plates of all three composite systems he tested was linearly proportional to the impacting energy. Sjöblom, Hartness and Cordell (10) favour using worst case reduction within a category of damage, saying it will give a better estimate of the performance of a structure after damage. The discrepances between their findings and those of Liu are perhaps explained by Verpoest, Marien, Devos and Wevers (25). They point out the problems of using total and absorbed energies as parameters, stating that these are not unique and depend heavily on specimen geometry and gripping conditions.

Many workers examined the degree of equivalence between static and dynamic testing to see if it is possible to perform simple static tests and use the results of these to predict dynamic behaviour. Caprino (23) and Elber (60) both state that their static and equivalent dynamic tests produced very similar force/displacement curves and Sjöblom, Hartness and Cordell (10) looked at micrographs of the damage and found no real difference between the static and dynamic case, all groups testing carbon fibre laminates. They all conclude that rate effects on the failure behaviour are minor and thus static tests can be used to model dynamic behaviour.

If repeated static and equivalent dynamic loadings were considered, however, it was found by Rotem (85) that repeated quasistatic loading did not degrade the strength whereas repeated impact did. He explains this by saying that the mechanism of damage in the two cases is different, with the subsurface impact damage resulting from the very high contact forces at the beginning of the impact. This leads to the destruction of the material under the surface, with repeated impact enlarging the damage.

2.4-2 On cylinders.

Considering firstly the damage process, Lloyd and Knight (32) evaluated the effects of low energy or low velocity impact events on high performance carbon fibre composites in small diameter pressure vessels. They found that an incipient damage point existed on their dynamic load/time curves (obtained by instrumenting the impact test), which they say is due to incipient damage where matrix cracking or delamination first occurred. They also comment on the importance of maintaining the cure conditions since they found that altering these resulted in 25% greater degradation in material properties. Christoforou, Swanson, Ventrello and Beckwith (33) also impacted carbon/epoxy cylinders, which were supported along their lengths in specially designed cradles. They note that on unloading, there was no permanent deformation in the cylinders.

Looking now at work done on filament wound glass/epoxy tubes, damage accumulation studies were carried out by Harrison and Bader (43) using their slow indentation technique (described previously). They found that tube failure was preceded by a fold in the surface which moved around the circumference as the indentation deflections increased. This fold eventually formed a crease whereby the fibres were broken in bending. The membrane and in-plane shear stresses then acted to extend the cracks and to form delamination zones around the failure region. They also found that the strains in the four quadrants of the tube surfaces (as measured by electrical resistance strain gauges) were assymetric, which they say is due to the relative distribution of the fibres near each surface.

Christoforou, Swanson, Ventrello and Beckwith (33) carried out residual property testing of cylinders by performing burst tests. They also found that the cylinder hoop stress decreased as the impact energy increased and that linear relationships existed between the hoop and axial delamination lengths (measured using ultrasonic C-scans) and impact energy.

In a later piece of work, Christoforou and Swanson (34) compared static and dynamic force/displacement curves and found that they were pretty much the same, suggesting a degree of equivalence between static and impact testing for this geometry.

This part of the literature review underlines earlier comments on the lack of previous impact testing carried out on cylinders, let alone impact testing at low velocities. Clearly, more work is needed in this area.

3. EXPERIMENTAL METHODS.

This chapter deals with experimental methods which are common to several or all of the test geometries considered. The methods are arranged in order of testing i.e. static tests, followed by equivalent impact tests. The damage caused was then analysed by both destructive and non-destructive techniques including specimens being retested to failure to obtain their residual properties. This procedure is the basis for the majority of the work performed. The individual experimental methods are considered in detail below.

3.1 Static Tests.

All static tests were performed on an Instron 1185 tensile testing machine (for the sections and small diameter pipe tests) or an Instron 1195 tensile testing machine (for the large diameter pipes) set up in compression mode using a three point bend geometry (see Figure 3.1). The load was applied at the midpoint of the top surface transverse to the pipe axis by a solid steel cylinder of length 150mm and diameter 25mm for the small pipe tests and of length 800mm and diameter 40mm for the large pipe tests. A variety of support conditions were used i.e. floor supported along the pipe length [see Figure 3.1(a)], supported in 81mm radius semicircular cradles of width 50mm [see Figure 3.1(b)] and supported in three point bend configuration [see Figure 3.1(c). The majority of tests (i.e all the full and half pipe tests in both diameters {with one exception - see below}) were

Fig. 3.1 Support conditions used in the tests:

a) floor-supported.

b) cradled.

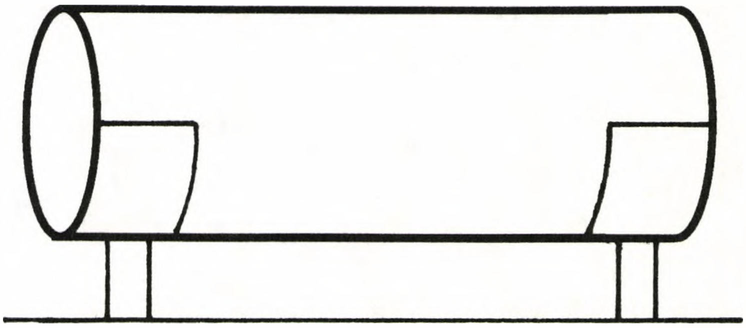

c) three point bend configuration.

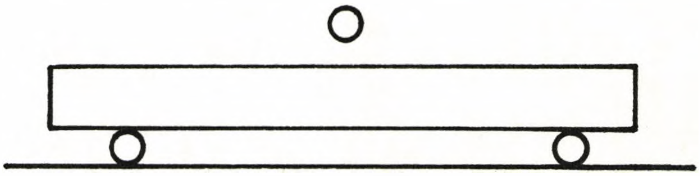

performed at a strain rate of 5mm/min. However, to satisfy the individual test requirements, a variety of strain rates were used from very low strain rates of 0.5 to 1mm/min for all the floor supported sections and the 70mm three point bend supported pipe sections (see sections 4.1 and 4.3-3), through a strain rate of 10mm/min for the remaining three point bend tests, including the standard tests performed (see sections 4.3 and 3.4-2) to very high strain rates of 50mm/min for the large diameter videoed pipe tests (see section 5.1-3a). The reason for the choice of strain rate in each case is discussed in the individual test details.

Tests were initially carried out until the pipe was about to collapse (which will be referred to as full specimen damage) to establish the damage process and the major features of the load/displacement curve. Once this had been achieved, a series of partial damage tests to selected points on the load/displacement curve determined from the full curve were carried out. These were performed to observe the delamination patterns obtained at various stages on the load/displacement curve (and thus at various stages in the damage process). The effects of varying the initial damage on the mechanical properties were also examined. The mechanical properties considered were those easily obtained from the load/displacement curve i.e. peak load, deflection to peak load, initial gradient and energy to peak load. [N.B. It is worth while at this point defining peak load for all future tests. Peak load is always the maximum load sustained by the particular specimen in its particular test - for example, it is the load at first failure when the test is stopped at first failure, the load selected as an end point of the test in the partial damage tests and the maximum load attained in the full specimen damage tests.] Energy to test end was also obtained and was used as a basis for performing equivalent impact tests, which are discussed below.

3.2 Impact Tests.

Two types of transverse impact tests were performed on the specimens. The majority were falling weight tests and were performed on the small pipes and pipe sections. For these, a large drop hammer rig was used with a maximum possible drop height of 8m. Both full and partial damage tests were carried out, the required drop height being calculated for each specimen from its equivalent static test using

$$E = mgh \tag{3.1}$$

where E is the static energy (i.e. the area under the static force/displacement curve), m the tup mass, h the drop height and g the acceleration due to gravity (taken as $9.81 m/s^2$) and the impact velocity, v, was calculated using

$$v = (2gh)^{\frac{1}{2}}. \tag{3.2}$$

Two tups were used in this work. The first was primarily used for very low energy requirements and had a mass of 3.4kg while the second, more widely used, had a mass of 36kg. Both tups had the same impactor nose attached, which was made to the same dimensions as in the static tests and equivalent support conditions to the static tests were also used.

Initially, multiple bounce tests were carried out i.e. the tup was allowed to impact the specimen until it came to rest. In order to obtain impact data which could be comparable with static data (e.g. peak load, initial gradient etc.), the first bounce of the multiple bounce impacts was instrumented using the technique of laser-doppler velocimetry (the background to which is described in Chapter 2). This provides a direct method of measuring velocity as a function of time. A Dantech laser-doppler velocimeter was used working in dual beam backscatter mode and information was displayed on a 20MHz oscilloscope and stored on a 20MHz Datalab transient recorder. The signal was filtered with a cutoff frequency of 800Hz. This value was predetermined experimentally as the optimum frequency for reducing the signal noise whilst retaining oscillations required for analysis. The signal was then processed to derive energy/displacement, force/displacement and force/time curves.

However, although multiple bounce impacts are realistic and easy to perform, they are not truly equivalent to the static tests since they have the effect of loading, then unloading a little, then loading again until the tup comes to rest. As one of the aims of this work was to compare static and impact tests of equivalent energies, the case for using single bounce impacts is apparent, though the following problems should be noted.

Firstly, single bounce impact tests are less likely to be realistic (although they can occur in practise) and secondly, they can be difficult to achieve. After several attempts, a mechanism consisting of a release trigger and stop, a spring loaded bolt and an adjustable frame was used (see fig. 3.2). This mechanism achieved single bounce impacts as follows. As the tup fell initially (a), the trigger movement allowed the bolt to release (b). Then, as the tup rebounded, the bolt sprang into position and caught the tup at the stop (c). The mechanism was bolted onto the adjustable support frame, (see fig. 3.2b), which allowed both the cradled and floor-supported conditions to be tested. The system worked very well for all cases except when a very low drop height was required. In these cases, the tup rebound was not high enough to be caught by the mechanism. Laser-doppler velocimetry was again used to record the velocity/time history of the impact and from this, again using specially written software, energy/displacement, force/displacement and force/time traces were obtained.

The second type of impact tests carried out were multiple bounce pipe drop tests performed on the large pipes only. In these, 5m pipe lengths were winched up using a crane and dropped onto an instrumented anvil from predetermined drop heights. The anvil had a nose made to the same dimensions as the large static nose bolted to it for equivalence purposes. Further experimental details for this test type are contained in Chapter 5.

Fig. 3.2a) Single bounce mechanism for use in impact tests.

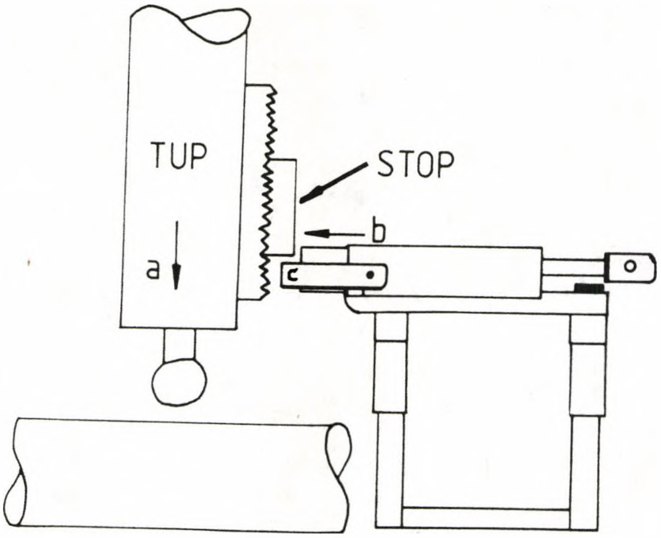

Fig. 3.2b) Details of the adjustable frame.

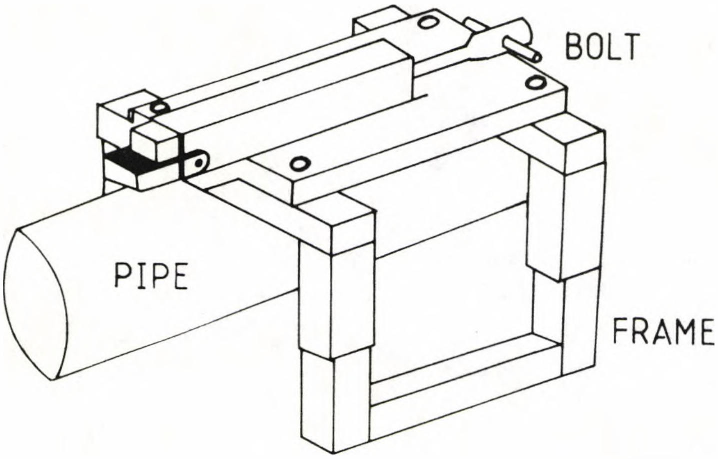

3.3 Damage Analysis Techniques.

Several methods were used to examine the effects of the damage caused by static and impact tests. The methods are divided into non-destructive and destructive techniques, and are considered below.

3.3-1 Non- destructive testing techniques.

There were two non-destructive techniques, both of which were used to observe and measure the extent of damage caused by testing.

3.3-1a) Penetrant-enhanced X-ray radiography.

This technique and the reason for using zinc iodide as the penetrant have already been discussed in the literature review section. It should be noted here that the zinc iodide penetrant used was that developed by Rummel, Tedrow and Brinkerhoff (57) with a slight alteration. The amount of photoflo (which is the wetting agent) was increased from 1ml to 10ml to enhance surface tension reduction, and thus make it easier for the penetrant to penetrate (86).

The damaged specimens were impregnated as follows. Firstly, surface contamination was removed using a hair drier. [If this is not done, the resultant radiograph will be blurred]. The zinc iodide solution was then dripped onto the specimen from a burette until it had penetrated all cracks and pores. A burette was used because it can easily both control the rate of the penetrant flow and direct it into the cracks and pores as required. Previous experiments had determined that introducing 20ml of the zinc iodide solution over a period of five minutes allowed the cracks and pores to be sufficiently penetrated to reveal the extent of the damage. Any excess fluid was removed from the specimen surface with tissues and the specimen was left to dry for more than 12 hours.

The specimens were then X-rayed using a Watson MX4 medical X-ray unit with the following settings:

Tube voltage = 60kV
Exposure = 20mAs
Tube current = 50mA

The experimental setup is shown in fig 3.3. After X-raying, the film was developed and printed and from the resulting radiographs, the area of damage was measured.

This technique is very good for specimens where it is easy for the penetrant to be introduced, especially in the pipe section tests. However, for the full pipe specimens and for any tests where very little damage has been done i.e not enough to allow penetration of the zinc iodide penetrant, another technique is required. This is described below.

3.3-1b) Backlighting technique.

This is a very simple technique which consisted of inserting a strong light source behind the damaged surface or, in the case of the full pipe sections, inside the pipe. This caused the delamination patterns formed to be very clearly illuminated and illustrated, by revealing overlapping ellipses, that delamination was not simply found between two layers but

Fig. 3.3 Experimental setup of the X-ray machine.

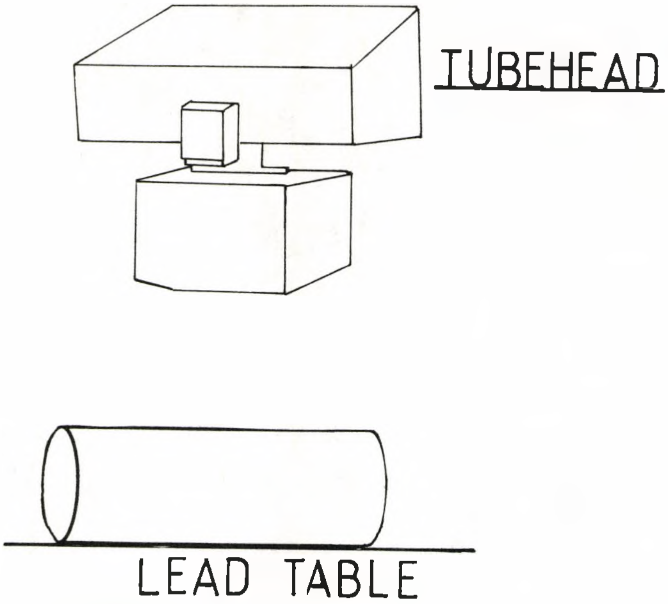

Fig. 3.4 How the area of damage was calculated.

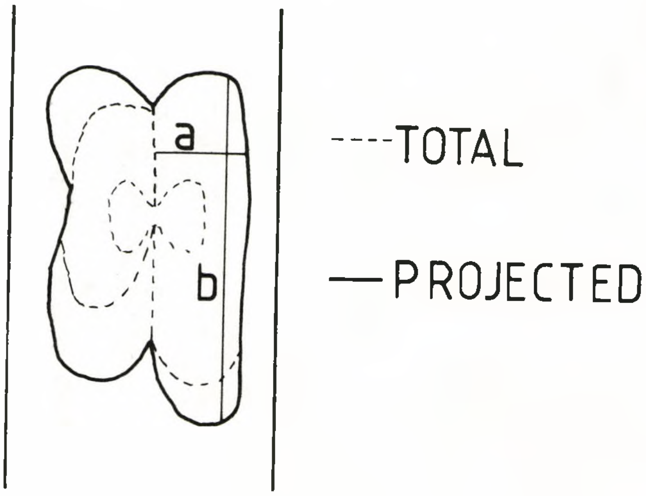

was occurring throughout the pipe thickness. The delamination patterns were then photographically recorded, allowing quantitative measurements of the extent of the damage to be made, a very good first approximation being to estimate the area of damage as follows. Firstly, the area was divided into ellipses, see figure 3.4, the area of each ellipse being calculated from

$$A = \pi ab \qquad (3.3)$$

Then, summing the areas of all the ellipses allowed an estimated total area of damage to be found which took into account delamination occuring throughout the pipe thickness. For comparison, the projected damage area was also measured in each case, this being the area without considering delaminations in the various layers (see fig. 3.4)

3.3-2 Destructive testing techniques.

There are two destructive techniques, the first used to provide extra information to that gained using the non-destructive techniques and the second to quantify the effects of damage on pipe performance.

3.3-2a) Examination of the damage using microscopy

In order to gain as much insight as is possible into the damage process, a selection of impacted and statically tested pipes were sectioned over the full damage spectrum from first failure to full damage for both floor and cradled support conditions. Once the required amount of damage had been introduced, the area it produced was sectioned from the pipe. The rough saw cuts caused by doing this were removed firstly using a linisher and then using 180 grade grit grinding paper. Further polishing proved unnecessary. The sections were then observed and photographed at low magnification (x9) using a Wild M8 Stereo Zoom microscope and the type of damage recorded along with the layer numbers between which delamination occurred. It should be noted that an undamaged pipe was also sectioned to ensure that the damage observed was that introduced by the actual tests and not by the sectioning and polishing processes.

3.3-2b) Residual property tests.

After the amount of damage in each specimen had been recorded, all specimens, whether initially statically tested or impacted, were retested to failure on the Instron, using the same geometries as in the original test, to measure their residual properties. Finally the specimens were re-examined using the optical technique to see what effects the retests had on delamination growth.

3.4 Quality assessment.

This series of tests proved necessary because of the variations observed in what were nominally identical pipe specimens. Variations in wall thickness were observed in both the large pipes (from 9/10mm to 12/13mm) and the small pipes (from 5mm to 6mm) but the most worrying variation was that indicated by changes in resin colour as this could mean changes in the cure conditions of the pipe or in the resin composition itself which were likely to have a noticable effect on pipe properties (32). This was only a problem in the case of the 150mm inside diameter pipes since the large pipes tested were all made in one batch. However, the small pipes were ordered throughout the duration of the project and although each batch had the same resin colour, this was observed to vary from one batch to the next. There were three identifiable resin colours, which for ease will be referred to as dark, medium and light. In addition to the differences in resin colour, it should be noted that the dark resin pipes are less well constructed than the other types. This is instantly apparent from the outer suface finish which is very rough compared to that of the medium and light resin pipes.

During scheduled testing, it was observed that the dark resin pipes were far weaker than the other two pipe batches, and that the light resin pipes were the strongest. Thus, it was decided to carry out the following series of tests to aid in assessing the effects of the variations in wall thickness, resin colour and quality of manufacture.

3.4-1 Ash tests.

These were conducted to determine the glass content of the different pipes and were performed to ascertain if the differences in mechanical properties were due to the variations in glass content as opposed to variations in resin type or cure condition. These tests were conducted on both large and small pipes of differing wall thicknesses and resin colour. It should be noted that the nominal weight percentage for all these pipes is 70% glass fibres.

Ash tests are very simple to carry out. The first stage was to "clean" the crucibles used and this was done by placing them in a furnace for more than two hours at 500°C. The crucibles were then allowed to cool for 20 minutes before they were weighed. Specimens from each pipe under consideration were cut (further details of specimen numbers involved are contained in the sections concerned with the individual pipe sizes and geometries) and placed in the crucibles. The weight of the crucible plus piece of composite was recorded and therefore, by subtraction, the weight of the composite was known. The crucibles plus pieces of composite were then placed in the furnace at 500°C overnight to burn off the resin. After cooling, the weight of the fibres plus crucible was recorded and, from this, the glass fibre volume fraction determined using :

$$V_f = \frac{W_f/p_f}{W_f/p_f + W_m/p_m} \qquad (3.4)$$

where V_f is the fibre volume fraction, W_f is the weight % fibres, W_m is the weight % matrix, p_f is the density of the fibres (= 2.56×10^3 kg/m^3) and p_m is the density of the matrix (= 1.25×10^3 kg/m^3).

3.4-2 Determination of the differences between the three resin types by standard three point bend testing.

These tests were performed to assess the differences in mechanical properties between the dark, medium and light coloured resins and so were only performed for the small pipes. It was decided that, to make a fair comparison, the best method would be to perform standard tests and those selected were three point bend tests, conducted according to the British standard method (87).

The specimens were cut in accordance with the standard and measurements of specimen thickness and width were made using vernier callipers. The required relationship was found to be satisfied (i.e. since thickness, h, lay between 1 and 10mm, width was required to be 15±0.5mm.) Also, the correct span value was calculated for each specimen, this being 16h.

Tests were conducted on the Instron 1185 using the standard three point bend rig. In accordance with the standard method, the crosshead speed used was 10mm/min. Thirteen specimens from the dark and medium pipes were tested and twelve from the light pipes to obtain good average values of the mechanical properties under consideration i.e modulus of flexure, flexure stress, flexure strain and energy values.

3.4-3 Determination of the differences between the three pipe types by microscopy.

Microscopic examination was carried out in order to investigate if there were any other physical differences between the three pipe types besides the obvious one of resin colour. Under investigation were the number and thickness of the layers of each pipe type (to ascertain if the differences in pipe thickness and mechanical properties were simply due to either extra composite layers or thicker composite or resin layers). The void content and interlaminar bonding were also examined. To this ends, samples were taken from the three pipe types and were mounted in Scandiplast resin, each pipe type being mounted in two orientations. These were upper resin surface downwards, and sideways (i.e. so that the number of layers could be counted). The samples were then ground using three successively finer silicon carbide papers and polished using a Struers DP-U2 automatic polisher.

The number of layers in the samples was counted at low magnification (x6) using a Wild M8 Zoom Stereo microscope. However, the remaining examinations required higher magnification (x100) so for these a Nikon Epiphot microscope was used and the regions of interest were photographed for reference and ease of comparison.

4. TESTING OF PIPE SECTIONS.

The tests performed in this chapter deal with experiments carried out on sections cut from both the large (400mm inner diameter) pipes and the small (150mm inner diameter) pipes constructed from E-glass and epoxy resin with a winding angle of ±55°. The tests can be divided into three groups, each of which is considered separately below along with the reasons for performing them and the results they yielded.

4.1 Crush tests.

Flat specimens were used in these tests as an attempt to discern those characteristics of failure in the load/displacement curve and also the damage features that are solely due to crush i.e. are not caused by delamination. Initially, the nearest approximations to flat beams (i.e. 1/16th large diameter pipes) were used. Both static and impact tests were conducted on these floor-supported specimens (see fig. 4.2a) of length 500mm. The static tests had to be stopped when the peak load reached 95kN i.e. just before the limits of the 100kN load cell had been exceeded. Impact tests were then performed to equivalent energies and the damage obtained in the two cases was compared.

Both static and equivalent energy impact crush tests were also performed on 1/8th small diameter pipes of length 500mm and 150mm. Once again, the static tests had to be stopped at 95kN to protect the load cell.

Damage for the above tests was observed by both penetrant enhanced X-ray radiography and by the backlighting technique. Both methods revealed the damage but the former proved the more useful for examining this particular geometry.

4.2 Tests conducted on half pipes.

These tests were performed as an intermediate stage between the crush tests described above and the full pipe tests (see chapter 6). All tests were performed on medium resin small diameter pipes of length 500mm, had a floor-supported geometry (see fig. 4.4) and were conducted statically. Initially, tests were carried out to full specimen damage. Damage accumulation was then studied by performing partial loading tests to points selected from the "full damage" load/displacement curve. The damage was assessed by penetrant enhanced X-ray radiography and the backlighting technique.

Equivalent static tests to full damage were also conducted on dark resin pipe specimens to investigate the effect of the "different" resin. [N.B. It was actually the results of these tests which were to prompt the quality assessments detailed in section 3.4 to be conducted.]

4.3 Correlations of residual properties to initially applied (incident) energy and damage area.

Partial and full damage static tests were conducted initially to introduce varying amounts of damage after which the specimens were tested to failure.

The idea then was to relate the damage area and the energy causing it to the residual properties (i.e. peak load, initial gradient and deflection to peak load) measured upon retest and to examine the results for any correlations. The specimens used for this work were 1/8th sections 150mm inner diameter pipes and tests were conducted in three point bend configuration (see fig. 3.1c), with the only variables being the strain rate, specimen length and test span. The three test spans considered are discussed below.

4.3-1 Sections with a test span of 500mm.

This specimen test span was chosen originally because it was the same as in the crush tests in section 4.1. The reason for this was so that even if damage area measurement proved unsuccessful, these tests would be useful as a means of comparing flexural and crush damage. Both static and equivalent energy impact tests were performed (the energy used being 23.9J) and, for consistency, the same three point bend rig was used in both cases, having a roller and nose diameter of 25mm and length of 150mm. Static tests were performed on the Instron 1185. The 100kN load cell was used with the x10 converter on and the crosshead speed (strain rate) was 10mm/min, with the chartspeed being 20mm/min. Impact tests were performed on the large drop weight rig. Damage measurements were made using X-ray radiography. To illustrate the benefits of introducing the zinc iodide penetrant, X-ray radiographs were initially taken without penetrant addition and then compared with penetrated sections.

4.3-2 Sections with test span 120mm.

This specimen length was chosen to give an aspect ratio of 20:1. Only static tests were performed on the Instron 1185 using the same rig as in 4.3-1. The 100kN load cell was used with the x10 convertor on and the chartspeed and crosshead speed (strain rate) were 20mm/min and 10mm/min respectively. Tests were conducted over the energy range 8.5J to 76J and the damage sustained was observed using penetrant enhanced X-ray radiography.

4.3-3 Sections with test span 65mm.

The sections now had the following dimensions: 70mm length, 60mm width and 6mm thickness. They were tested on the Instron 1185 using the same three point bend rig as above with a span width of 65mm. The 100kN load cell was used with the x10 convertor on and the crosshead speed (strain rate) and chartspeed were held at 1mm/min and 20mm/min respectively. Initially, pilot tests to full specimen damage were performed to examine the viability of using sections of this size and to establish the shape of the load/deflection curve and the damage process. Once this had been achieved, partial damage tests were conducted to selected points on the load/displacement curve as illustrated in fig. 4.1. The usual properties were extracted from the curves and then damage was measured by both X-ray radiography and the backlighting technique.

After damage observation, the specimens were taken

Fig. 4.1 Load/deflection plot for 1/8th small diameter pipes, test span 65mm and in three point bend configuration.

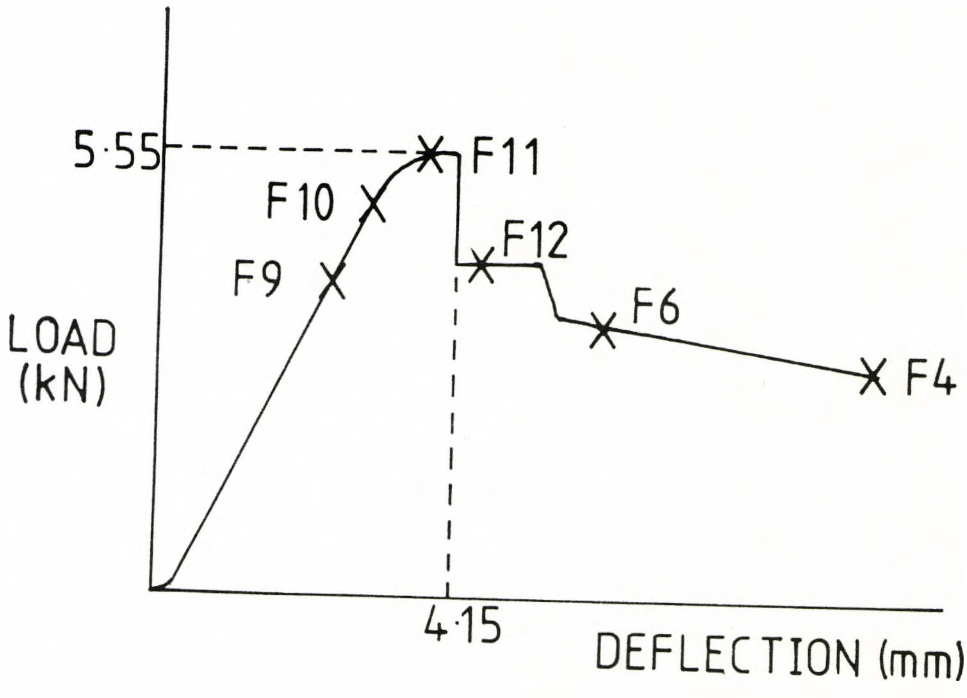

back to the Instron and their residual properties (peak load, initial gradient and deflection to failure) were measured by testing to failure. This criterion was achieved for all the specimens.

4.3-4 Microscopic examination of the damage.

A further series of tests were performed to aid the damage analysis. Specimens were tested with each of the above spans and examined non-destructively as above. Then, instead of being retested to failure to measure residual properties, the specimens were sectioned and examined in a Metalloplan light microscope following the procedure outlined in 3.4-3. The only difference was that examination and photography took place at higher magnification, ranging from x62.5 to x2300.

4.4 Results.

4.4-1 Crush tests.

The large and small diameter pipe sections tested yielded slightly different load/deflection plots. Fig. 4.2a shows an example of the plot for a 1/16th large diameter pipe. The "kink" (marked I in the curve) occurred at the point in the damage process when the upper surface crush crater was formed, the lower resin surface cracked and delamination was initiated. This was very localised, as can be seen in fig. 4.3, which is a penetrant enhanced X-ray radiograph of T1, a large diameter 1/16th specimen tested to 95kN. Very little damage occurred after point 1 and virtually all the deflection was recoverable. Impact damage was identical to static damage.

Fig. 4.2a Load/displacement plot for the 1/16th large diameter pipe crush tests.

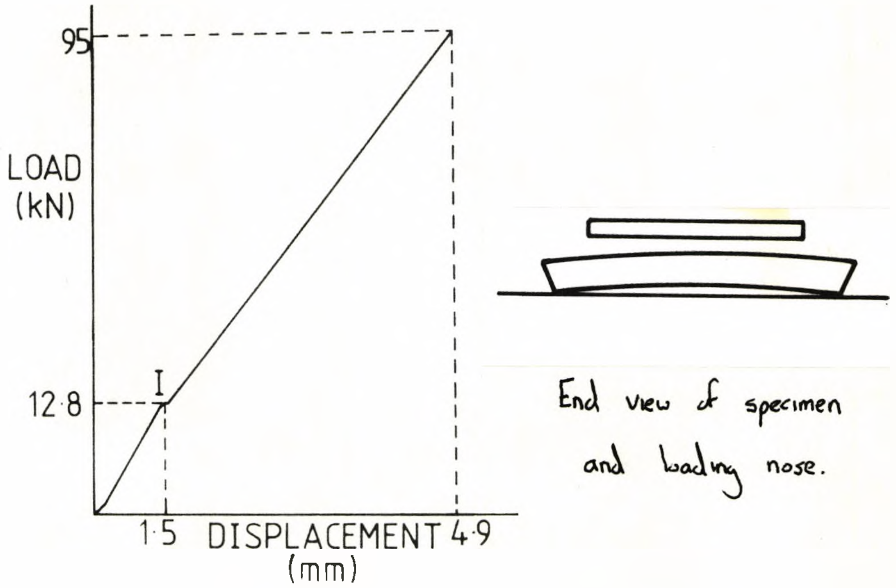

Fig. 4.2b Load/displacement plot for the 1/8th small diameter pipe crush tests.

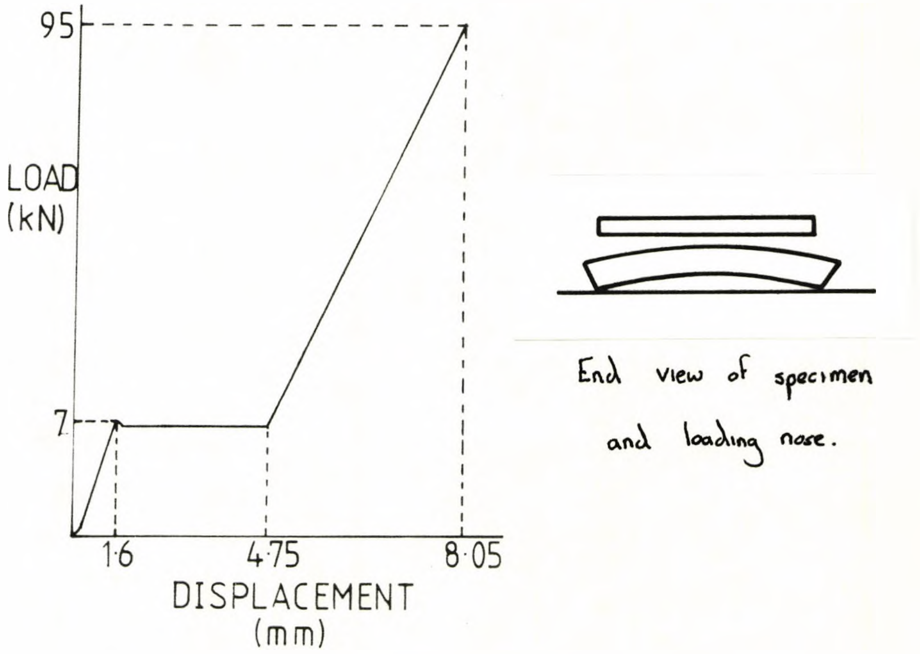

Fig. 4.3 Penetrant enhanced X-ray radiograph of T1.

Regarding now the 1/8th small diameter pipe sections of both lengths, they yielded load/displacement plots such as fig. 4.2b, which reveals a distinct plateau region after the "kink" in the curve. This could be because the 1/16th's are flatter than the 1/8th's i.e. the plateau is due to flattening of specimen curvature.

It should be noted that, despite the difference in the load/displacement plots, identical damage is found in these static (and impact) tests as in the 1/16th large diameter pipes considered above.

The data extracted from the load/displacement plots is presented in tables 4.1 and 4.2a and b, indicating how little deflection and energy is required for the specimens to reach the limits of the Instron load cell. Table 4.2a, concentrating on the 1/8th small diameter specimens tested to first failure, also reveals that the actual crush damage occurs at very low loads (5.8 - 7.8kN compared with the 95kN end of test value), and thus low energies and displacements. It proved interesting to observe if crush damage in other geometries tested throughout this work also occurred so early in the test.

4.4-2 Tests conducted on half pipes.

An example of the load/displacement curve to full specimen damage for this test geometry is shown in fig. 4.4 and reveals two distinct failure points. The damage sustained was analysed by both non-destructive techniques. The backlighting technique revealed the size

Table 4.1 Static data for the 1/16th large diameter pipe crush tests.

Specimen No.	Peak load (kN)	Gradient (N/mm)	Deflection (mm)	Energy to test end (J)
T1	95.00	9.39×10^3	4.9	180.4
T2	95.00	1.95×10^4	4.4	155.5

Table 4.2a Static data to first (crush) failure for the 1/8th small diameter pipe crush tests.

Specimen No.	Peak load (kN)	Gradient (N/mm)	Deflection (mm)	Energy to test end (J)
T7	6.9	5.19×10^3	1.6	4.75
T8	7.2	4.98×10^3	1.7	5.12
T9	5.8	3.53×10^3	2.1	5.25

Table 4.2b Static data to test end for the 1/8th small diameter pipe crush tests.

Specimen No.	Peak load (kN)	Gradient (N/mm)	Deflection (mm)	Energy to test end (J)
T7	95.0	4.27×10^4	8.1	146.09
T8	95.0	5.00×10^4	8.1	130.36
T9	92.8	4.10×10^4	9.1	217.93

Fig. 4.4 Load/displacement plot for the half pipe tests.

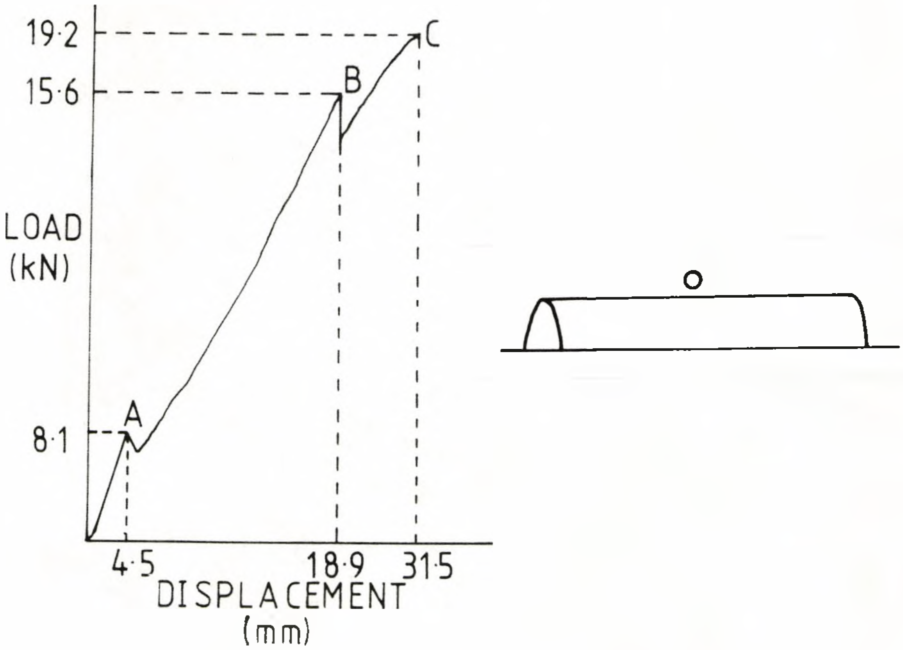

Fig. 4.5 Damage accumulation for the half pipes.

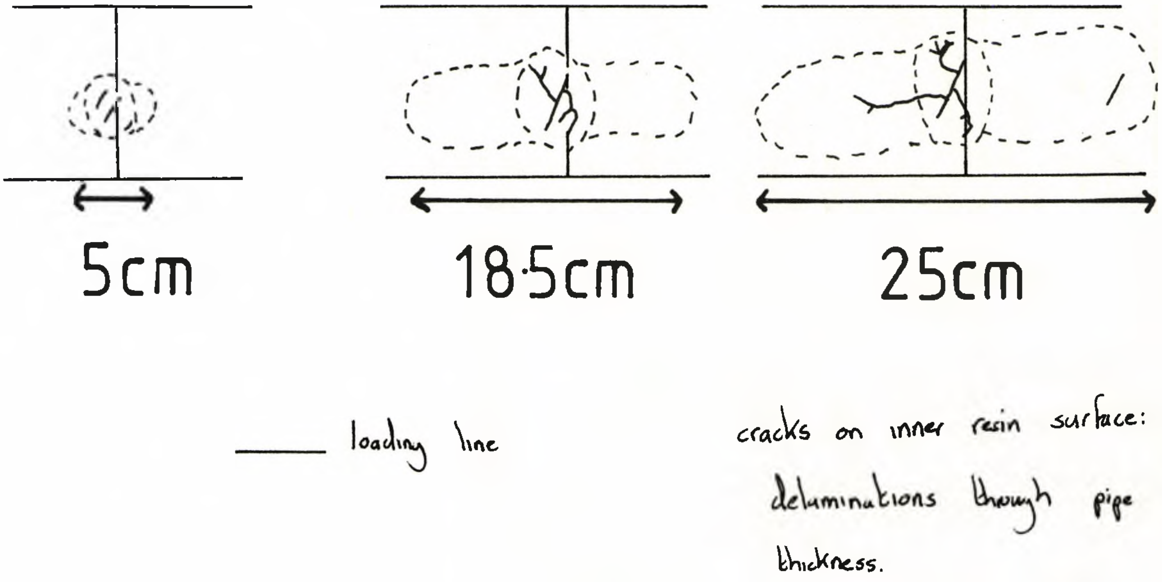

a). After first failure

b). After second failure

c) At test end

of the delamination pattern but gave little detail of the central crush damage: the X-ray radiography technique revealed the finer details of the crush damage but gave no indication of the extent of the delaminations. Therefore, a combination of both techniques was used in the following analysis.

At the first failure point (marked A in fig. 4.4), the cratering effect surrounded by resin cracks was observed in the upper surface. This was accompanied by slight undersurface cracking in the fibre direction and resulted in a delamination of length 5cm (see fig. 4.5a). This point is believed to be purely crush damage and therefore equivalent to that sustained in the beam specimens above.

At the second, and more catastrophic, failure (marked B), the upper surface damage was much more extensive (see fig. 4.5b). The delamination length was now 18.5cm and tears were found not just in the fibre direction. Flexure of the pipe ends had not yet started to occur.

For tests continued beyond second failure, the pipe began to flex and specimen damage was more extensive, with the delamination length now being 25cm (see fig. 4.5c).

The test figures extracted from the force/displacement plots are presented in tables 4.3a and b. Table 4.3a presents the data up to first failure and table 4.3b to second failure. Included in these tables are the data from the dark resin pipes for comparison.

Table 4.3a Static data for the half pipes up to first failure.

Specimen No.	Resin Colour	Peak load (kN)	Deflection (mm)	Gradient (N/mm)	Energy (J)
W1	Dark	5.68	4.50	1.33×10^3	8.82
W2	Dark	7.50	3.25	3.05×10^3	9.80
W3	Dark	7.68	4.00	2.27×10^3	13.18
T3	Medium	6.75	4.40	1.92×10^3	13.54
T4	Medium	8.10	4.50	1.80×10^3	18.22
T5	Medium	8.40	4.13	2.24×10^3	17.33
T6	Medium	7.70	4.25	1.80×10^3	16.36

Table 4.3b Static data for the half pipes up to test end.

Specimen No.	Resin Colour	Peak load (kN)	Deflection (mm)	Gradient (N/mm)	Energy (J)
W1	Dark	11.30	13.50	0.98×10^3	82.51
W2	Dark	13.00	12.00	0.82×10^3	97.57
W2	Dark	13.90	14.00	1.90×10^3	106.60
T3	Medium	17.95	24.53	1.04×10^3	262.18
T4	Medium	15.60	18.88	0.71×10^3	182.65
T5	Medium	16.50	20.75	0.76×10^3	208.73

These undergo a similar damage process producing a similar load/displacement curve to their medium resin counterparts and up to first failure point have similar properties. However, beyond this point the dark resin pipes reveal themselves to be much weaker, failing at loads of between 11.3kN and 13.9kN as opposed to between 15.6kN and 17.95kN for the medium resin half pipes. Further analysis of the different coloured resin is presented in section 6. [N.B. It should be noted that the gradient quoted in table 4.3b is the gradient between first and second failure and NOT the initial gradient value taken from the beginning of the tests. This will apply throughout this work].

4.4-3 Correlations of residual properties to initially applied (incident) energy and damage area.

4.4-3a) Sections with a test span of 500mm.

The first thing to note is that these tests did not fulfill the criterion for which they were established. Observing an example of the X-ray radiographs taken of the specimens after testing (see fig. 4.6a) reveals why. In these tests, no actual area of damage was produced, simply lower surface resin cracking was observed. There was a huge amount of deformation (78.5 - 82mm!), almost all of which was recoverable. Damage was similar under both static and impact conditions.

Despite this test span not yielding the required information, these tests were not wasted for two reasons. Firstly, they were used to demonstrate the

Fig. 4.6a X-ray radiograph of a 500mm test span specimen (with zinc iodide X-ray opaque fluid added).

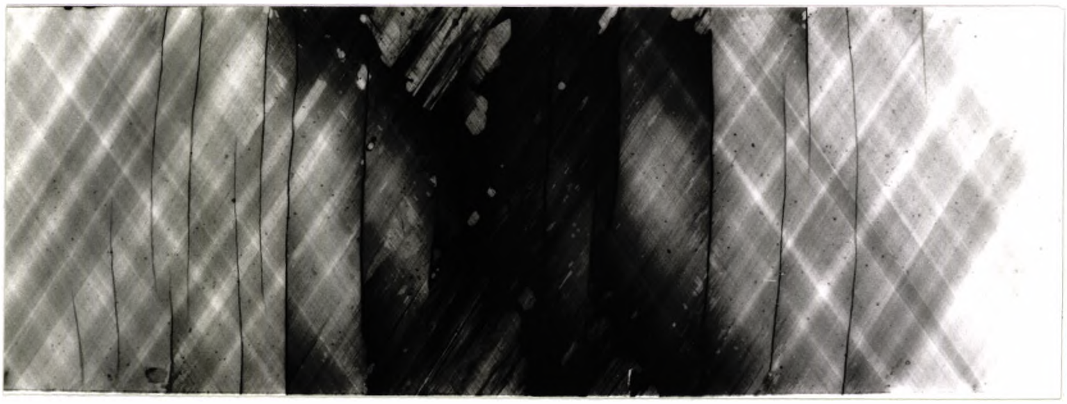

Fig. 4.6b X-ray radiograph of a 500mm test span specimen (without zinc iodide X-ray opaque fluid).

benefits of adding the zinc iodide X-ray opaque fluid. Fig. 4.6b is an X-ray radiograph of the same specimen as in fig 4.6a without the addition of the penetrant and it can be seen that the damage is very difficult to discern. Secondly, these tests proved useful means of comparing crush and flexural damage (see figs. 4.3 and 4.6a). Crush damage consists of a gel coat crater, resin cracking on both surfaces and delamination initiation. It is very localised. Flexural damage consists of lower resin cracks only and extends over a much larger area.

4.4-3b) Sections with a test span of 120mm.

The thing to note here is that as above these tests did not fulfill the criterion for which they were established. Observing an example of the X-ray radiographs taken of the specimens after testing (see fig. 4.7) again reveals why. In this case, failure did occur, unlike the 500mm test span specimens which produced lower surface gel coat cracks only. The area of damage produced by this process was "egg-timer" shaped, which was probably due to tensile failure at the specimen edges i.e. it was a geometrical effect. This shape did not lend itself to easy measurement and therefore, it was decided to abandon these tests and to use the 65mm span as a basis for the residual property against damage parameter (i.e. incident energy and area of damage) correlations. This series of tests did, however, emphasise both the advantages and disadvantages of using the X-ray technique. On the positive side, the gel cracks and delaminations are very well revealed. However, the

Fig. 4.7 X-ray radiograph of a 120mm test span specimen.

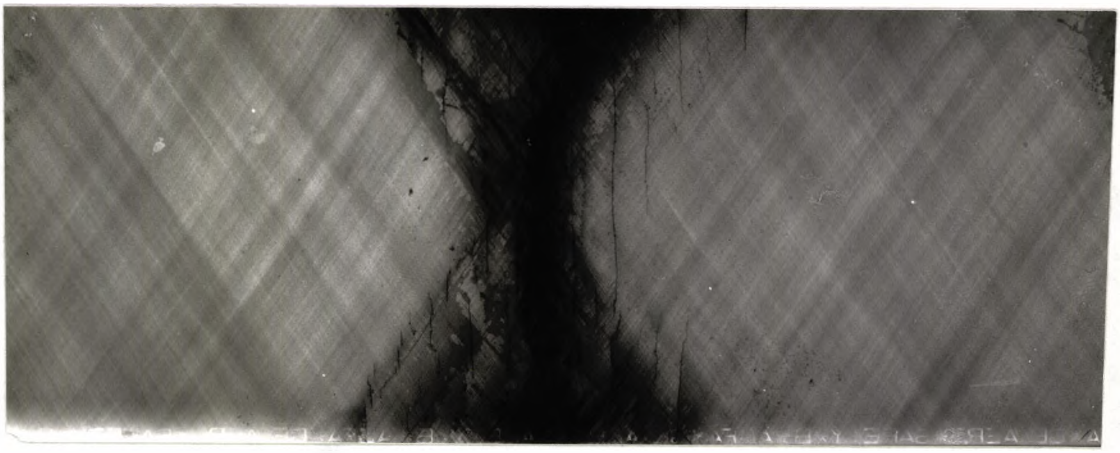

Fig. 4.8 X-ray radiograph of a 65mm test span specimen.

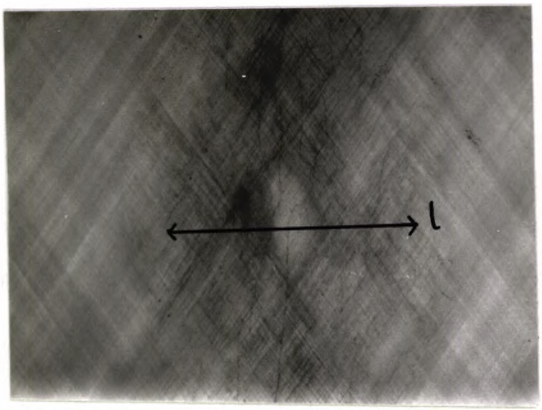

l = damage length

damage all appears to be in one plane, which is not the case and can thus be misleading.

4.4-3c) Sections with test span 65mm.

Unlike the above two test spans, these tests produced sections with very measurable damage areas, as can be seen in fig. 4.8. It was also apparent that the damage on both upper and lower surfaces resembled closely the crush damage seen previously. Since a span length had now been established so that damage measurement was possible, the programme of tests illustrated in fig. 4.1 was justified.

The pilot tests performed revealed the following damage process. Initial damage consisted simply of resin cracking. The first failure was caused by the top surface deforming (again as previously described). Finally, the layers began to delaminate from the inner resin surface upwards.

Regarding now the partial damage tests, the level of damage at each point is given below for additional information:

i) F9 - loaded up to 3kN. At this stage, there was no visible damage.

ii) F10 - loaded up to 4.85kN. This marked the onset of damage i.e. both resin cracks and the crush crater had begun to form.

iii) F11 - loaded up to 5.2kN. This was intended simply as a point after F10 and before first failure occurred.

iv) F12 - stopped after first failure.

In addition to these tests, F4 and F6 were conducted, both to well beyond failure. In the case of F5, a problem arose because the section failed at the edges, and not in the central portion, first. This only occurred with this one specimen and could be due to several reasons, including non-uniformity of the pipe sections and weakening at the edges due to the cutting process. The former is the more likely explanation.

Damage was then measured by the two usual techniques, with a combination of the two being the most useful way of extracting the necessary information. The backlighting technique was better used when damage was light i.e. when the penetrant couldn't enter the specimen. When the damage was extensive enough to allow penetration of the X-ray opaque fluid, the X-ray method was a better technique. In this case, the parameter actually used was damage length, as indicated in fig. 4.8. This was because the major delamination occurred in one layer only, and so a total area calculation was unnecessary. The specimens were then tested to failure to obtain their residual properties.

The numerical information extracted from both the initial and residual tests is presented in tables 4.4a and b respectively, and in figs. 4.9, 4.10 and 4.11. Fig. 4.9 is a plot of residual peak load against damage length and shows a linear relationship with the residual peak load decreasing with increasing damage length. Fig. 4.10, a plot of residual gradient against damage length, revealed an identical pattern to fig. 4.9,

Table 4.4a Static data from the initial tests for the 65mm test span specimens.

Specimen No.	Peak load (kN)	Deflection (mm)	Gradient (N/mm)	Energy to test end (J)
F9	3.00	1.63	2.17×10^{3}	2.07
F10	4.85	2.80	2.11×10^{3}	6.40
F11	5.20	3.85	1.89×10^{3}	10.87
F12	5.55	4.15	2.28×10^{3}	14.04
F4	5.85	3.35	2.39×10^{3}	36.66
F5	5.49	3.90	2.14×10^{3}	31.46
F6	5.95	3.80	2.25×10^{3}	34.71

Table 4.4b Static data from the residual property tests for the 65mm test span specimens.

Specimen No.	Peak load (kN)	Deflection (mm)	Gradient (N/mm)	Damage length (mm)
F9	6.45	3.05	2.89×10^{3}	-
F10	6.65	3.35	2.65×10^{3}	3.00
F11	6.08	3.25	2.16×10^{3}	5.00
F12	5.39	3.35	1.98×10^{3}	15.00
F4	3.46	7.80	0.60×10^{3}	32.00
F5	4.24	5.65	1.12×10^{3}	33.00
F6	4.40	6.90	1.02×10^{3}	40.00

Fig. 4.9 Graph of residual peak load against damage length for the 65mm span tests.

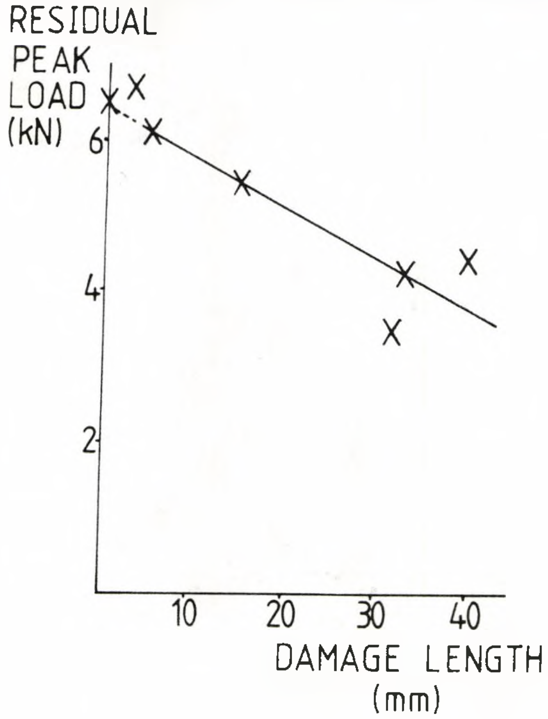

Fig. 4.10 Graph of residual gradient against damage length for the 65mm span tests.

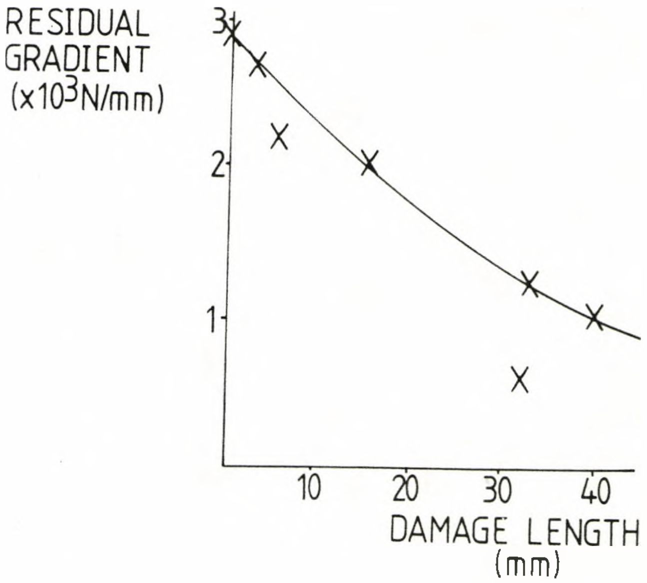

Fig. 4.11 Graph of residual deformation at peak load against damage length for the 65mm span tests.

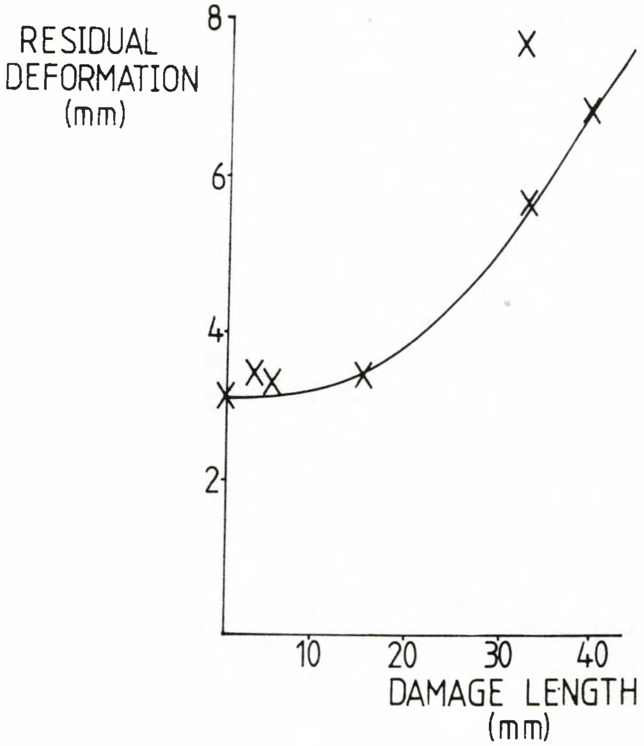

Fig. 4.12 Graph of incident energy against damage length for the 65mm span tests.

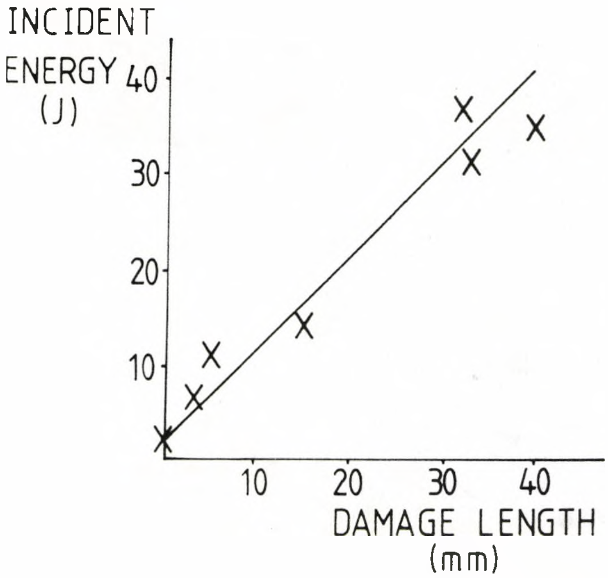

thus indicating increasing damage resulted in reductions in both strength and stiffness (characterised by peak load and gradient respectively). Fig. 4.11 is a plot of the residual deformation at peak load against damage length. Here, the pattern was that there was a cut off point below which increasing the amount of damage had no effect. Beyond this point (about 12mm damage length), the deformation required to cause failure rose rapidly.

It should be noted at this point why only the damage length parameter was considered and the answer lies in fig. 4.12. This is a plot of the initially applied (incident) energy against the damage length and is linear. Therefore, the same relationships were found between the residual properties and the incident energy as those already shown in figs. 4.9, 4.10 and 4.11, meaning that plots of residual properties against incident energy provide no further information and thus are not required.

4.4-3d) Microscopic examination of the damage.

As previously stated, the purpose of these tests was to aid in the damage process analysis by providing information about both delamination and resin crack morphology. Fig. 4.13 depicts the lower resin surface of a 500mm test span specimen and reveals details of one of the lower resin surface cracks. [N.B. In order to ensure that this feature was not simply a polishing aberration, a further specimen was photographed before sectioning and polishing]. Further information was provided by observing how the lower resin surface crack

Fig. 4.13 Photomicrograph of the lower resin surface of the 500mm test span showing details of the resin crack (x62.5). (T7)

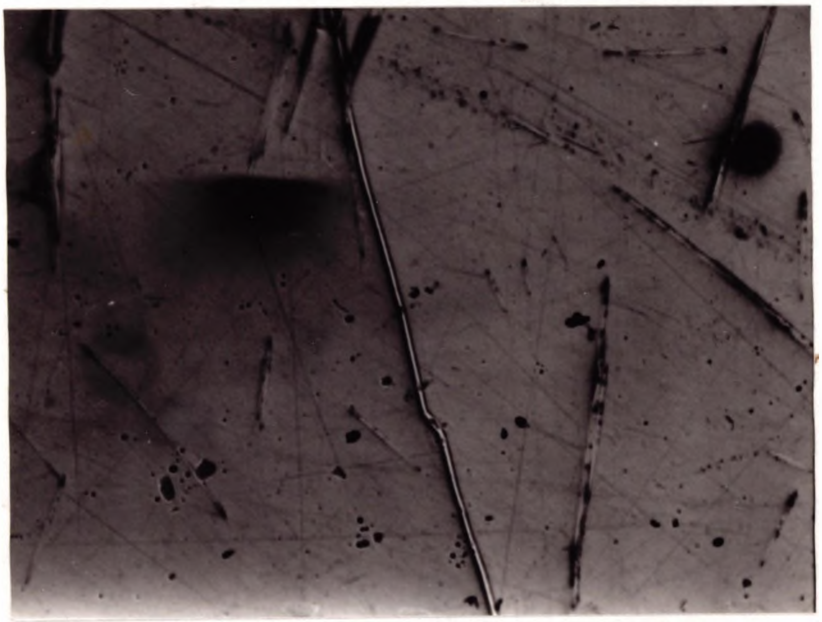

Fig. 4.14 Photomicrograph of the 500mm test span specimen revealing the path of the resin crack into the fibrous layers (x62.5). (T7)

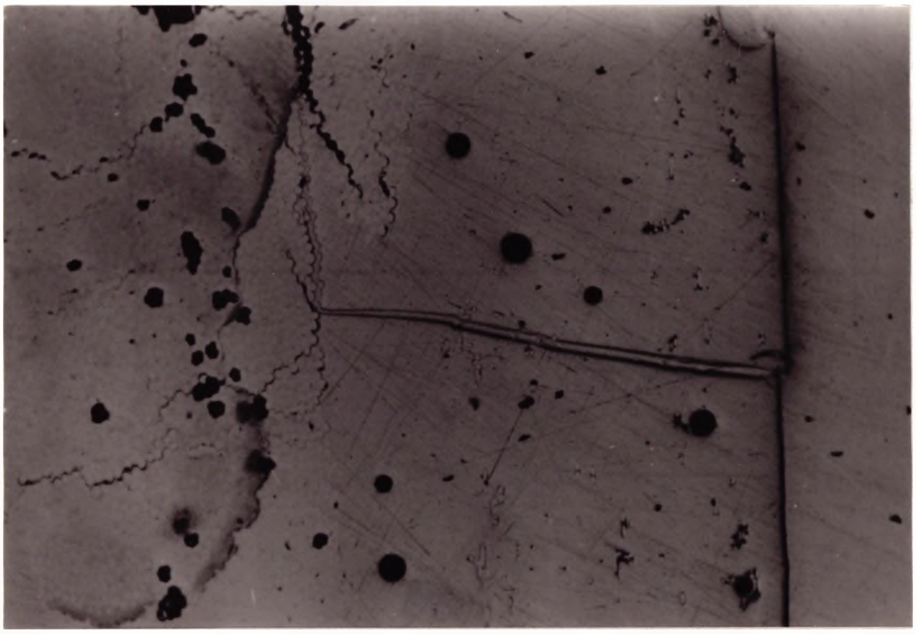

extended into the reinforced layers and this is revealed in fig. 4.14. The interesting thing to note here is though the crack did extend into the first fibrous layer before being arrested, it tended to follow a path around the individual fibres i.e. very little fibre splitting was seen. This pattern was repeated in all samples of similar amounts of damage examined.

Considering now the specimens with test spans of 65mm, as expected more damage was observed here. Fig. 4.15 shows the resin crack entering the fibrous layer and reveals two things. Firstly, both the resin crack itself and the hairline cracks seen in the first fibrous layer had expanded (compare with fig. 4.13), the latter resulting in discontinuities in the fibrous layer. Secondly, there was a huge delamination between the first and second fibrous layers (this being the major delamination mentioned when considering damage area (length) measurements in section 4.4-3c). It is interesting to note that once again there was little evidence of fibre fracture with the majority of the cracks and the delamination producing "clean breaks" i.e. their paths followed the fibre shapes.

Fig. 4.16 reveals what had happened further into a 65mm span specimen, showing the effect on the fibrous layers beyond the major delamination. It can clearly be seen that further delaminations have occurred, with the size of these decreasing the farther up into the specimen they go. Another feature revealed in this photomicrograph is the presence of transverse cracks,

Fig. 4.15 Photomicrograph of the 65mm test span specimen revealing the path of the resin crack into the fibrous layers (x62.5). (F4)

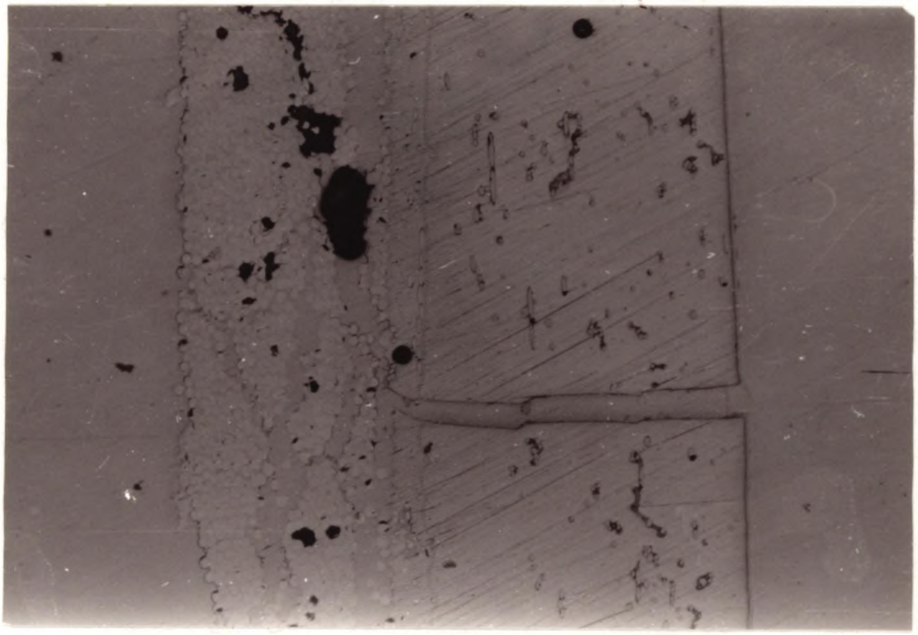

Fig. 4.16 Photomicrograph of the 65mm test span specimens revealing delaminated layers in the body of the composite (x62.5). (F4)

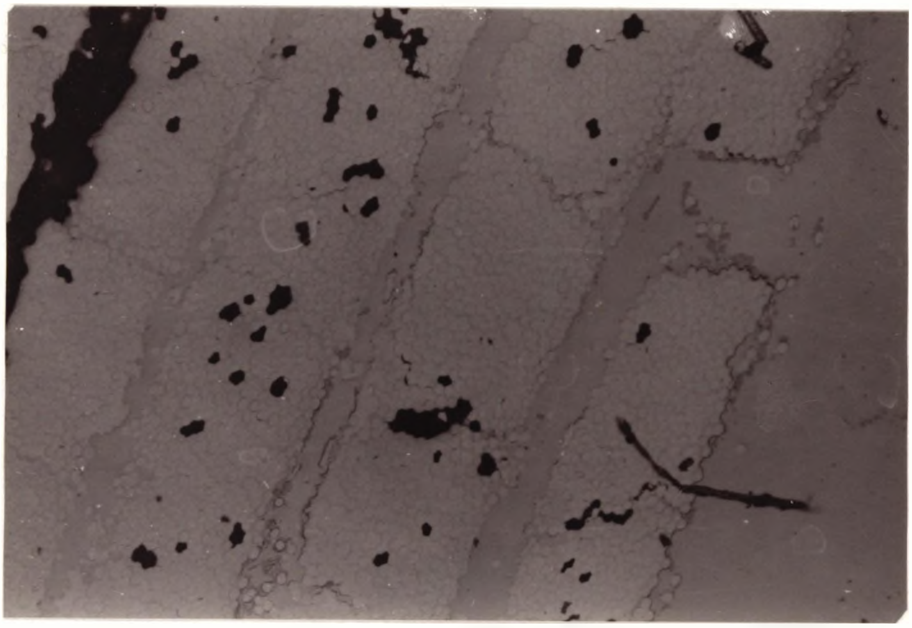

seen by the naked eye in the lower layers of the specimen, but also revealed to extend higher. These again revealed "clean breaks" at the fibre/matrix interface. This observation made throughout these microscopic examinations indicates the weakness of the fibre/matrix interface. Interlaminar bonding is also revealed as weak due to the delaminations formed.

It should be noted at this point that since the damaged specimens have been mounted in Scandiplast resin for polishing, what appear to be resin-rich areas in figs. 4.13 - 4.16 are in fact just regions where the Scandiplast resin has entered the specimen.

5. LARGE DIAMETER PIPE TESTING.

This chapter deals with experimental work carried out on large (400mm inner diameter) pipes. These were constructed with the same resin, reinforcement and winding angle as the small (150mm inner diameter) pipes so that comparisons between the two sizes could be made. Floor supported static tests and multiple bounce pipe drop impact tests were carried out, but in both cases different methods were employed from those already detailed in chapter 3, and these methods and the reasons for their use are explained below, followed by the results they yielded.

5.1 Static Tests.

All static tests were performed on the Instron 1195 (see section 3.1) with only the floor supported condition being considered. One problem which arose was the recurring theme of quality control, in this case with a variation in both wall thickness and glass content. Therefore, the thickness and glass content (determined by ash tests as described in section 3.4-1) are quoted in each of the test descriptions which follow.

There were three categories of static test:

5.1-1 Preliminary test.

This test was performed exactly according to section 3.1 to establish the load/displacement curve and the failure pattern. The test geometry is shown in fig. 3.1a and the test specimen was a 1m length of pipe of wall thickness 9/10mm and glass content V_f=62.8%. During this test, the surface in contact with the Instron plate failed and thus for subsequent tests, the pipes were supported on a flat 10mm thick aluminium plate. The Instron settings were also established for subsequent use as 5mm/min crosshead speed and 20mm/min chartspeed.

Once this test had been performed, the following modifications to the basic procedure were used to provide further information on the failure process.

5.1-2 Strain-gauged pipe tests.

These tests were carried out to monitor strain variations during the static testing. The first stage of the procedure of strain gauging was to establish the centre point of the pipe from which the required gauge positions could be determined. The positions were marked using an engraver. The area just to the left of the mark was sanded down using emery paper to smooth out any undulations in the gel coat. Once this had been completed, the mark was redrawn and the surface cleaned using M-Line CSM-1 Degreaser spray. It was very important that these preparatory steps were carried out with upmost care since abnormal results could be obtained by positioning the gauge on a rough surface or by positioning it even the slightest fraction out of line.

The gauge itself could now be applied and, to make the procedure easier, one single and one double terminal per gauge were also applied. For this series of tests, three types of gauge were used:-

i) EA-06-125TM-120 [R=120±0.2% Ω]

ii) CEA-06-125UT-350 [R=350±0.4% Ω]

iii) EA-06-125MW-120 [R=120±0.5% Ω]

Gauge types (i) and (ii) consist of one axial gauge and one hoop gauge on a rosette and are illustrated in fig. 5.1. [N.B. Gauge type (ii) was used as it produces an increase in accuracy.] Gauge type (iii) consists of 10 axial gauges contained on a strip of length 40mm. All three gauge types were made by MM Micro-Measurements Division, Measurements Group Inc., North Carolina.

Gauge and terminal application occurred as follows. To ensure alignment was exact, temporary application was intially made using sellotape. Once the alignment had been checked, the sellotape was peeled back and M-Line 200 Catalyst was applied to the back of the gauge and terminals and left for at least a minute. A bead of M-bond 200 Adhesive was then applied ahead of the gauge and terminals. As quickly as possible, the sellotape was pushed back and held down for at least a minute. Both gauge and terminals were now firmly attached.

The next stage was to attach wires to the gauges. Firstly, all the terminals were gently scratched to ensure good connections were made. Each "wire" used actually consisted of several wires enclosed in an insulating coat i.e. could be regarded as a group of wires. To make the connections, three groups of wire were necessary for each gauge. A single wire was separated from the others in its group, which were cut to a length of the order of millimetres, in two of the three cases. The connections were then made as is shown in fig. 5.1. [N.B. The gauge itself must not be touched by either

Fig. 5.1 Strain gauge rosette and terminals.

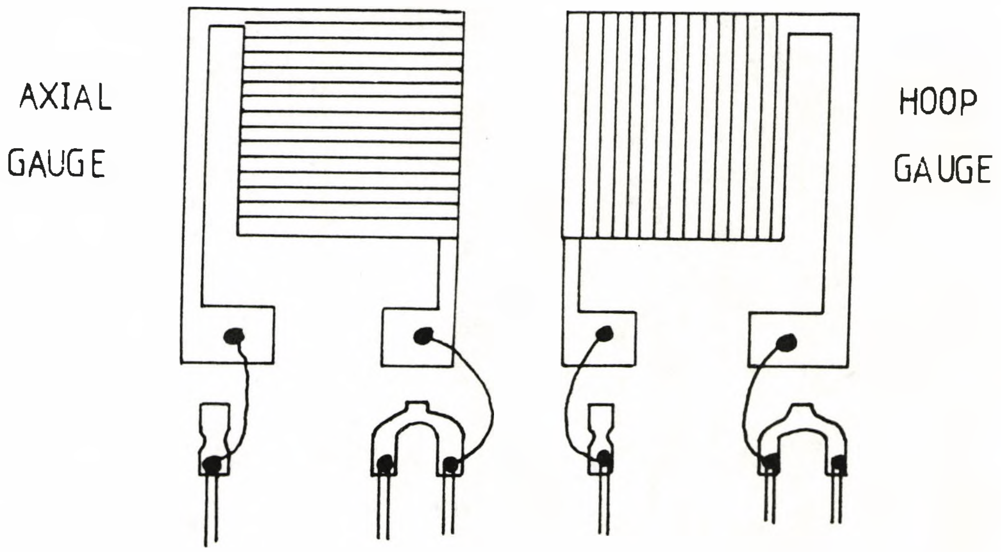

the soldering iron or the solder since this would render it useless. In the event of this happening, the gauge must be sanded away using emery paper and the process restarted.]

At this stage, it was useful to check that all the gauges applied were in good working order and this was done using a measurements group Gauge Installation Tester 1300 unit. This measured the resistance of the gauge along with its 5% and 1% deviations from nominal. If any abnormal readings were obtained, the gauge was deemed to be not working properly and was therefore replaced as in the note above.

Once the gauges had been checked and were known to be operative, it was necessary to protect both gauges and connections until use. This was achieved by initially applying M-Line Rosin Solvent all over the gauge and terminal area. Then M-Coat A was applied. [This is an air-drying polyurethane coating with a drying time of 20 minutes and a full cure time of 7 days, both at room temperature.] Finally, tape markers were used to mark the wires so that quick identification of the gauges was possible during the tests.

Three pipes were tested with strain-gauges attached in the above manner. The experimental setup is shown in fig. 5.2 and Instron settings for the three tests were as determined in section 5.1-1.

The first gauged pipe was of length 1m, thickness 9/10mm and had a glass content of 62.8%. Twenty operational gauges were fitted, 8 being of type (iii) and

Fig. 5.2 Experimental setup for the Strain-gauged pipe tests.

12 being type (i), as stated in table 5.1, and shown in fig. 5.3a. The test was initially conducted only to 22.25kN due to difficulties with the program used to process strain data (listed in the Appendix). This cut out as a gauge failed, resulting in strain data no longer being gathered. The test was halted as soon this became apparent, the program modified and then the test restarted. Unfortunatly, the modification did not prove successful and as a second gauge failed, the program cut out again, with the same consequence as above i.e. the strain data was not gathered. This resulted in the test being stopped at a load of 31.75kN.

The fault in the program was finally corrected and a second test was conducted on a pipe of length 1m, glass content 54.5% and with wall thickness varying from 13 to 15mm. [N.B. The non-uniform thickness of this specimen was due to the end of a tapered pipe being used. This tapering was only a problem for the large diameter pipes.] Twelve gauges were fitted, all of type (i), and these were placed as stated in table 5.2, and shown in fig. 5.3b. The test was conducted up to 49.50kN due to further difficulties with the computer program, which had been based on a full scale deflection on the Instron of 50kN. Altering the full scale deflection led to the program crashing, so the maximum load possible was just above 50kN. However, this was deemed to be sufficiently high a load to allow damage to be studied so it was decided to repeat the test with a pipe of uniform thickness.

Fig. 5.3a. Gauge positions for Test 1 with pipe viewed from above.

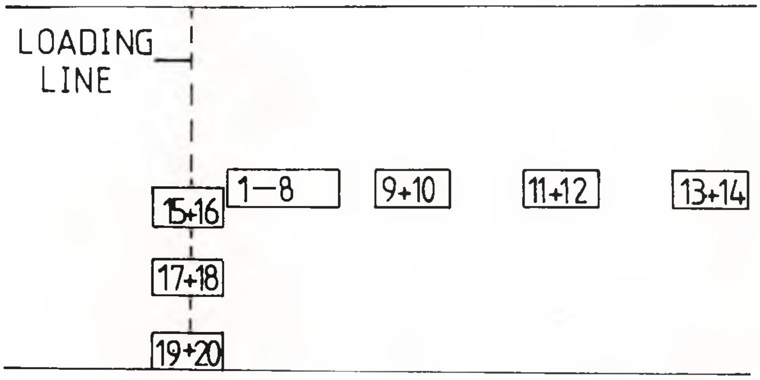

Fig. 5.3b. Gauge positions for Tests 2 and 3 with pipe viewed from above.

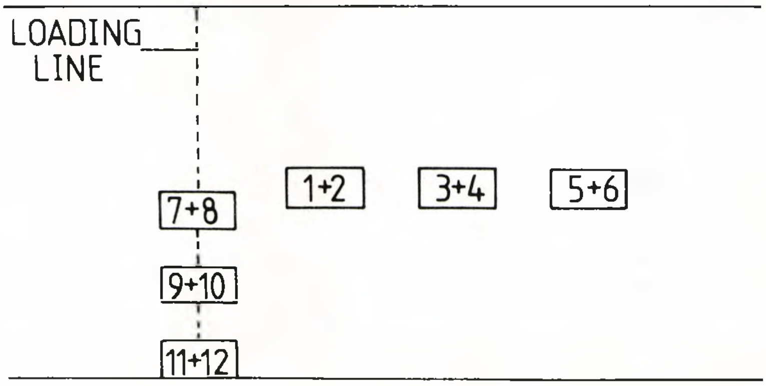

Table 5.1 Gauge positions for Test 1.

Gauge no.	Gauge position	Axial or Hoop?
1 -> 8	25mm->	Axial
9	100mm->	Axial
10	100mm->	Hoop
11	200mm->	Axial
12	200mm->	Hoop
13	400mm->	Hoop
14	400mm->	Axial
15	100mm|	Hoop
16	100mm|	Axial
17	200mm|	Hoop
18	200mm|	Axial
19	300mm|	Axial
20	300mm|	Hoop

Table 5.2 Gauge positions for Tests 2 and 3.

Gauge no.	Gauge position	Axial or Hoop?
1	85mm->	Axial
2	85mm->	Hoop
3	130mm->	Axial
4	130mm->	Hoop
5	170mm->	Axial
6	170mm->	Hoop
7	100mm|	Axial
8	100mm|	Hoop
9	200mm|	Axial
10	200mm|	Hoop
11	300mm|	Axial
12	300mm|	Hoop

Key for above Tables.

xmm->	Gauge positioned xmm from pipe centre in the axial direction.
xmm|	Gauge positioned xmm from pipe centre in the hoop direction.

The third pipe had length 1m, wall thickness 12/13mm and a glass volume fraction of 55.5%. It was also decided to increase the accuracy of the strain readings and so type (ii) gauges were used. Gauge positions were as in test 2 except that gauges 1 and 2 were placed at 80mm in the axial direction as opposed to 85mm. The test was conducted until the load reached 51kN.

The data from each of the three tests was fed from a Hewlett Packard (HP) 3852A Data Acquistion/Control unit into a HP Vectra. Information was stored using "Lotus 123" and graphs were modified for printing in "Lotus Freelance".

5.1-3. Tests performed to study the delamination process.

The tests in this category can be divided into two sections.

5.1-3a). Using video techniques.

Monitoring the pipe in this way allowed the velocity of the delaminations to be measured and the process of delamination growth to be studied. Three tests were conducted, all in accordance with section 5.1-1, except they were conducted much faster. This was because of the limited amount of videotape available for recording the failures. The delamination patterns were made clearly visible by conducting the tests with a strong light source located inside the pipe. Then, as soon as the damage was visible (i.e. usually just after the local crush and crack initiation point), the camera, which was a Kodak Ektapro 1000 Imager used at 500 frames per second, was started. The information was later transferred to VHS videotape for further reference. The experimental setup is shown in fig. 5.4. The camera was positioned to video one side of the pipe from the top so that the growth of delaminations in that direction could be monitored. Tests were stopped after the major delamination occurred. Individual test details are given below.

The first pipe tested had a length of 1m, a fibre volume fraction of 62.8% and a thickness of 9/10mm. The test, conducted at a crosshead speed of 50mm/min with the chartspeed adjusted to 100mm/min to obtain the clearest possible trace, was stopped at 38.50kN.

The second pipe tested had a length of 1m, a glass content of 55.5% and a thickness of 12/13mm. The test was conducted at a crosshead speed of 100mm/min with the chartspeed at 200mm/min initially, but this caused the Instron to stall. The settings were adjusted to those used in the first test and the test was restarted. The Instron stalled at 35.40kN and the test was stopped at 65.00kN.

The third pipe tested had a length of 2.5m, a glass content of 55.5% and a thickness of 12/13mm. The settings for the Instron were as in the first test, and the test was stopped at 82.60kN.

5.1-3b). Using a periphery camera.

Failure patterns from five of the seven tests conducted were recorded using a periphery camera. This is really a more sophisticated version of the backlighting

Fig. 5.4 Experimental setup for the "video" tests.

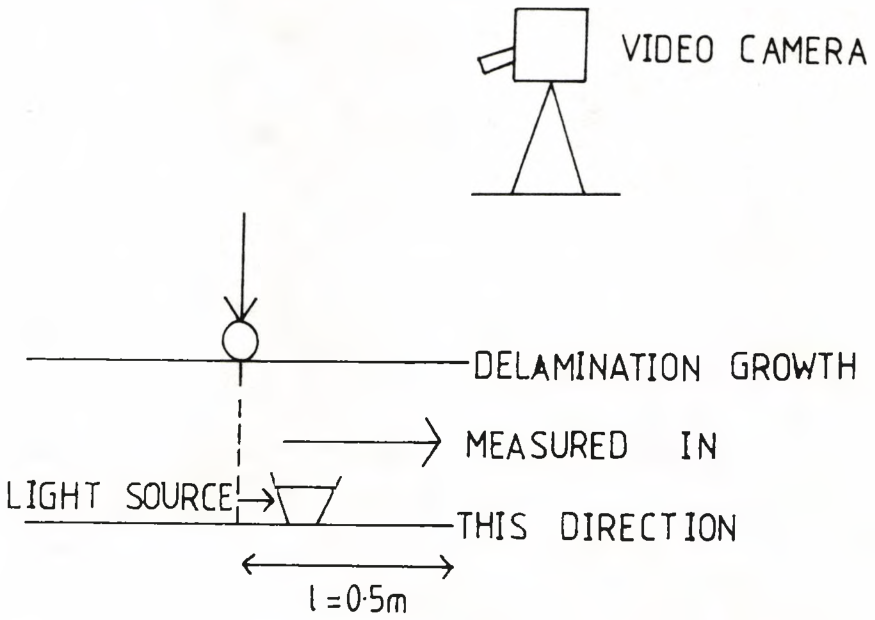

Fig. 5.5 Pipe rigged up for periphery photography.

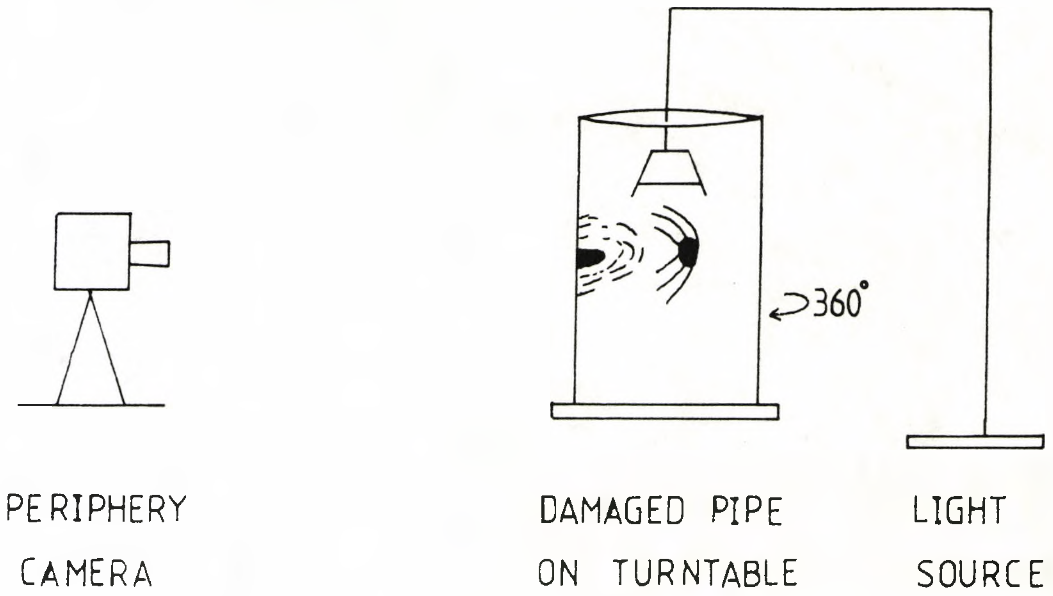

technique (see section 3.3-1b) developed by Shell Research. A strong light source was located inside the pipe which was mounted on a turntable as shown in fig. 5.5. This was rotated through 360° whilst the camera recorded the entire circumference of the pipe.

The pipes viewed in this way were all the "videoed" pipes, the first strain-gauged pipe and the preliminary test pipe.

5.2 Impact Tests.

In the case of the large diameter pipes, multiple bounce pipe drop impact tests were conducted on complete pipes of length 5m, wall thickness 12/13mm and fibre volume fraction 55.5%. The experimental setup is shown in fig. 5.6. This is a completely different situation to the small diameter pipe tests where the pipe was supported and was impacted by a falling weight. Here, the pipe itself was dropped and was prevented from swinging as it fell by guideropes. Tests were conducted in this manner partly to simulate the real situation of pipes being dropped as they are lowered into position and partly due to the 400mm inner diameter pipes being too large to fit under the impact rig. It would be useful in future to conduct falling weight tests on the large diameter pipes to compare with the pipe drop tests, but there was insufficient time to perform these during this project.

Five tests were performed with drop heights of 0.5m, 1.25m, 1.75m, 2.5m and 3m, corresponding to velocities of 3.13m/s, 4.95m/s, 5.86m/s, 7.00m/s and

Fig. 5.6 Impact test rig.

7.67m/s and incident energies of 828.1J, 2145.2J, 3003.3J, 4290.4J and 5148.9J. The pipes were dropped onto the same nose as was used in the static tests for direct comparison. The position of the first and subsequent impacts was marked using white spraypaint.

The impact was recorded in two ways. A video was taken of the centre of the pipe to record the change in diameter as it hit the nose. However, no indication could be obtained from this about how the impact affects the pipe as a whole. Therefore, a ciné film of the entire pipe was taken.

The impact damage was analysed in three ways. Firstly, weepage tests were performed, which involved filling the impacted pipes with water and pressurising them. The amount of weepage was recorded. Then, penetrant-enhanced X-ray radiographs and periphery photographs were taken to record the damage patterns. No residual property tests were conducted on these pipes. This is another candidate for future work.

5.3 Results.

5.3-1 Static Tests.

All seven of the pipes tested yielded a load/displacement curve, the basic shape of which is shown in fig. 5.7. After an initial elastic region, there is a region of slight non-linearity followed by a failure. This, as in the majority of tests conducted on various pipe diameters and sections, is not catastrophic i.e. it is not accompanied by any noise or by debris.

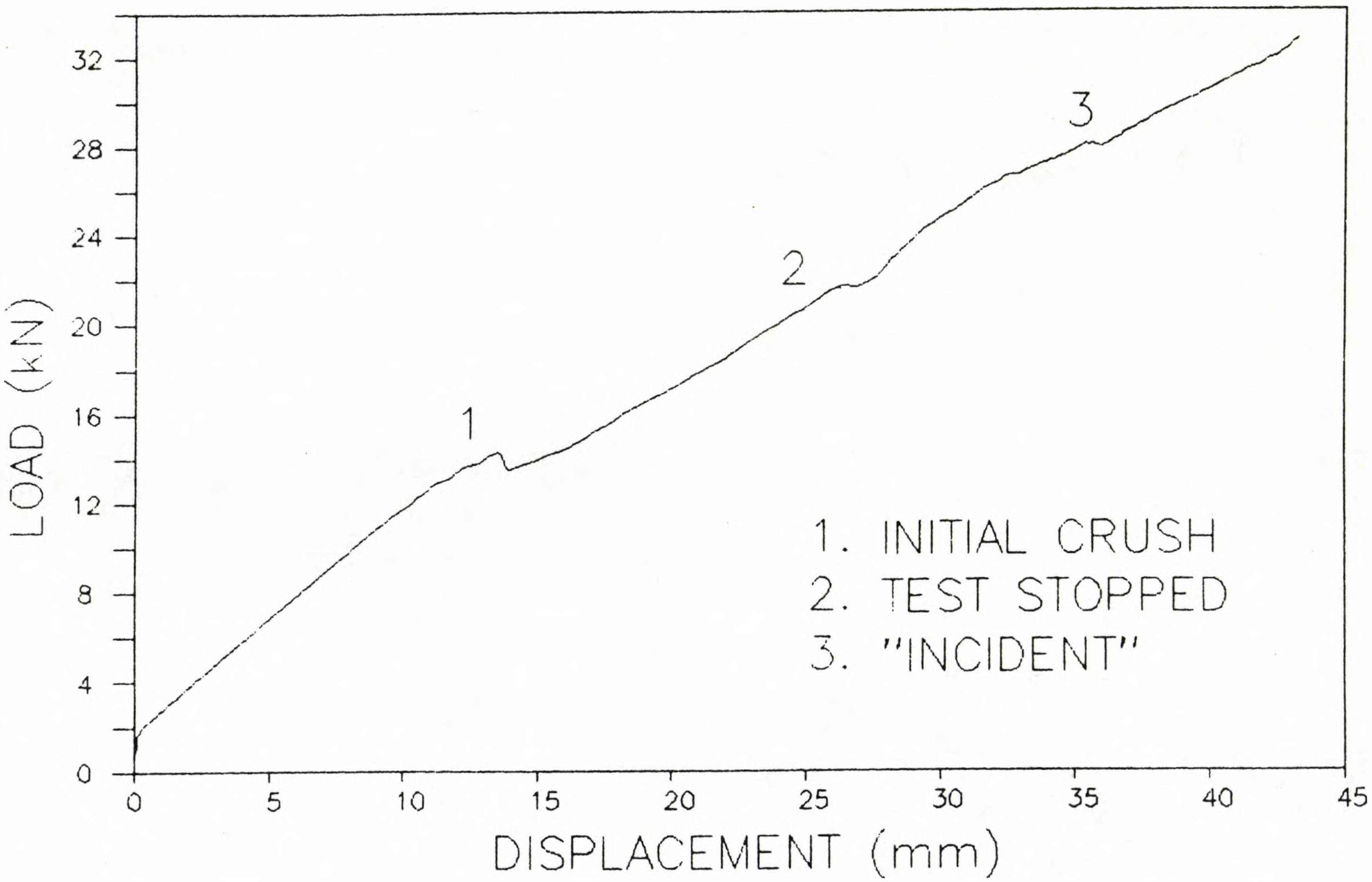

Fig. 5.7 Load/displacement curve for the large diameter pipes

This is equivalent to local crush damage, delamination initiation and lower resin surface cracking. It is not yet known in what order these events occur; they have always been assumed to be concurrent. The curve then continues with slight irregularities, marking further delaminations initiating, until a second major feature, marked 3 on the curve, occurs. This is a further failure point and, although not representing a large drop in load, is accompanied by much tearing and by a change in the gradient of the load/displacement curve. [N.B. There is nothing special about the point marked 2 - this is simply where this particular test was stopped due to problems with the strain data gathering program - see section 5.1-2]. The numerical information from all seven pipe tests is given in tables 5.3, 5.4 and 5.5, each table giving data to a different reference point, namely initial crush damage, second failure and test end.

The plot actually used for fig. 5.7 was produced by the first gauged pipe, but any six of the seven load/displacement curves could have been used. The one exception is the video three pipe i.e the 2.5m pipe tested and videoed at 50mm/min. In this case, the first failure was catastrophic, resulting in much internal damage. This manner of failure has been seen previously, but only as the second failure for the half pipes. It has never been seen in transverse tests as a first failure.

Further information on the failure process was obtained from the two types of tests performed and is detailed below.

Table 5.3 Static data up to the first (crush) failure.

Pipe no.	Thickness (mm)	Gradient (N/mm)	Deformation (mm)	Peak load (kN)	Energy (J)
Gauge 1	9/10	1.037×10^3	15.00	14.25	114.5
Gauge 2	13->15	2.058×10^3	12.50	24.50	173.9
Gauge 3	12/13	2.186×10^3	11.75	23.75	137.5
Prelim.	9/10	1.550×10^3	13.50	19.75	133.7
Video 1	9/10	1.040×10^3	14.00	14.50	101.5
Video 2	12/13	2.059×10^3	8.50	17.50	74.4
Video 3	12/13	2.333×10^3	14.75	32.75	245.6

Table 5.4 Static data up to the second failure.

Pipe no.	Thickness (mm)	Gradient (N/mm)	Deformation (mm)	Peak load (kN)	Energy (J)
Gauge 1	9/10	0.583×10^3	37.50	27.00	567.2
Gauge 2	13->15	0.929×10^3	35.25	41.85	876.9
Gauge 3	12/13	-	-	-	-
Prelim.	9/10	0.541×10^3	51.00	42.10	1304.9
Video 1	9/10	0.589×10^3	52.00	34.25	1043.1
Video 2	12/13	1.739×10^3	14.50	27.00	203.7
Video 3	12/13	0.893×10^3	49.50	59.00	1663.8

Table 5.5 Static data up to test end.

Pipe no.	Thickness (mm)	Gradient (N/mm)	Deformation (mm)	Peak load (kN)	Energy (J)
Gauge 1	9/10	0.632×10^3	46.00	31.75	815.1
Gauge 2	13->15	0.964×10^3	45.25	49.50	1316.9
Gauge 3	12/13	1.125×10^3	41.25	51.00	1188.4
Prelim.	9/10	0.333×10^3	99.75	52.00	3531.4
Video 1	9/10	0.500×10^3	65.50	38.50	1485.4
Video 2	12/13	1.821×10^3	71.00	65.00	2324.0
Video 3	12/13	0.700×10^3	81.00	82.60	3925.3

5.3-1a) Using the strain gauges.

Use of the strain gauges permitted the variation of strain during the pipe test to be studied. The three pipes tested in this manner generated a large amount of data which was converted into load/strain plots. Figures 5.8, 5.9, 5.10 and 5.11, four examples of these which yield information on the strain at all the positions considered, are summarised below:-

i) Fig. 5.8 - this is a plot of load/strain for the strip gauge placed at 25mm axially from the pipe midpoint in test 1. Six of the operational gauges are shown and they are all of the axial type.

ii) Fig. 5.9 - this is an enlargement of fig. 5.8 for loads up to 14kN. The reason for this was to observe more closely what is happening just before the first (crush) failure point.

iii) Fig. 5.10 - this is a plot of load/strain for the gauges placed at 100mm (9 and 10), 200mm (11 and 12) and 400mm (13 and 14) axially from the pipe midpoint in test 1. Gauges 9, 11 and 14 are of the axial type and gauges 10, 12 and 13 are of the hoop

Fig. 5.8 Plot of load against axial strain for Gauged pipe 1.

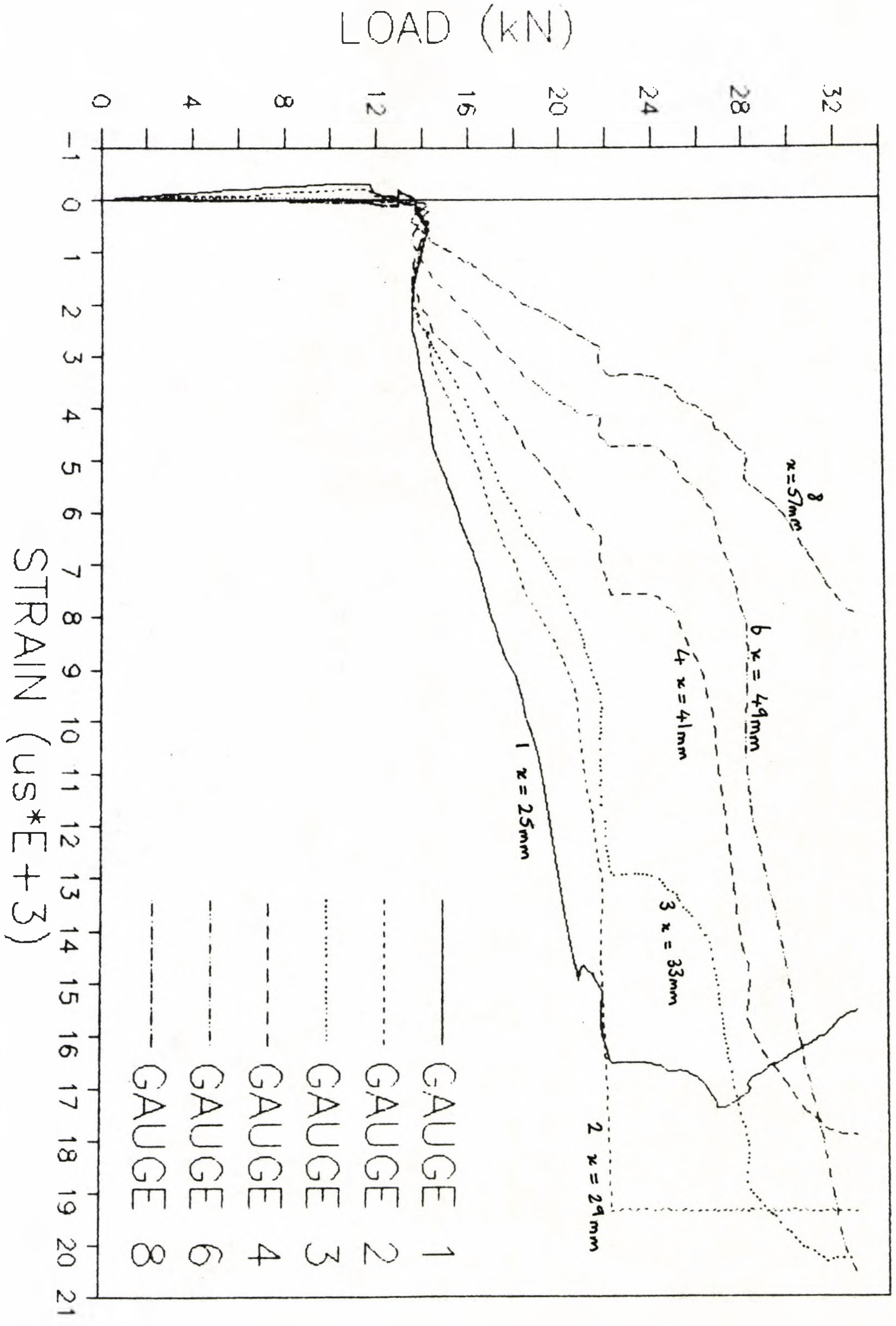

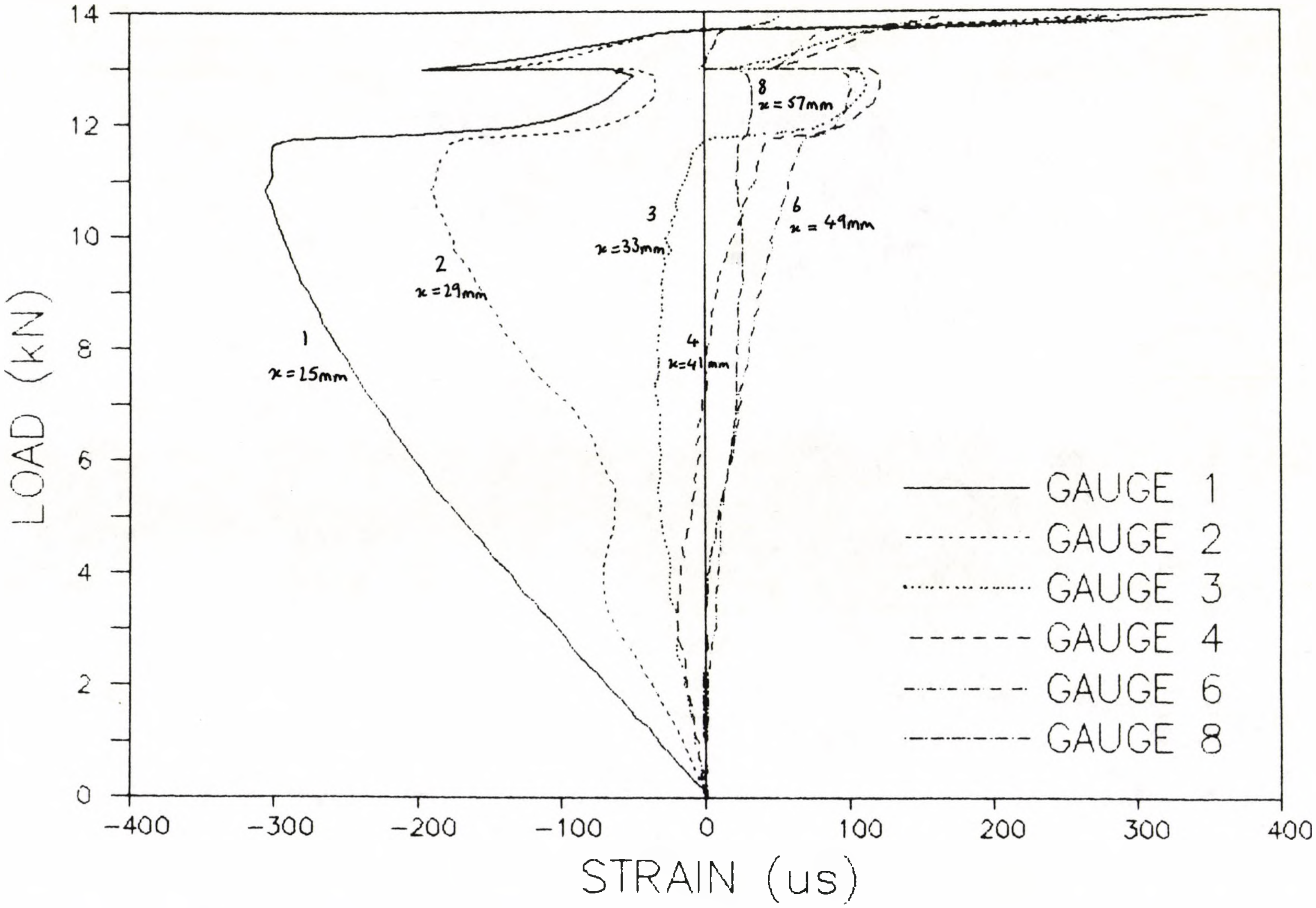

Fig. 5.9 Enlarged version of Fig. 5.8 up to 14kN.

Fig. 5.10 Plot of load against strain (both axial and hoop) for Gauged pipe 1.

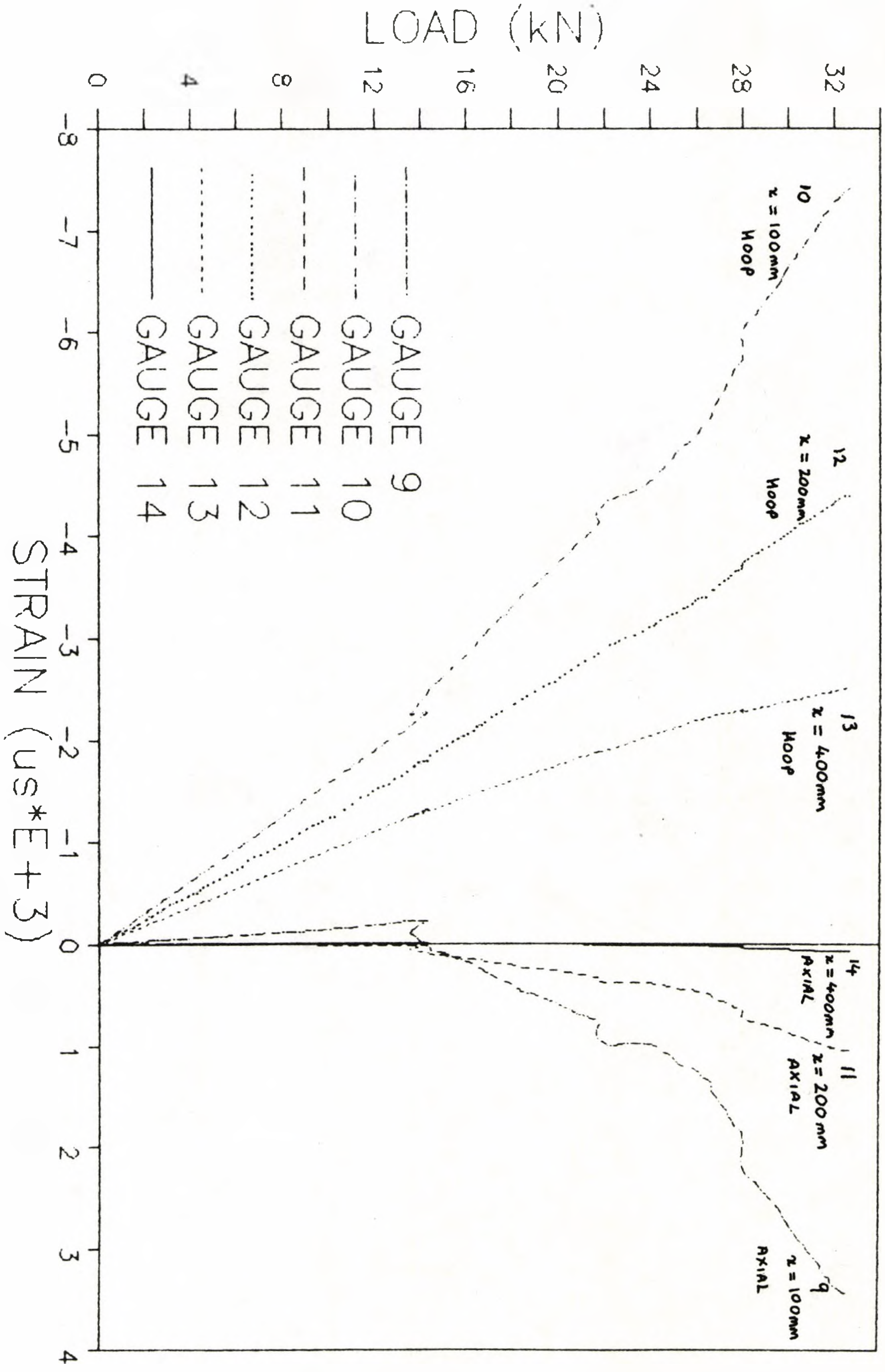

Fig. 5.11 Plot of load against strain (both axial and hoop) for Gauged pipe 2.

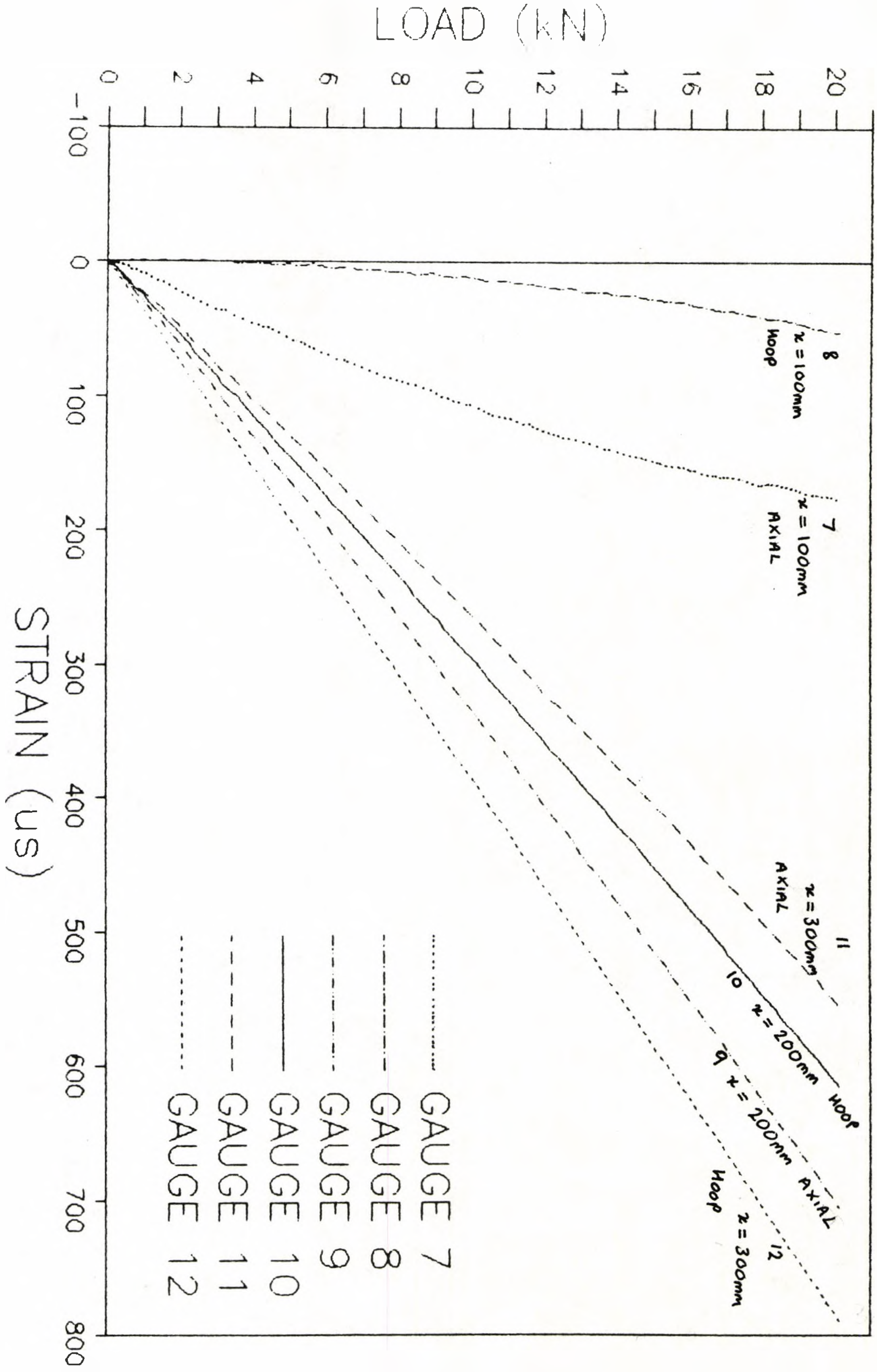

type.

iv) Fig. 5.11 - this is a plot of load/strain for the gauges placed at 100mm (7 and 8), 200mm (9 and 10) and 300mm (11 and 12) in the hoop direction from the midpoint of the pipe in test 2. Gauges 7, 9 and 11 are of the axial type and gauges 8, 10 and 12 are of the hoop type.

The significance of these plots will be further discussed in Chapter 8.

5.3-1b) Damage process analysis.

The damage process was analysed in two ways. The first was by video and from this, information was yielded about the method of delamination growth. This is best represented by a series of drawings (see figs. 5.12a, b and c) which illustrate how the delaminations grow, viewing growth from above and considering one side of the delamination only. The dotted line represents the loading line. Included in these figures is some indication of the speed of delamination growth. [It was possible to measure this because the film speed was known to be 500 frames per second i.e. one frame is equivalent to 2ms]. In general, the pattern was that slow, creeping growth occurred initially, in all 3 cases non-symmetrically. In two of the three cases, this speeded up just before the major delamination occurred. With the film

Fig. 5.12 Delamination growth viewed from one side of the loading line in:

a) Video test 1 b) Video test 2 c) Video test 3

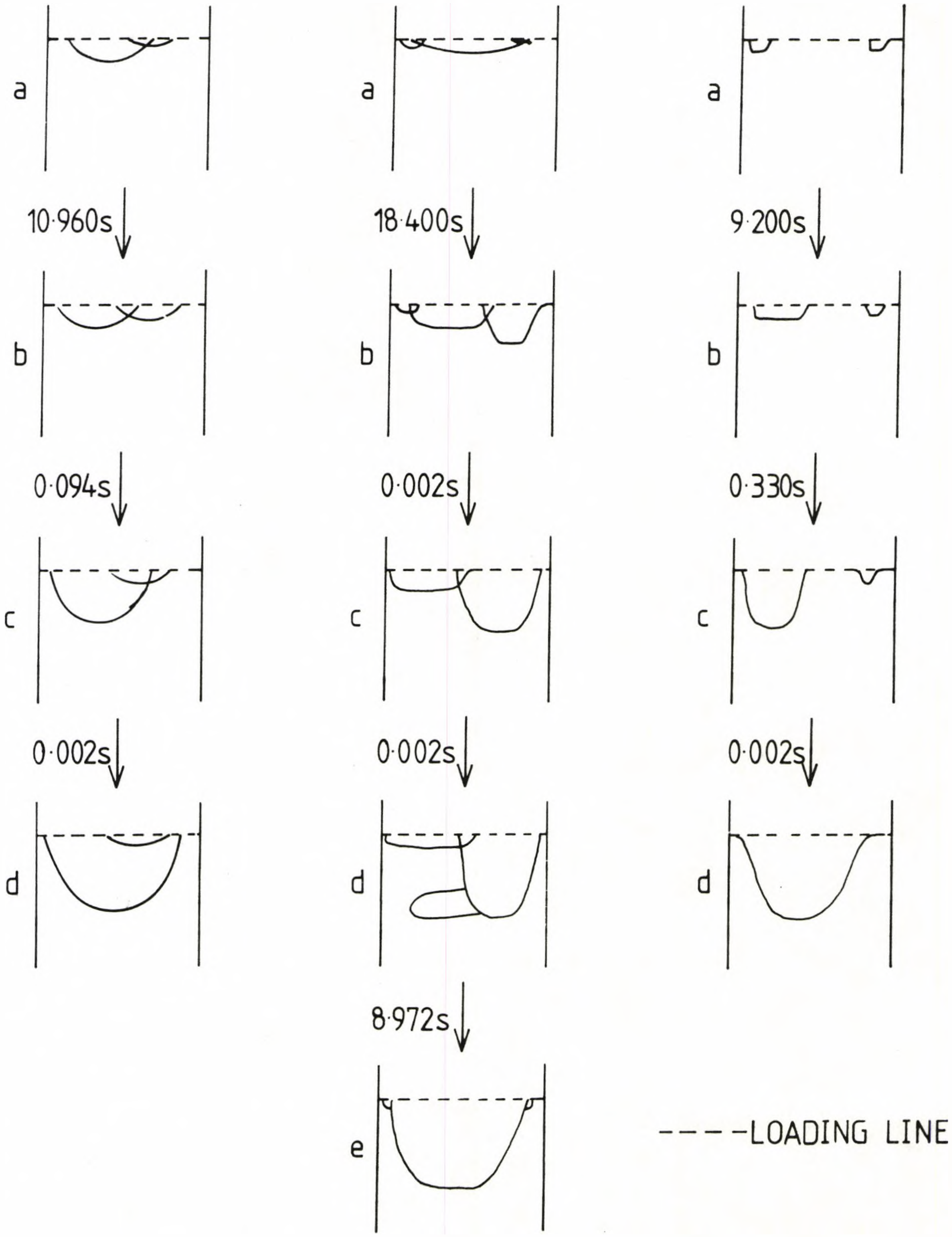

at normal speed, the growth appeared to be continuous but using the VHS frame advance option showed that the event actually occurred in just 1 frame i.e. in 2ms.

The second method of analysis was also a mapping method, looking at the delamination pattern after failure. This involved the use of the periphery camera and an example of the output from this technique is shown in fig. 5.13, which is a photograph of the preliminary damage test.

5.3-2 Impact tests.

Due to data being classed as confidential, only qualitative information was available for analysis i.e. the periphery photographs and the video of the pipe tests. The periphery photographs gave an indication of the damage sustained by the pipes under impact loading and comparison of these with equivalent static tests reveals that although the damage patterns are similar, more delaminations were found under impact conditions.

The video and ciné of the pipe tests were useful on two counts. Firstly, the video showed the almost complete recovery of the pipe shape after damage in all five cases. This was the situation found in all static and impact tests conducted. Secondly, the ciné revealed that the entire pipe was involved in the impact response, not just the region which hit the loading nose. This effect is in complete contrast with the static work where the nature of the tests prevents the large deformations of the pipe ends seen here.

It would have been useful at this point to have

Fig. 5.13 Periphery photograph of the Preliminary damage test.

performed falling weight tests on the pipes as well so that comparisons with the pipe drop and static tests as far as damage created could be made and once again it is suggested that any future work should include such tests.

6. SMALL DIAMETER PIPE TESTS.

This chapter deals with experimental work carried out on small (150mm inner diameter) pipes constructed from E-glass/epoxy resin with a winding angle of ±55°. These pipes were nominally identical, but variations in wall thickness and resin colour (probably due to either cure conditions or resin composition) were observed, leading to the series of quality assessment tests detailed in section 3.4 being carried out. The wall thicknesses of the pipes under test are quoted in each of the test descriptions below, with the remaining results given and discussed in section 6.3.

Static and both multiple and single bounce drop weight impact tests were conducted (88) in two loading geometries - floor-supported and cradled - and the basic test details are presented below, followed by the results they yielded.

6.1 Floor supported tests.

All tests in this geometry were conducted in the floor supported geometry (see fig. 3.1a) on pipes of length 500mm. The individual test types are considered separately below.

6.1-1 Static tests.

Static tests in this geometry were conducted in accordance with section 3.1 on the Instron 1185 tensile testing machine set up in compression mode. The load was applied at the midpoint of the top surface transverse to the pipe axis by a solid steel cylinder of length 150mm and diameter 25mm. For these particular tests, complete specimens were taken from 5m medium resin pipes of two different wall thicknesses. The complete cycle of tests [i.e. pilot and partial damage tests (documented in 3.1) followed by measurement of the damage introduced, by the backlighting technique (section 3.3-1b) and finally residual property tests to assess the effects of the pipe properties such as peak load, deflection to peak load and gradient (section 3.3-2b) were carried out on complete sections cut from two 5m pipes (one for the pilot tests and the other used in the partial damage tests), both of thickness 6mm. The complete load/displacement curve is shown in fig. 6.1 along with the points selected for partial damage tests. For comparison purposes, all but the residual property tests were also conducted on complete specimens cut from medium resin pipes of wall thickness 5mm.

In both cases, the 100kN load cell was used and the chartspeed and the crosshead speed (strain rate) were 20mm/min and 5mm/min respectively.

6.1-2 Impact tests.

All impact tests were performed on the large drop hammer rig using the 36kg tup with a maximum possible drop height of 8m and the same loading nose as in the static tests (see section 3.2). In this geometry, both multiple and single bounce tests were conducted. In order to obtain a direct comparison with the static tests, the single bounce impact tests were conducted on specimens cut from the same 5m pipe as the partial static tests

Fig. 6.1 Load/deflection plot for the static floor supported complete pipes of length 500mm.

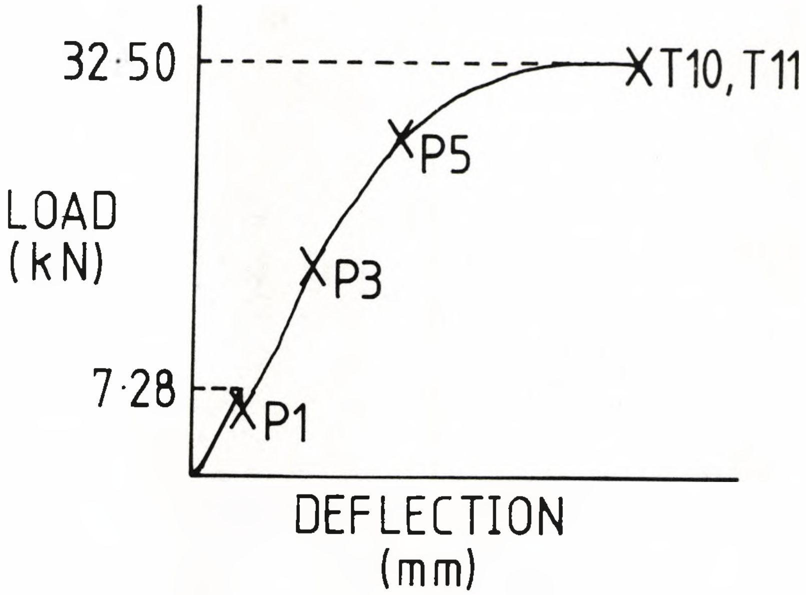

Table 6.1 Impact data for the floor supported complete pipes of length 500mm.

Specimen No.	Static energy (J)	Drop height (m)	Velocity (m/s)	Tup energy (J)
IP1, S1	20.84	0.060	1.08	23.05
IP3, S3	167.65	0.442	2.94	169.77
IP5, S5	370.98	0.978	4.38	375.64
IP11, S11	763.60	2.013	6.28	773.18
IP10, S10	1246.73	3.295	8.04	1265.60

Key : IPX = Multiple bounce impact tests.

SX = Single bounce impact tests.

(P1, P3 and P5) and two of the pilot tests (T10 and T11). The multiple bounce impact test specimens were cut from a further 5m length of medium resin pipe, again with a thickness of 6mm.

Both test types were conducted to mirror the static tests using the static energy to test end to determine the required drop height (see section 3.2), the drop heights and corresponding velocities and tup energies being listed in table 6.1. In order to obtain impact data that would be comparable with the static data (e.g. peak load, initial gradient etc.), the single bounce tests and the first bounce of the multiple bounce tests were instrumented using laser-doppler velocimetry, and from the velocity/time history, plots of energy/time, force/time, energy/displacement and force/displacement were obtained (see Chapter 2). The areas of damage produced by the impacts were measured by the backlighting technique and then residual property tests were performed on the pipes using the same Instron settings as in the static tests above.

6.1-3 Microscopic examination of the damage.

In order to gain as much insight as is possible into the damage process with the specimens available, the following series of tests was carried out on pipes which were then sectioned and observed in the Wild M8 Stereo Zoom microscope (as described in 3.3-2a). Static floor supported tests were conducted to first failure and to complete specimen damage on 500mm lengths of both light and medium resin pipes and to 15kN for a 500mm length of a light resin pipe only. Single bounce floor supported impact tests were conducted to energies equivalent to the static energies for first failure, loading up to 20kN and complete specimen damage on 500mm lengths of medium resin pipes only. The type of damage was recorded along with the layer numbers between which delamination occurred and comparisons were made between the damage caused by equivalent static and impact tests. Comparisons were also made between the damage found in medium and light resin pipes after equivalent static tests had been conducted. [N.B. All the pipes used in this work had a wall thickness of 6mm].

6.2 Cradled tests.

All tests in this section were conducted in the cradled geometry (see fig. 3.1b) on light resin pipes only of length 500mm and wall thickness 6mm. The individual test types are considered separately below.

6.2-1 Static tests.

Static tests in this geometry were conducted in accordance with section 3.1 on the Instron 1185 tensile testing machine set up in compression mode. The same cycle of tests as in the floor supported geometry was conducted on complete sections cut from one 5m length light resin pipe with the method of load application and the loading nose also being the same. The load/displacement curve to full specimen damage is shown in fig. 6.2, with the points selected for partial damage tests indicated on it. For both initial and residual

Fig. 6.2 Load/deflection plot for the cradled complete pipes of length 500mm.

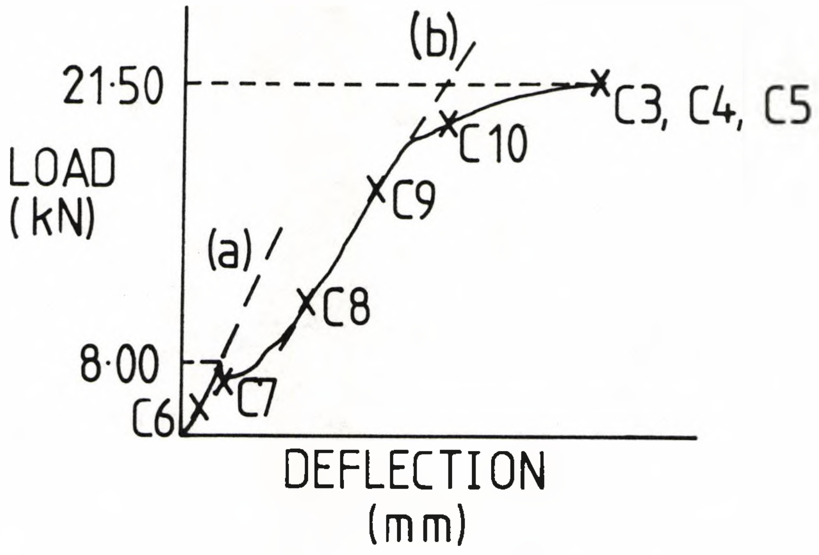

Table 6.2 Impact data for the cradled complete pipes of length 500mm.

Specimen No.	Static energy (J)	Drop height (m)	Velocity (m/s)	Tup energy (J)
L7	11.12	0.060	1.08	23.05
L8	67.34	0.185	1.91	71.06
L9	142.74	0.376	2.72	144.42
L10	354.19	0.930	4.27	357.20
L3	610.66	1.615	5.63	620.31
L4	443.97	1.175	4.80	451.31
L5	712.55	1.885	6.09	724.01

damage tests, the 100kN load cell was used and the chartspeed and crosshead speed (strain rate) were 20mm/min and 5mm/min respectively.

6.2-2 Impact tests.

All impact tests were performed on the large drop hammer rig using the 36kg tup with a maximum possible drop height of 8m in accordance with section 3.2 with the same loading nose being used as in the static tests. In this geometry, instrumented single bounce tests only were conducted on specimens all cut from a second 5m length of light resin pipe. Again, these tests were designed to be equivalent to the static tests by using the static energies to test end as a basis for determining the required drop heights (see section 3.2), the drop heights and corresponding velocities and tup energies being listed in table 6.2. [N.B. The differences between the static and tup energies is due to experimental error in the drop heights. In the case of L7, the required drop height of 2.9cm was too small to be obtained and so the test was conducted using a drop height of 6cm (the lowest available), resulting in a tup energy of 23.05J as opposed to 11.12J in the static test. It should also be noted that an equivalent test to C6 with an energy of 3.36J proved impossible to carry out]. The laser-doppler instrumentation recorded the velocity/time history, and from this, plots of energy/time, force/time, energy/displacement and force/displacement were obtained for further analysis. The areas of damage produced by the impacts were measured by the backlighting technique and then residual property tests were performed on the pipes using the same Instron settings as in the static tests above.

6.2-3 Microscopic examination of the damage.

Once again, in this series of tests the aim was to gain as much insight into the damage process as possible with the specimens available. To this ends, the following series of tests was carried out on 500mm lengths of pipe which were then sectioned and observed in the Wild M8 Stereo Zoom microscope (as described in 3.3-2a). Static cradled tests were conducted to first failure (light resin only) and to complete specimen damage, the latter for both a light and medium resin sample. Single bounce cradled impact tests were conducted to energies equivalent to the static energies for first failure and complete specimen damage on pipes with light resin only. The type of damage was recorded along with where delaminations were found and comparisons were made between equivalent tests conducted on pipes of different resin colours. Comparisons were also made between the damage caused in these tests and that found in the floor supported geometry.

6.3 Results.

Before discussing the results from the above, it is useful to consider results from the quality assessment tests. The methods involved in this series of tests and the reasons for carrying them out have already been discussed in section 3.4. There were three groups of tests, each considered separately below.

a) Ash tests.

These were conducted in order to obtain the glass volume fractions of the three different resin colour pipes i.e. dark, medium and light, which were all nominally 70% by weight glass fibres. Six small pieces of each resin colour were cut from a variety of pipes in order to include any variations from pipe to pipe and, in the case of the medium resin pipe, to include variations in wall thickness. Tests were conducted as described in section 3.4-1. Weight percentages were determined directly and from these, using equation 3.4, fibre volume fractions were obtained. These were then averaged for each resin colour and the results are listed in table 6.3.

As can be seen from this table, the glass volume fraction is very similar for the light and medium resin pipes (i.e. 55.7% and 56.2% respectively), meaning any differences in pipe properties between these two is unlikely to be due to variations in glass content. The dark resin pipes, however, do show a lower glass volume fraction of 52.7%, which could be one of the factors behind the weakness of this type.

b) Determination of the differences between the three resin colours by standard three point bend testing.

These tests were conducted in accordance with the British standard method (87) as described in section 3.4-2 in order to assess the differences in mechanical properties between the dark, medium and light coloured

Table 6.3 Glass fibre weight percentages and volume fractions for each resin colour.

Resin type	Fibre weight %	Fibre volume fraction
Light	72.0	55.7
Medium	72.5	56.2
Dark	69.5	52.7

Table 6.4 Properties obtained from the standard three point bend tests for each resin colour.

Standard properties	Resin colour					
	Light		Medium		Dark	
E_b (MPa)	7960	±950	6850	±830	7500	±1900
σ_f' (MPa)	114.7	±6.3	95.5	±8.5	89.7	±9.3
σ_f'' (MPa)	114.5	±9.0	112	±11	80	±14
ε' ($\times 10^{-3}$)	12.3	±1.4	12.1	±1.0	11.0	±1.1
ε'' ($\times 10^{-3}$)	37.8	±1.4	41.0	±2.9	37.2	±3.1
E' (J)	1.38	±0.17	1.00	±0.23	0.88	±0.14
E" (J)	6.20	±0.45	5.14	±0.60	4.10	±0.67

Fig. 6.3 The three load/displacement curve types for the standard three point bend tests.

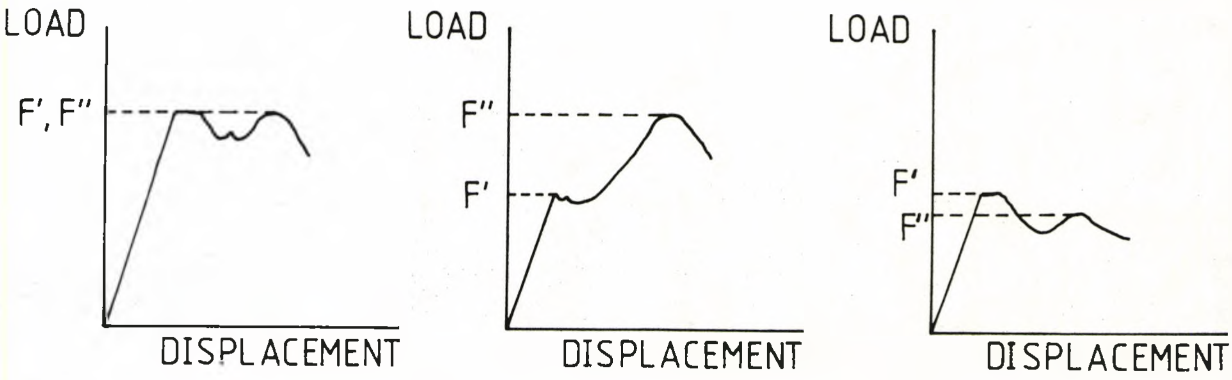

a) F' = F"   b) F" > F'   c) F' > F"

resins. Thirteen specimens from the dark and medium pipes and twelve from the light pipes were tested to obtain average values of the mechanical properties under consideration. These are listed in table 6.4, and were calculated from the load/displacement curves as follows:-

i) Modulus of flexure, $$E_b = \frac{L^3}{4bh^3}\ \frac{F}{d} \qquad (6.1)$$

ii) Flexural stress, $$\sigma_f = \frac{3FL}{2bh^2} \qquad (6.2)$$

iii) Flexural strain, $$\varepsilon = \frac{4hd}{L^2} \qquad (6.3)$$

where L is the test span, b the specimen width, h the specimen thickness, F the load at the point under consideration (see below) and d the corresponding deflection (and thus $\frac{F}{d}$ is the gradient). The energy values were simply found from the areas under the load/displacement curves. It can be seen that two values are quoted for all of the properties but the modulus of flexure. This can be explained by referring to fig. 6.3, which shows that the load/displacement curves encountered during testing have two distinct failure points, F' and F". Fig. 6.3 also shows that there were three different cases - i.e. where the two loads were the same, where F" was higher than F' and where F' was higher than F". Observing the failure process during testing revealed that first failure, F', resulted from the formation of the lower resin surface cracks. These cracks opened and widened as the test progressed. Then, after F" (the second peak), delaminations in the other layers occurred from the lower resin surface upwards. Therefore, since the two failure points were considered equally significant, values of flexural stress and flexural strain were calculated for both by feeding F', F", d' or d" where appropriate into equations 6.2 and 6.3, for example the flexural stress at the initiation of the first resin crack would be given by :-

$$\sigma_f' = \frac{3F'L}{2bh^2} \qquad (6.4)$$

The energy values E' and E" were simply the areas under the particular section of the load/displacement curves under consideration.

The first thing to comment on in these tests is that the medium resin pipes have F" higher than F' in a majority (10/13) of tests, indicating it is easier to crack the resin than to cause delamination. The reverse is true for the dark resin pipes in a majority (9/13) of curves. However, for the light resin pipes, there is no clear majority in any of the failure situations, indicating it is just as difficult to split the lower surface resin as it is to cause delamination.

Considering the first failure point, the light resin pipes had the highest properties across the board, indicating it is hardest to cause first failure (i.e. to initiate resin cracking) in these pipes. The pattern is repeated at second failure, although the medium resin values are now very close to the light resin ones with the flexural stress being equal within the margin of error. However, the dark resin pipes were much easier to delaminate, indicated by low values of flexural stress and energy.

The overall comments from this part of the quality assessment tests are that the light resin pipes are the strongest in flexure , followed closely by the medium resin pipes. The dark resin pipes exhibited the worst properties, indicating it was easiest to initiate cracking of the lower resin surface and especially to cause delaminations. The latter points to the interlaminar bond being weakest in these pipes. These findings confirm those already noted in the testing of the three different coloured resin pipes.

c) Microscopic investigation of the three different coloured resin pipes.

Microscopic examinations were carried out in order to investigate if there were any physical differences between the dark, medium and light resin pipes other than the obvious one of resin colour. Since it is already known that the glass content of the medium and light resin pipes is very similar, it was hoped that these tests would reveal differences in pipe layup and microstructure which could then be used to explain the differences obtained in mechanical properties both in the standard and scheduled testing. Specimens from pipes of each resin colour were prepared for observation as in section 3.4-3 and the following investigations were carried out.

Firstly, the number of layers in each of the dark, medium and light coloured resin pipes was counted at a magnification of x6. This revealed that both the dark and medium resin pipes had 12 composite layers encased by two gel coat (resin) layers whereas the light resin pipes had 19 layers, 17 of which were composites and two gel coat. [N.B. This increased number of layers is constructed to improve the weepage resistance of the pipes.]

Photographs were then taken of the specimens at x100 and enlarged to x350 to measure the thickness of both gel coat and composite layers for the dark, medium and light resin pipes. The results from this investigation are presented in table 6.5. This reveals that in all cases the (inner) lower resin surface was at least twice the thickness of the (outer) upper gel coat layer. Comparing the three resin colours reveals that the light resin pipes have the thickest resin layers and the medium resin pipes the thinnest. The reverse is true for the reinforced layers.

Finally, photographs were again taken and this time enlarged to x125. The interlaminar bonding and void content for specimens of each resin colour were examined. [N.B. When regarding figs. 6.4, 6.5 and 6.6, it should be noted that the ripped fibre edges seen are due to the polishing technique]. Fig. 6.4, a light resin pipe specimen, reveals very good interlaminar bonding with excellent ±55° boundaries. The layers were very difficult to spot as separate entities, though it should be noted that even in these specimens there is a high void content. Fig. 6.5 is a micrograph of a medium resin sample and reveals the typical mixed interfaces seen in these specimens i.e. following a single interface down

Table 6.5 The thicknesses of the composite and gel coat layers for the three different resin coloured pipes.

Resin Colour	Pipe thickness (mm)	Thickness in mm of upper resin	lower resin	composite
Light	6.52	0.24	0.54	0.34
Medium	6.38	0.10	0.32	0.50
Dark	6.35	0.16	0.44	0.48

Fig. 6.4 Photomicrograph of a ±55° boundary in a light resin pipe specimen (x125).

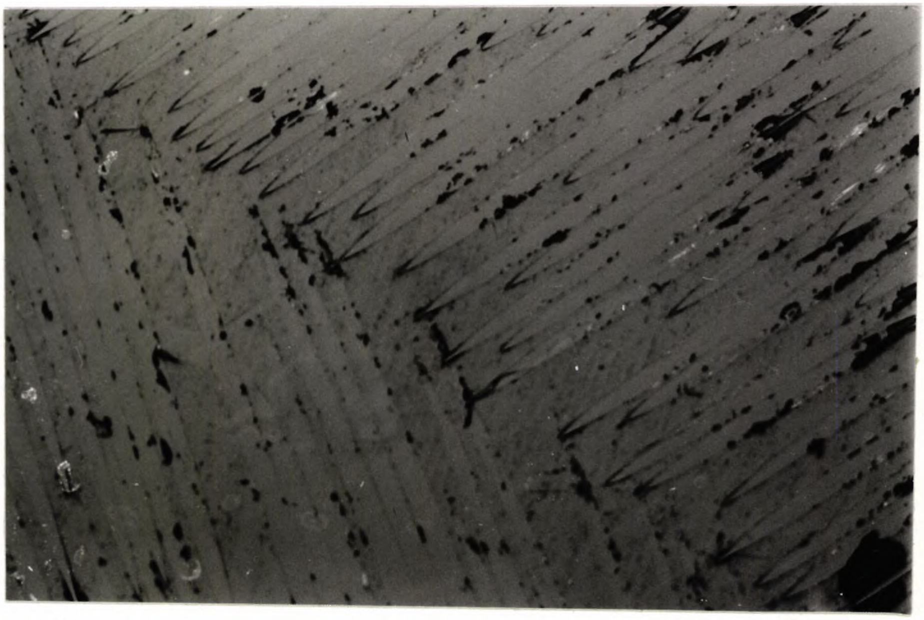

Fig 6.5 Photomicrograph of a ±55° boundary in a medium resin specimen (x125).

Fig. 6.6 Photomicrograph of a ±55° boundary in a dark resin specimen (x125).

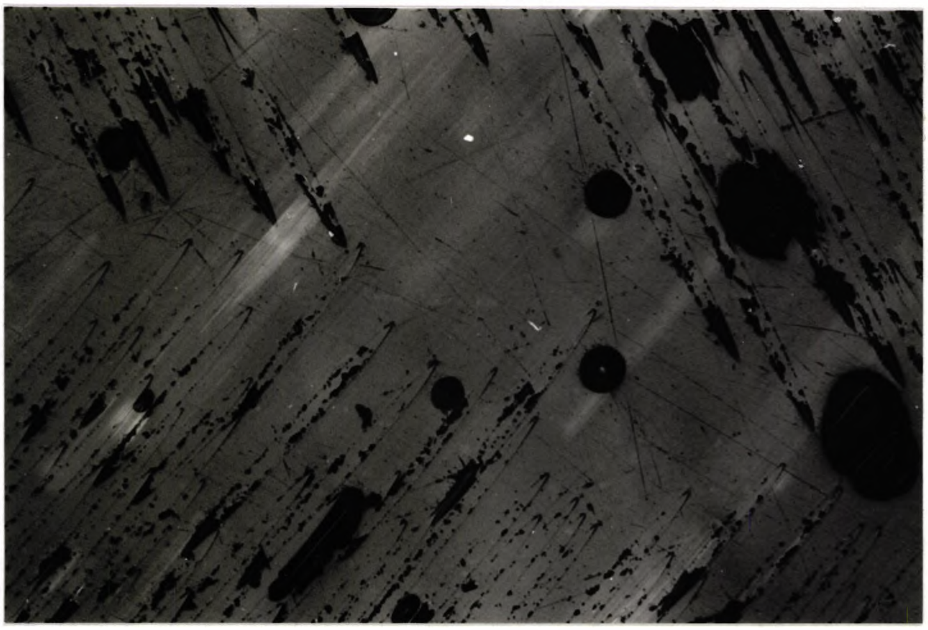

reveals regions of very good bonding next to regions of very poor bonding. The composite layers were now relatively easy to resolve and the void content was higher than in the light resin case. Finally, fig. 6.6 reveals the microstructure for the dark resin pipes. This shows large gaps at the ±55° fibre/resin interfaces, indicating interlaminar bonding is very poor. The layered structure was very pronounced but the void content was found to be similar to that in the medium resin pipes.

Summing up the findings of the three quality assessments, the following is revealed. The light resin pipes were the strongest in flexure, i.e. had the highest mechanical properties, and also were slightly thicker, had the most reinforced layers, thickest gel coats and the best interlaminar bonding. The dark resin pipes had the lowest mechanical properties, i.e. were the weakest, especially for delamination. They were also the least well constructed, having the worst interlaminar bonding and the lowest glass content. The medium resin pipes had the middle values of mechanical properties, despite having a slightly higher glass content than the light resin pipes. The reasons for the differences in properties are revealed when regarding the pipe microstructures - these have fewer layers than the light resin pipes and also thinner gel coats.

[N.B. It should be noted at this point that the pipe manufacturers were contacted about the variations in nominally identical pipes and they confirmed that the same resin had been used in each of the three cases, but that a variation in cure conditions probably resulted in the three different resin colours].

The above considerations were then taken into account when comparing tests carried out on pipes and pipe sections of the three different resin colours.

6.3-1a Initial tests on Floor supported pipes.

Fig. 6.7(i) shows the load/displacement curve for T10 i.e. to full specimen damage. The curve had two distinct regions, indicating a 2-part failure process, (88). The first region (up to point a) represents elastic behaviour to a first discernible failure point. After this, the load continued to increase but at a slower rate, marked by a less steep gradient, with progressive damage until a second major failure (marked c) occurred. Although the test was accompanied by much tearing, it is not catastrophic and despite the huge deformations involved (up to 55mm), the pipe recovers nearly all of its original shape. Superimposed on the static curve in fig. 6.7(i) is the dynamic force/displacement curve for IT10, which was a multiple bounce impact specimen tested to equivalent energy as T10. The dynamic curve followed a similar pattern to its equivalent static curve i.e. an overall increase in force (F) with displacement (d) but also included a large vibratory effect (further analysed in chapter 7). Once more, despite large deflections observed in the tests (over 70mm), almost all the deformation was recoverable.

Fig. 6.7(i) Comparison of static and impact load/displacement curves for specimens T10 and IT10.

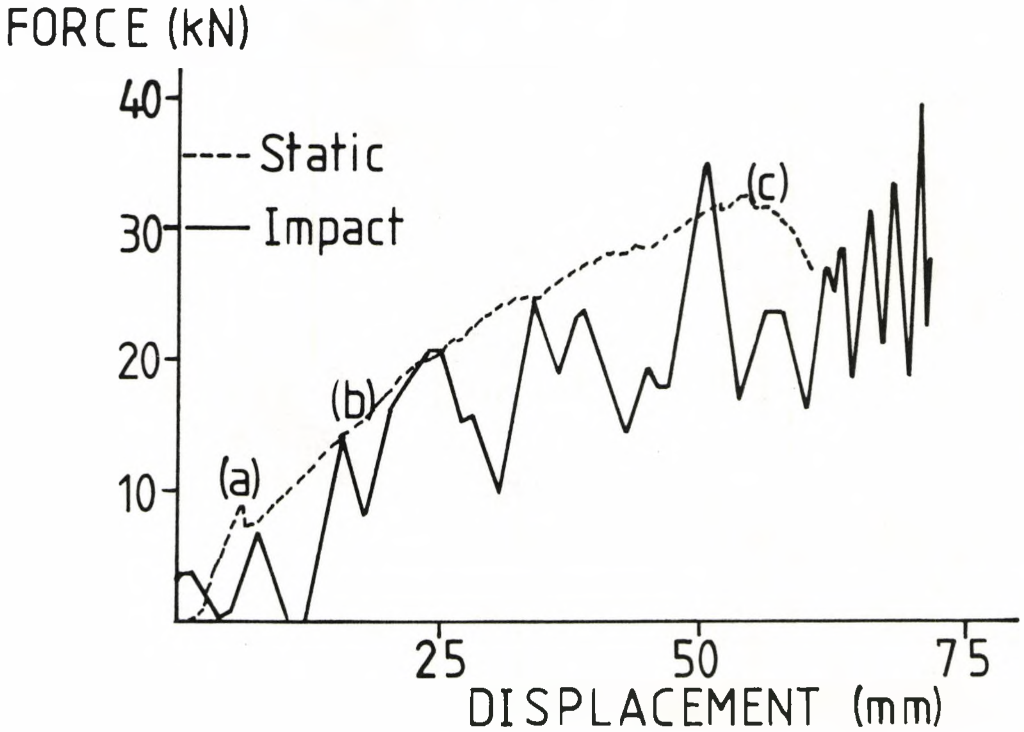

Fig. 6.7(ii) Schematic representation of delamination development: (a) after initial damage; (b) after loading to 15kN; (c) at test end.

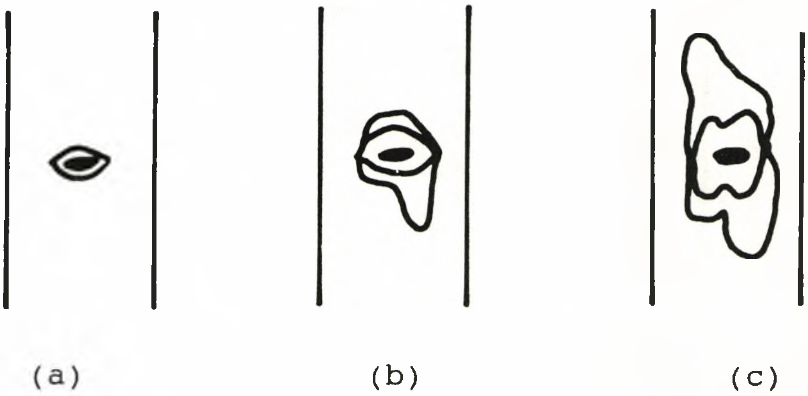

In all three cases i.e. static, single bounce and multiple bounce impact tests, the basic upper resin surface damage pattern consisted of an indentation mark (or crush crater), gel coat cracking and regions where the tup nose entering had caused the resin to shear away. This damage was of a similar nature for all the tests conducted with the only real difference being degree of severity, which was ordered static tests, single bounce impact tests and with multiple bounce impact tests being the most severely damaged as expected. The delamination patterns were observed by the backlighting technique and examples of each test type are shown in figs. 6.8, 6.9 and 6.10, representing the equivalent energy tests T11 (static), S11 (single bounce impact tests) and IT11 (multiple bounce impact tests) respectively. These reveal that the static tests show the least damage (with a total delamination area of $0.1491m^2$) followed by the single bounce tests ($0.2590m^2$), with the multiple bounce tests (as expected) being the most damaged (total delaminated area of $0.2792m^2$).

After tests to full specimen damage had been completely analysed, partial damage tests were carried out (see fig. 6.1 and table 6.1). As already stated, there were two reasons for performing these tests. The first of these was to observe how the damage built up during the tests (and thus to study the damage process) and this aim was achieved for all three test types. Considering firstly the partial static tests, photographs were taken of the delamination patterns revealed by the

Fig. 6.8 Photograph of pipe delamination obtained by the backlighting technique for T11 (static).

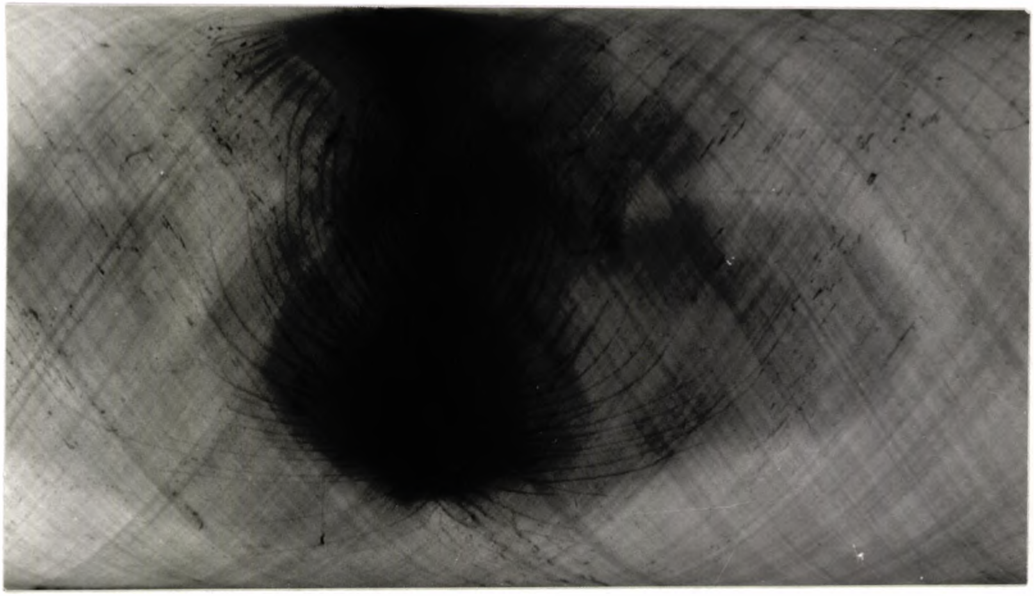

Fig. 6.9 Photograph of pipe delamination obtained by the backlighting technique for S11 (single bounce impact).

Fig. 6.10 Photograph of the pipe delamination obtained by the backlighting technique for IT11 (multiple bounce impact).

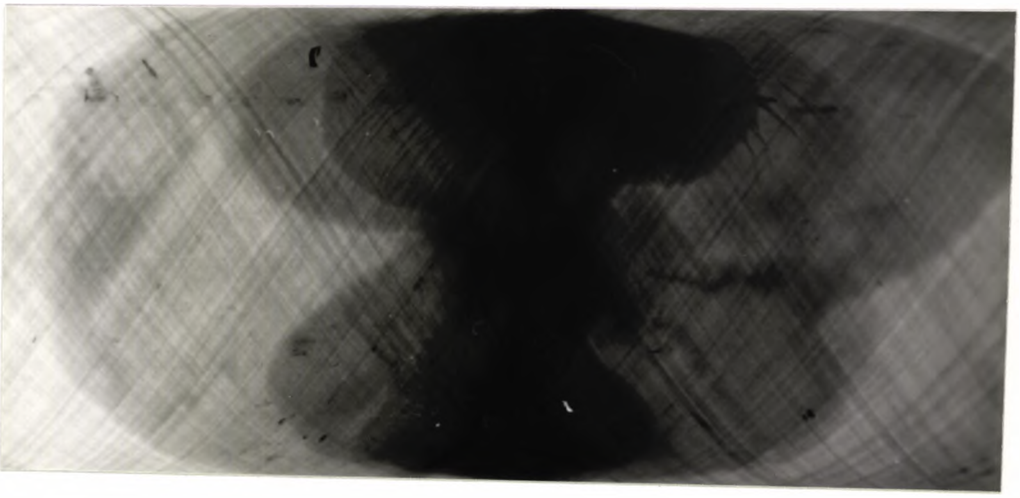

backlighting technique for specimens P1, P3, P5, T11 and T10 and sketches of these are presented in fig. 6.7(ii). Fig. 6.7(ii)a shows the damage for P1 i.e. after first failure. Here, the local crush indentation mark was visible and delamination had been initiated. Fig. 6.7(ii)b shows the damage at 15kN (P3), which is half the load to second failure. Further delaminations had occurred and these continued to grow until failure was reached, indicated by fig. 6.7(ii)c (for T10). It should be noted that the damage also built up in the same way for the single and multiple bounce impact tests, but was more severe in both these cases with the multiple bounce tests again being the most badly damaged.

The buildup of damage was further studied for static and single bounce floor supported impact tests by axially sectioning selected pipes as shown in fig. 6.11. Before any of the damaged specimens could be observed, the axial face of an undamaged section was observed and photographed at a magnification of x9 (see fig. 6.12) to act as a control i.e. to show that no damage was introduced as a result of the sectioning and polishing process. The damaged specimens were then observed and axially photographed, also at x9. Taking static testing as a basis for analysis, and considering behaviour at first failure, the very localised effects were immediately apparent. A crazing type pattern (see fig. 6.13a, which was a medium resin sample) was observed directly under the loading nose while a short distance away, the pipe material was completely unaffected (see

Fig. 6.11 Schematic showing how sectioning took place.

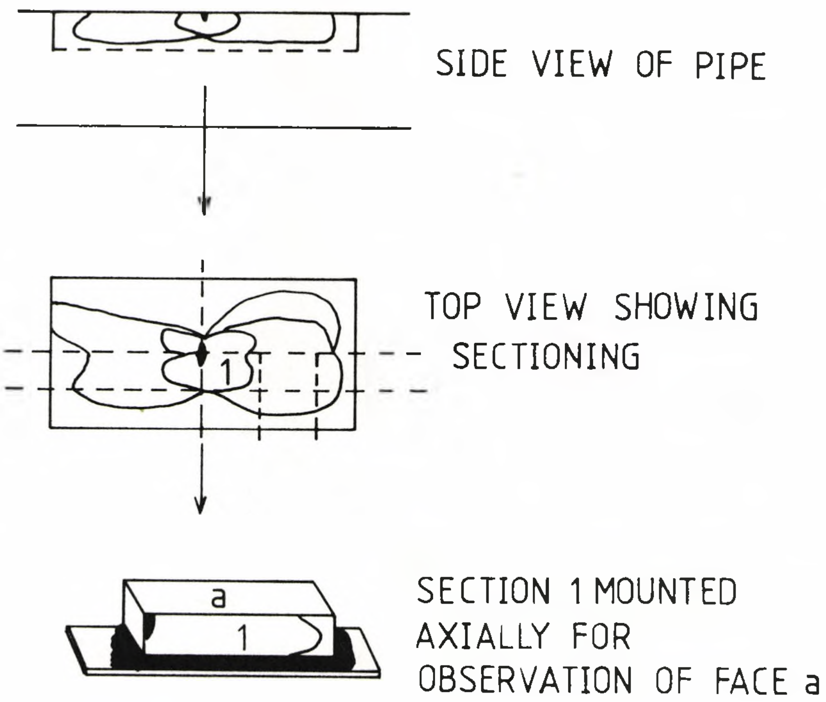

Fig. 6.12 Photograph of the undamaged (control) specimen (x9).

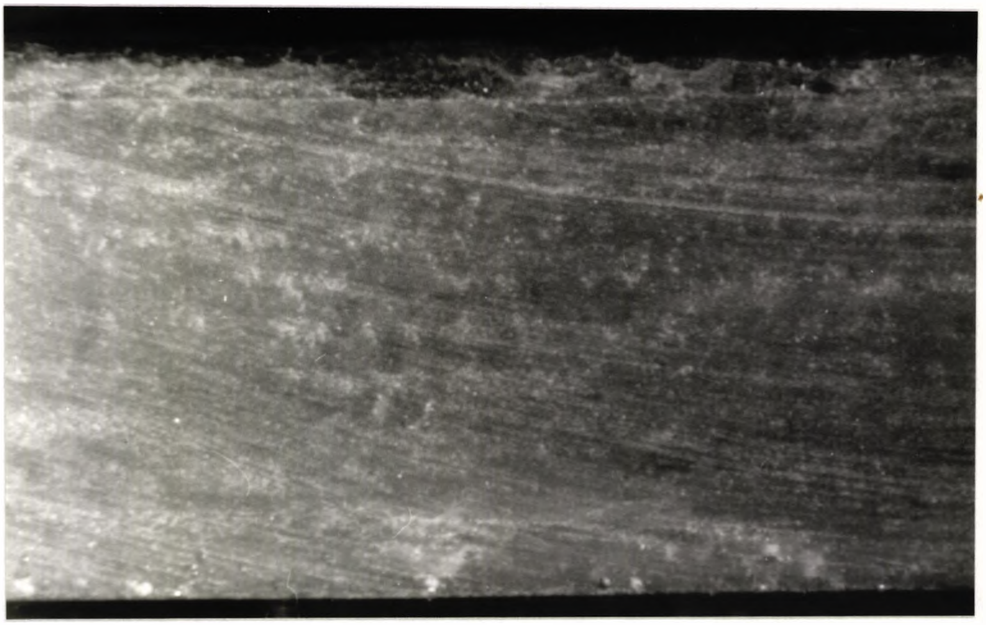

Fig 6.13a Photograph of the damage seen in the pipe (x9) at first failure.

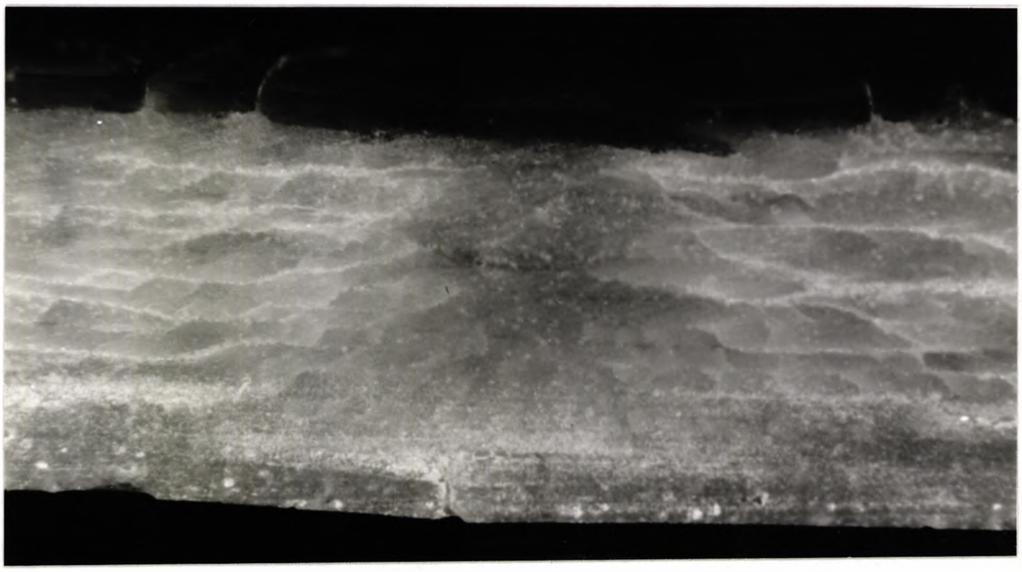

Fig. 6.13b Photograph of the same pipe section a short distance from the loading nose (x9).

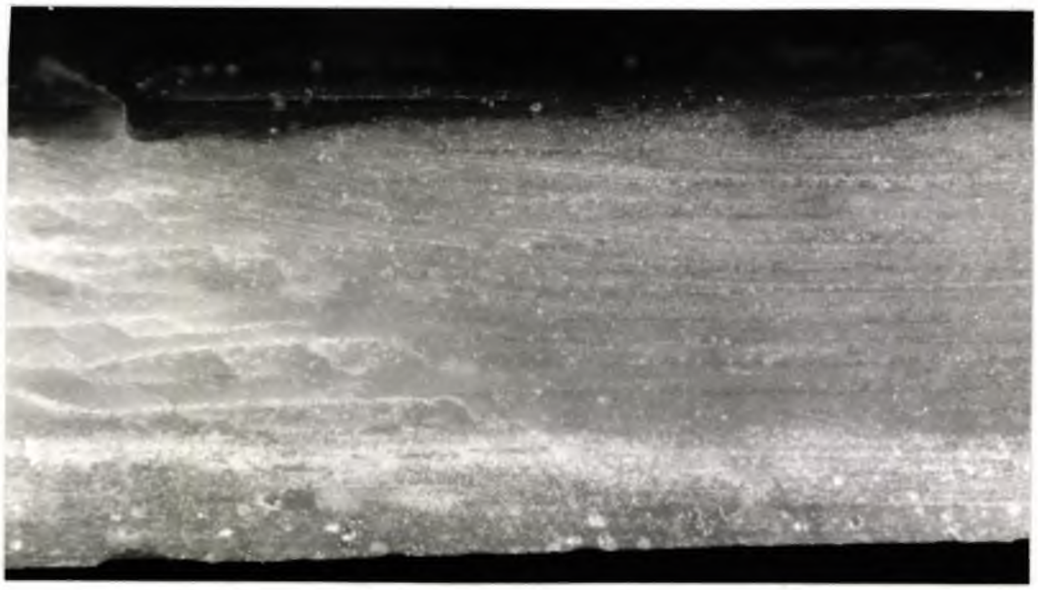

fig. 6.13b). It can be seen that the damage under the indentor spread out in an almost perfect 45° pattern, which has been previously observed (10), (21), (25) (see chapter 2). Transverse cracks were also seen in the lower resin layer. Similar damage was observed for the light and dark resin specimens.

Progressing away from first failure, the pipe tested up to 15kN revealed a major delamination (see fig. 6.14, which was a light resin specimen) around the middle layer. Delaminations could also be seen initiating in the layers immediately above and below the resin layers.

By the time the test end had been reached, very severe damage was observed. In the light resin case (see fig. 6.15), this extended to three major delaminations in layers 1, 4 and 10 counting from the inner resin surface. In the medium resin case, two major delaminations were seen at layers 4 and 8 from the inner resin surface. This highlights the observations that the medium resin pipes were less severely damaged than their light resin counterparts. [N.B. In both full damage cases, the sections photographed were those directly under the loading nose. Although attempts were made to observe the damage a little way from this (2/3cm), these sections fell apart when sectioned i.e. were very badly delaminated].

Similar investigations on single bounce impact tests revealed the same damage pattern at first failure as in the equivalent static tests i.e. a myriad of shear cracks was seen with a 45° damage pattern. Progressing to

Fig. 6.14 Photograph of pipe section (x9) to show the position of the delamination after loading to 15kN.

Fig. 6.15 Photograph of pipe section (x9) to show the position of the delaminations at full specimen damage.

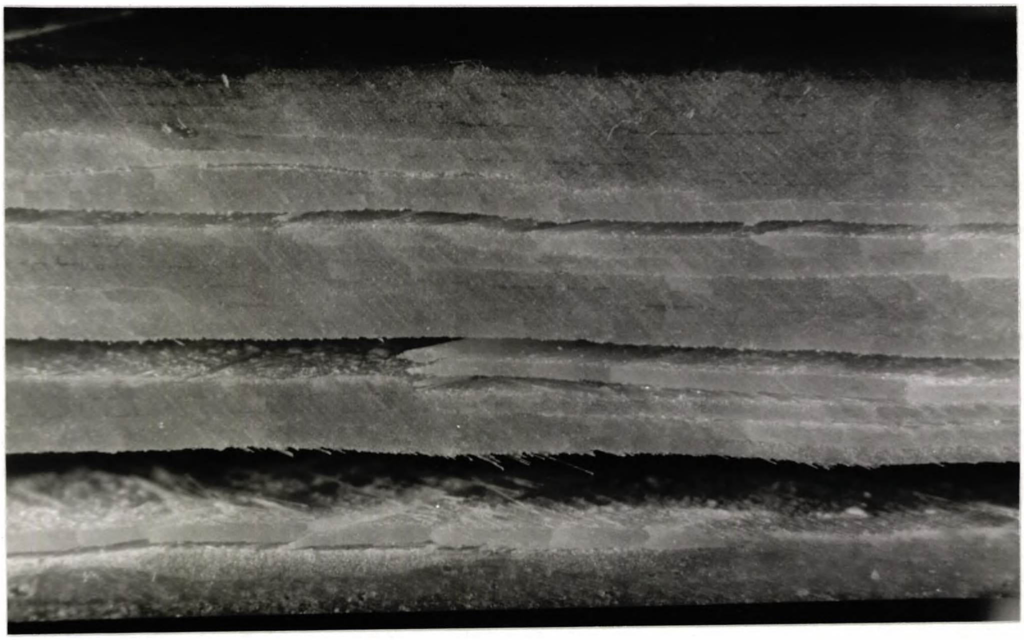

the test performed at an equivalent energy to a static test to 20kN revealed that again a major delamination had occurred in the middle pipe layer, but this extended much further away from the crush mark both axially and transversely. There appeared to be no damage in the other resin layers save that under the indentor. By full specimen damage, however, delamination was seen to extend to nearly all layers in sharp contrast to the static tests where delamination was observed at most between 3 layers.

Turning back to the partial damage tests performed and documented above, before residual property tests were carried out, numerical information (i.e. peak load, deflection to peak load, gradient and energy both at peak load and to test end) was extracted from the test curves. This is listed for each test type in tables 6.6a (static tests), 6.7 (single bounce impact tests) and 6.8 (multiple bounce impact tests) and the following comments should be made. Firstly, the lack of information for S3 is due to the laser-doppler velocimeter missing a part of the velocity/time history, making analysis impossible. Secondly, it was expected that properties for the single bounce and the first bounce of the multiple bounce impact tests would be similar. Reading tables 6.7 and 6.8 shows this is not the case. It would appear that the single bounce tests were carried out on weaker pipes with both stiffness and strength (characterised by gradient and peak load respectively) being lower. This is a variation in what appeared to be identical pipes as far as wall

Table 6.6a Static test data.

Specimen No.	Peak load (kN)	Deflection (mm)	Gradient (N/mm)	Energy to (J)	
				Peak load	Test end
P1	7.28	6.50	1.45x10^3	-	20.84
P3	15.00	20.25	0.69x10^3	-	167.65
P5	20.00	25.00	0.72x10^3	267.10	370.98
T10	32.50	54.25	0.79x10^3	1064.48	1246.73
T11	27.30	40.75	0.87x10^3	652.26	763.60
T12	31.90	55.25	1.08x10^3	1066.32	1121.46

Table 6.6b Static data for pipes of wall thickness 5mm.

Specimen No.	Peak load (kN)	Deflection (mm)	Gradient (N/mm)	Energy to (J)	
				Peak load	Test end
P2	4.78	6.50	0.90x10^3	-	13.78
P7	10.00	19.75	0.42x10^3	-	110.79
P4	14.30	30.25	0.46x10^3	237.94	261.59
P6	14.40	30.38	0.50x10^3	241.47	272.37

Table 6.7 Single bounce impact data

Specimen No.	Peak load (kN)	Deflection (mm)	Gradient (N/mm)	Energy to (J)	
				Peak load	Test end
S1	9.75	4.46	2.20x10^3	22.28	22.37
S3	-	-	-	-	169.77
S5	21.49	32.59	0.66x10^3	355.71	365.32
S11	21.17	49.36	0.45x10^3	665.71	749.29
S10	26.37	36.05	0.72x10^3	1152.50	1230.17

Table 6.8 Multiple bounce impact data

Specimen No.	Peak load (kN)	Deflection (mm)	Gradient (N/mm)	Energy to (J)	
				Peak load	Test end
IP1	30.47	5.44	2.80x10^3	17.64	22.75
IP3	26.00	17.78	1.47x10^3	149.15	166.84
IP5	48.24	26.07	1.87x10^3	374.72	375.60
IT11	34.94	52.74	0.66x10^3	744.76	762.16
IT10	38.65	71.11	0.58x10^3	1170.73	1251.31

thickness (6mm) and resin colour (medium) were concerned and possible reasons for this will be examined in chapter 8.

For comparison purposes and in order to highlight the differences to properties that small changes (in this case a 1mm reduction in wall thickness) in the pipe construction can have, the results are also listed in table 6.6b for static tests performed on pipes of wall thickness 5mm.

6.3-1b Residual property tests.

After the initial tests, the pipes were taken back to the Instron and retested to failure using the same geometry and loading conditions as in the original tests. The damage caused and the effect of varying the amounts of initial damage on the specimens was examined. The results of this investigation for the static and single bounce impact tests are considered below: the multiple bounce impact retests will be discussed later.

Firstly, the specimens were examined both visually and using the backlighting technique. All specimens, whether statically tested or impacted originally, showed damage to the inner surface of the pipe in contact with the Instron . This was in the form of inner surface gel coat cracks. As far as the delamination patterns were concerned, it was interesting to note that for initial loadings up to 20kN, retesting resulted in new delaminations. After this, the pattern remained the same with existing delaminations just growing.

The numerical information obtained from the residual property tests is presented in table 6.9 for the specimens originally statically tested and table 6.10 for those originally impacted using the single bounce mechanism. Both the total and projected delamination areas for each specimen are also included in these tables. Fig. 6.16a and b show graphs revealing the relationship between the two damage parameters i.e. total and projected delamination areas (A and A' respectively) against the incident energy, E_i, which is the energy applied to each specimen in the original test. Data points from the multiple bounce impact tests are also included in these plots. The easiest way of studying the relationship between the residual properties measured and the varying amounts of damage applied is to plot the properties against the two damage parameters. Figures 6.17, 6.18 and 6.19 show the result of plotting residual peak load (P_r), gradient (S_r) and deflection (d_r) to peak load respectively against both incident energy and total delamination area. The significance of these plots will be discussed later.

Before moving on to consider the cradled test results, the residual property tests conducted on the multiple bounce floor supported specimens should be mentioned. There was a difficulty associated with these, namely finding a well-defined second failure point since one did not exist in the majority of cases. Where no second failure existed, the test was stopped just before the impact nose would have entered the pipe specimen, causing it to collapse. Thus, the only residual property

Table 6.9 Residual properties for static floor supported tests

Specimen No.	Peak load ((kN)	Deflection (mm)	Gradient (N/mm)	Damaged area (m²)	
				Projected	Total
P1	17.85	30.50	$0.67x10^3$	0.0071	0.0071
P3	18.05	30.25	$0.55x10^3$	0.0198	0.0311
P5	19.50	33.50	$0.36x10^3$	0.0671	0.1108
T10	17.80	58.38	$0.24x10^3$	0.1657	0.2223
T11	18.50	51.50	$0.30x10^3$	0.1092	0.1491
T12	18.60	54.00	$0.23x10^3$	0.1623	0.2145

Table 6.10 Residual properties for the single bounce impact tests.

Specimen No.	Peak load (kN)	Deflection (mm)	Gradient (N/mm)	Damaged area (m²)	
				Projected	Total
S1	12.90	26.50	$0.55x10^3$	0.0026	0.0026
S3	13.05	37.50	$0.47x10^3$	0.0349	0.0778
S5	15.05	64.50	$0.25x10^3$	0.0969	0.1663
S11	14.80	65.00	$0.17x10^3$	0.1509	0.2590
S10	12.25	72.25	$0.13x10^3$	0.2213	0.3678

Table 6.11 Residual properties for the multiple bounce impact tests

Specimen No.	Gradient (N/mm)	Delaminated Area (m²)	
		Projected	Total
IP1	$0.48x10^3$	0.0027	0.0027
IP3	$0.24x10^3$	0.0586	0.0970
IP5	$0.29x10^3$	0.0594	0.1217
IT11	$0.19x10^3$	0.1533	0.3200
IT10	$0.15x10^3$	0.1791	0.3157

Fig. 6.16a Total delaminated area against incident energy for the floor supported geometry.

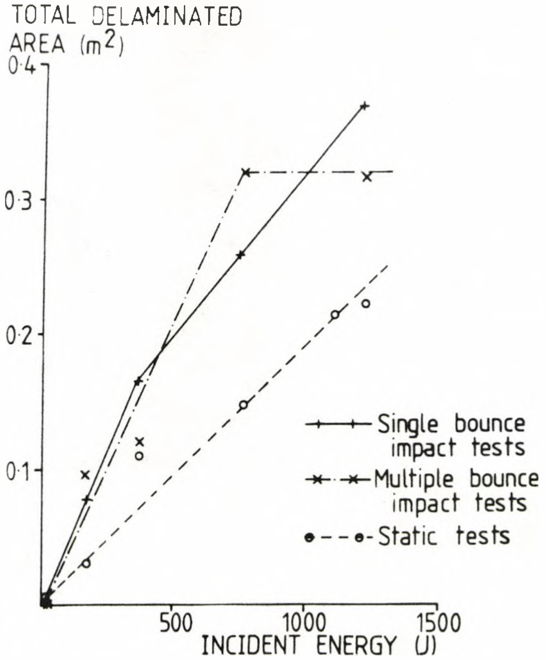

Fig. 6.16b Projected delaminated area against incident energy for the floor supported geometry.

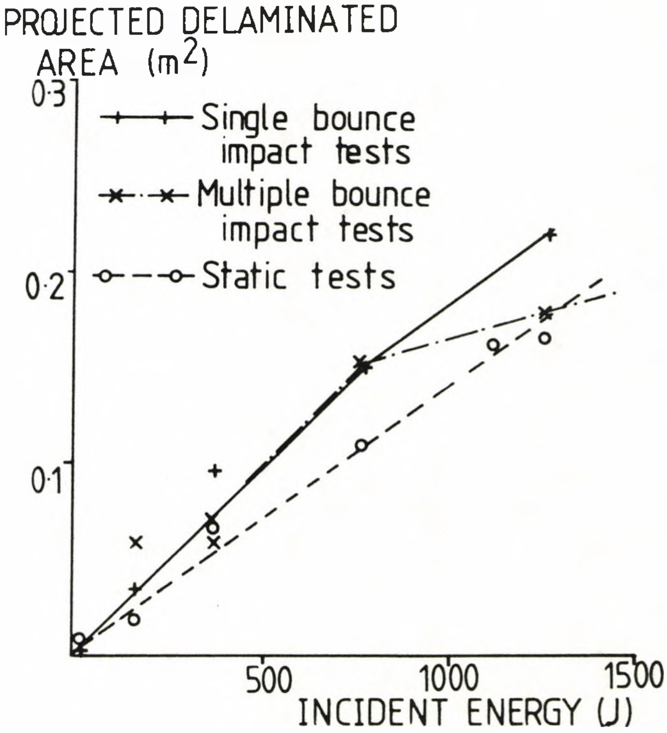

Fig. 6.17a Residual peak load against incident energy for the floor supported geometry.

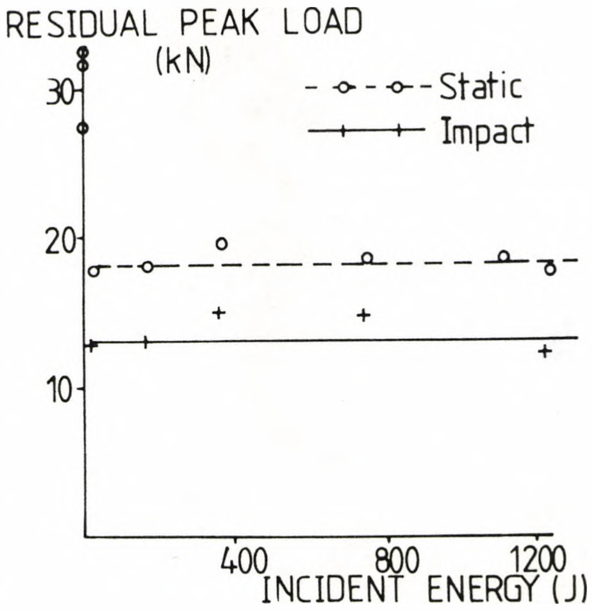

Fig. 6.17b Residual peak load against delaminated area for the floor supported geometry.

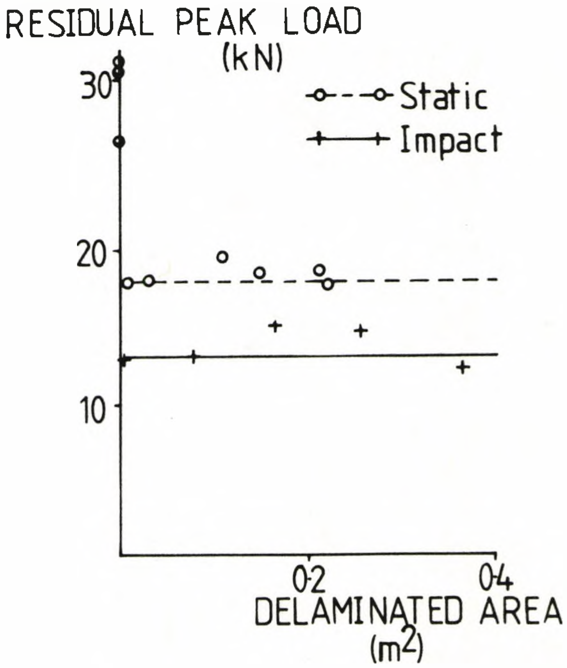

Fig. 6.18a Residual gradient against incident energy for the floor supported case.

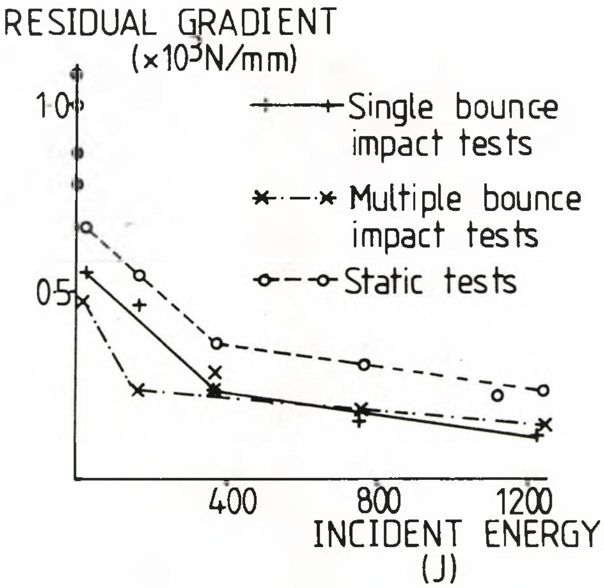

Fig. 6.18b Residual gradient against delaminated area for the floor supported geometry.

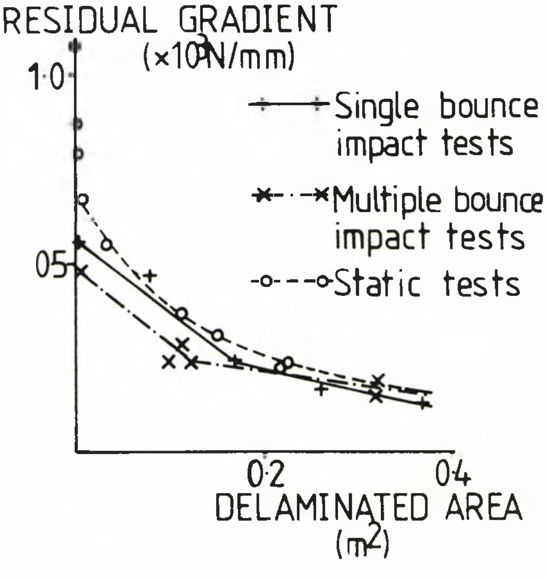

Fig. 6.19a Residual deflection at peak load against incident energy for the floor supported geometry.

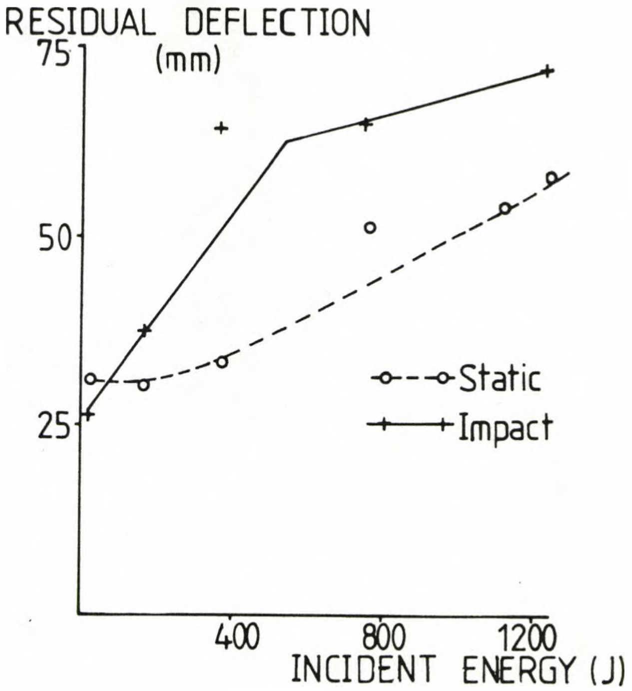

Fig. 6.19b Residual deflection at peak load against delamination area for the floor supported geometry.

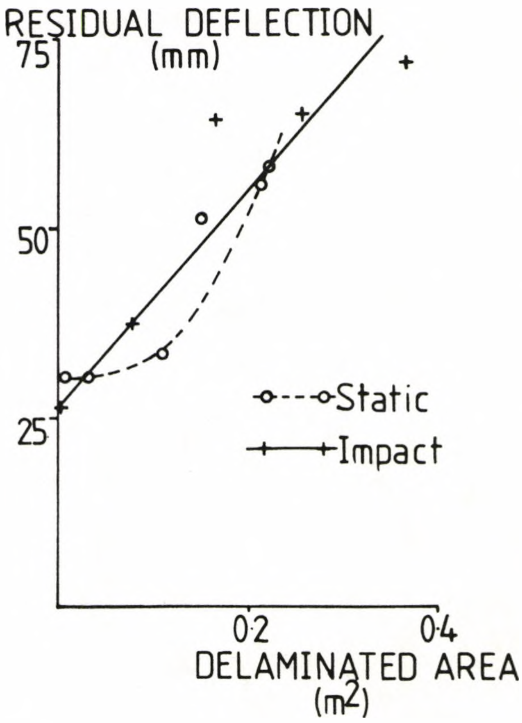

which could be measured in these tests was the gradient and details of this with the total and projected delamination areas are contained in table 6.11, with the data being plotted in fig. 6.18.

6.3-2a Initial cradled tests.

Fig. 6.20 shows the load/displacement curve for C4 i.e. to full specimen damage. The first thing to note is that despite the change of geometry, the failure process follows the same two part pattern as in the floor supported cases, although it does occur at a lower load (18.70 - 20.75kN as opposed to 27.30 - 32.50kN). There are two interesting features to note. The first is that for both geometries, the first failure point occurs at around the same peak load (between 6.4 and 8.6 kN). The second is that under test the close-fitting cradles do not appear to allow significant flexure at the pipe edges. This means the pipe retains its circular shape at the ends, unlike in the floor-supported geometry where for both pipe inner diameter sizes, significant squashing of the pipe ends was seen, resulting in an elliptical shape. Once again, almost all the damage is recoverable. Superimposed on the static curve is the dynamic force/displacement curve for L4, which was a single bounce specimen tested to equivalent energy as C4. This agrees very well with its equivalent static case, showing an overall increase in force (F) with displacement (d) and including a large vibratory effect (further analysed in chapter 7). Again, almost all damage is recoverable.

Fig. 6.20 Comparison of static and impact load/deflection curves for C4 and L4.

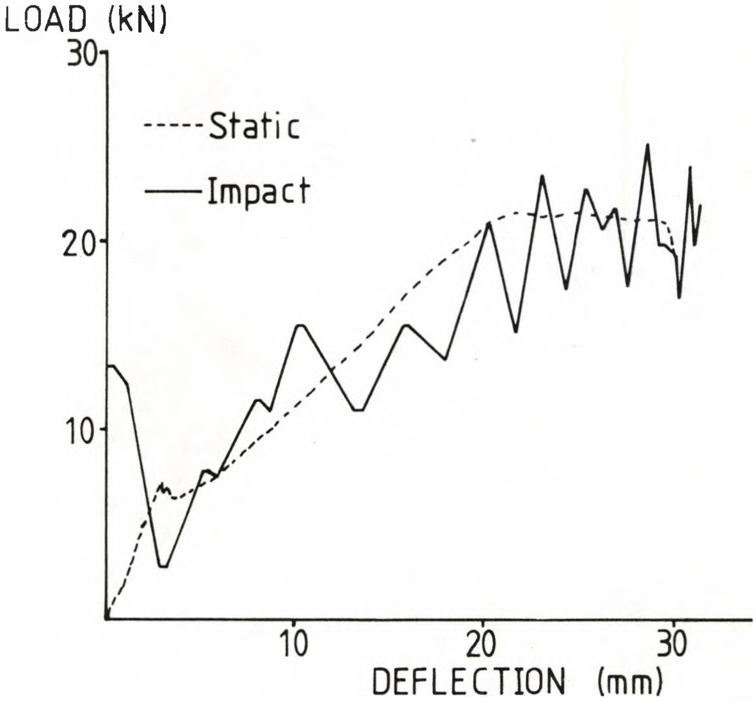

Fig. 6.21 Photograph of pipe delamination obtained by the backlighting technique for C3 (static).

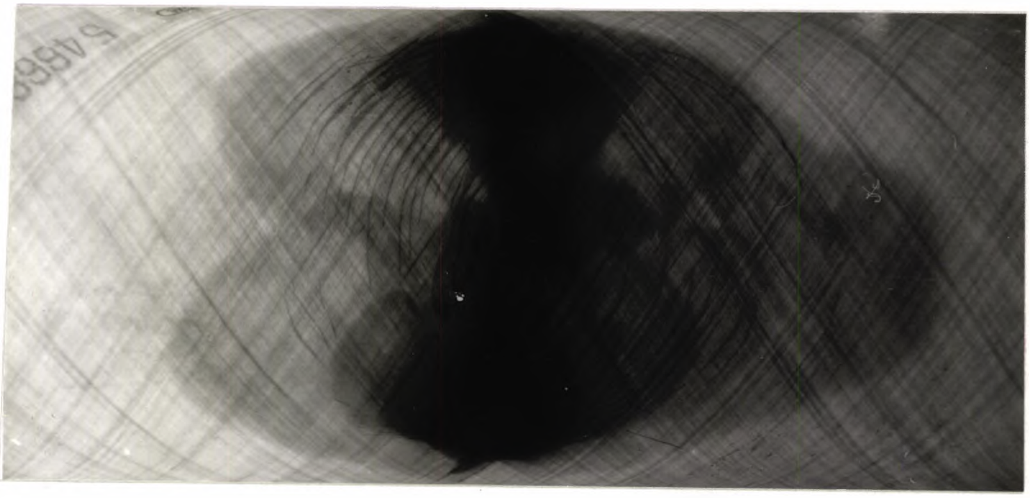

On inspection, both visually and by the backlighting technique, the damage sustained in the tests was similar to that seen in the floor supported tests, only less severe. An example of the delamination pattern at full damage (C3) is shown in fig. 6.21. After tests to complete specimen damage had been fully analysed, partial damage tests were carried out (see fig. 6.2 and table 6.2), revealing that damage built up as in the floor supported case (see fig. 6.7ii), but, as in the tests to full specimen damage, was less severe. These observations hold true for both static and impact cradled tests.

The build up of damage was further studied for static and single bounce cradle supported tests by sectioning selected pipes and observing the damage at x9. Again, as in the floor supported tests, the crazing type pattern was seen at first failure for both static and impact tests. The cracks also spread out at an angle of 45°. Looking firstly at the static tests, by the time full damage had been reached, delaminations were observed throughout the pipe layers and again the two different resin colours tested produced slightly different results. For the medium resin case, one major delamination was observed at around the central layer. For the light resin case, this delamination does exist, but it was much smaller than that found in the medium resin pipes. In both cases, damage was less severe than in the floor supported case. Turning now to the single bounce impact tests, by full specimen damage two major delaminations could be observed in layers 4 and 10 as opposed to one major delamination in the static tests. As observed above, this is much less severe than in the equivalent floor supported cases, where delaminations were found to extend to between virtually all layers.

Returning to the partial tests performed and documented above, before residual properties were measured, numerical information (i.e. peak load, gradient, deflection to peak load and energy both at peak load and to test end) was extracted from the test curves. This is listed in table 6.12 for the static tests and table 6.13 for the single bounce impact tests. These were observed to assess the differences between static and dynamic testing and were compared with the numerical information from the floor supported tests to investigate the effects of changing the test geometry. [N.B. It is worth noting at this stage why C6 and C7 have much greater stiffness than the other specimens. This is simply because of how the gradient was measured, illustrated as a in fig. 6.2 i.e. in these cases the gradient is measured before first failure occurred. For the remaining specimens (see b on fig. 6.2), the gradient was measured between first and second failure].

6.2-3b Residual property tests for the cradled specimens.

The pipes were then taken back to the Instron and retested to failure using the same geometry and loading conditions as in the original tests. The damage caused and the effect of varying the amounts of initial damage on the specimens were examined. The results of this

Table 6.12 Static test data for the cradled specimens.

Specimen No.	Peak load (kN)	Deflection (mm)	Gradient (N/mm)	Energy to Peak load	(J) Test end
C6	4.00	2.00	2.40×10^3	-	3.36
C7	8.00	3.13	3.08×10^3	-	11.12
C8	12.00	9.88	1.04×10^3	-	67.34
C9	16.00	15.75	0.90×10^3	-	142.74
C10	21.75	26.50	1.03×10^3	-	354.19
C3	21.25	30.50	0.91×10^3	427.93	610.66
C4	21.50	24.75	0.95×10^3	338.33	443.97
C5	22.75	34.25	0.98×10^3	549.05	712.55

Table 6.13 Single bounce impact data for the cradled specimens

Specimen No.	Peak load (kN)	Deflection (mm)	Gradient (N/mm)	Energy to Peak load	(J) Test end
L7	10.99	3.07	3.58×10^3	19.07	22.37
L8	14.03	9.14	1.52×10^3	67.33	68.96
L9	16.80	14.98	1.13×10^3	135.11	141.66
L10	30.68	23.65	1.29×10^3	340.43	346.69
L3	30.86	28.20	1.08×10^3	600.48	603.90
L4	25.29	28.59	0.89×10^3	407.05	438.02
L5	24.89	34.14	0.80×10^3	699.21	702.69

investigation for the static and single bounce impact tests are considered below.

Firstly, the specimens were examined both visually and using the backlighting technique. The first thing to note is that the surface in contact with the cradles under both static and impact conditions was not damaged at all (compared with the floor supported pipes which had inner surface gel coat cracks upon retest). As far as delamination patterns were concerned, all the partial tests upon retest produced new delaminations. For the full damage specimens, the pattern remained the same with existing delaminations just growing.

The numerical information obtained from the residual property tests is presented in table 6.14 for specimens originally statically tested and table 6.15 for those originally impacted. Both total and projected delamination areas for each specimen are also included in these tables and fig. 6.22 a and b show graphs revealing the relationships between both areas and the incident energy. The easiest way of studying the relationships between the residual properties measured and varying the amounts of damage induced is to plot the properties against the two damage parameters. Figs. 6.23, 6.24 and 6.25 show the results of plotting residual peak load, gradient and deflection to peak load, respectively, against both incident energy and total delamination area. The significance of these tests will be discussed later.

Table 6.14 Residual property data for the cradled static tests.

Specimen No.	Peak load (kN)	Deflection (mm)	Gradient (N/mm)	Damage area (m^2)	
				Projected	Total
C6	22.00	24.38	$0.98\text{x}10^3$	-	-
C7	22.25	36.50	$1.07\text{x}10^3$	0.0038	0.0038
C8	23.25	37.00	$1.06\text{x}10^3$	0.0184	0.0184
C9	23.00	37.00	$0.66\text{x}10^3$	0.0363	0.0453
C10	22.25	40.00	$0.56\text{x}10^3$	0.0715	0.1470
C3	19.75	41.25	$0.27\text{x}10^3$	0.1206	0.2009
C4	22.75	41.00	$0.32\text{x}10^3$	0.0847	0.1470
C5	20.75	50.50	$0.26\text{x}10^3$	0.1211	0.2300

Table 6.15 Residual properties for the cradled single bounce impact tests.

Specimen No.	Peak load (kN)	Deflection (mm)	Gradient (N/mm)	Damage area (m^2)	
				Projected	Total
L7	23.25	38.00	$1.82\text{x}10^3$	0.0044	0.0044
L8	20.50	27.13	$1.12\text{x}10^3$	0.0116	0.0163
L9	22.90	39.50	$0.55\text{x}10^3$	0.0236	0.0356
L10	22.60	39.75	$0.43\text{x}10^3$	0.0746	0.1177
L3	21.00	42.00	$0.33\text{x}10^3$	0.1302	0.2191
L4	19.80	38.75	$0.30\text{x}10^3$	0.0879	0.2120
L5	17.50	53.13	$0.25\text{x}10^3$	0.1876	0.3088

Fig. 6.22a Graph of total delaminated area against incident energy for the cradled specimens.

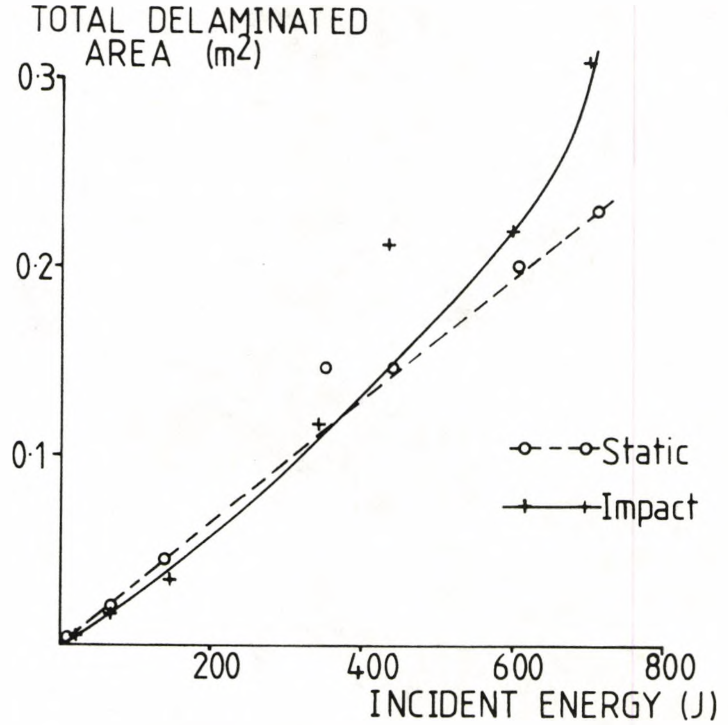

Fig. 6.22b Graph of projected delaminated area against incident energy for the cradled specimens.

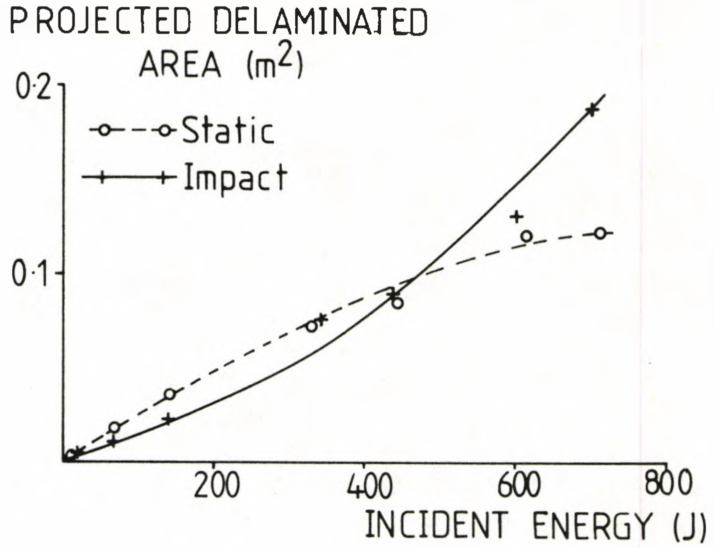

Fig. 6.23a Graph of residual peak load against incident energy for the cradled geometry.

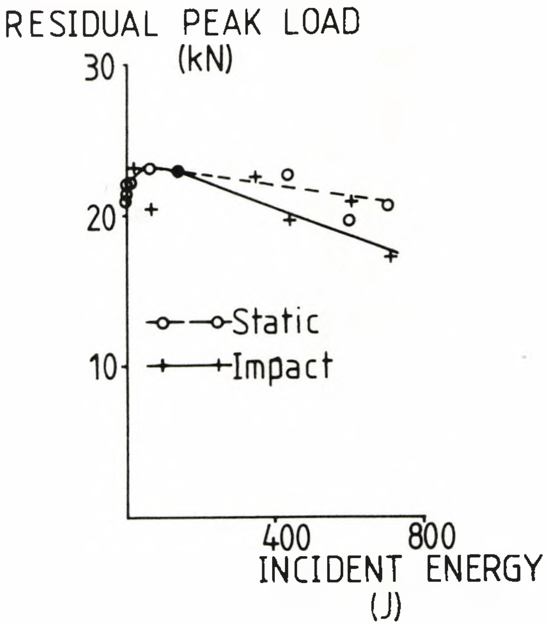

Fig. 6.23b Graph of residual peak load against delaminated area for the cradled geometry.

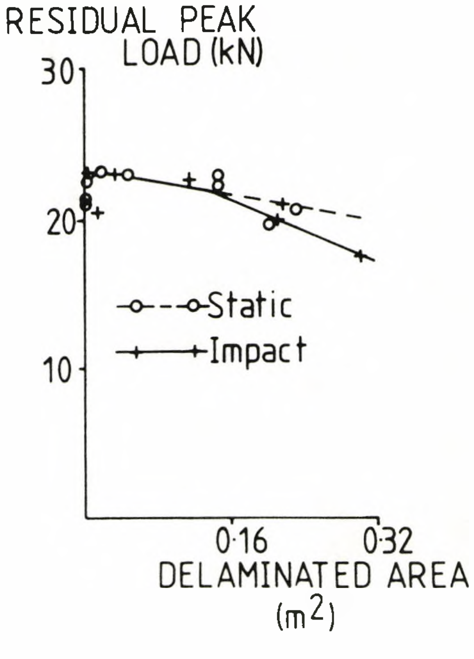

Fig. 6.24a Graph of residual gradient against incident energy for the cradled geometry.

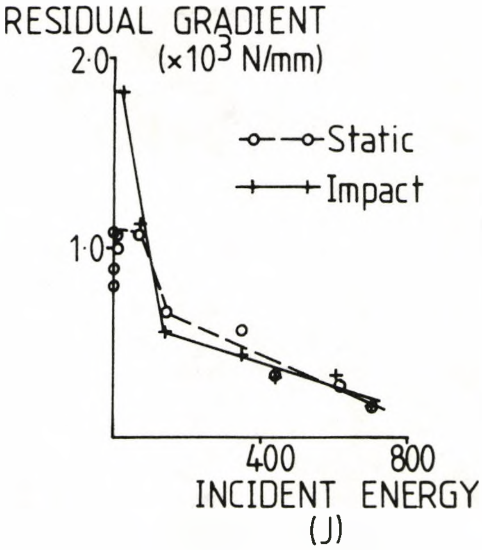

Fig. 6.24b Graph of residual gradient against delaminated area for the cradled geometry.

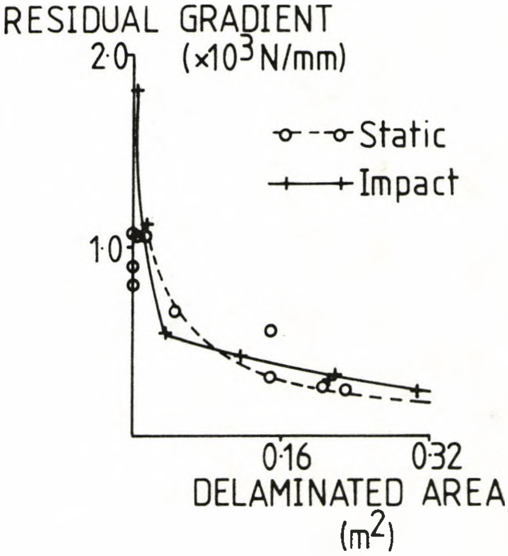

Fig. 6.25a Graph of residual deflection to peak load against incident energy for the cradled geometry.

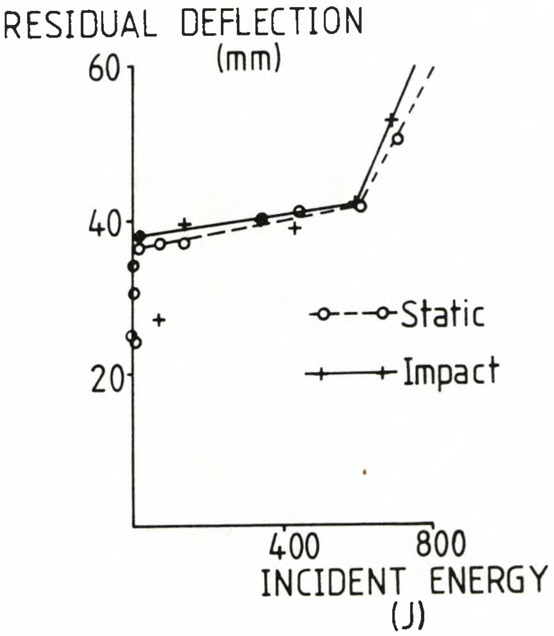

Fig. 6.25b Graph of residual deflection to peak load against delamianted area for the cradled geometry.

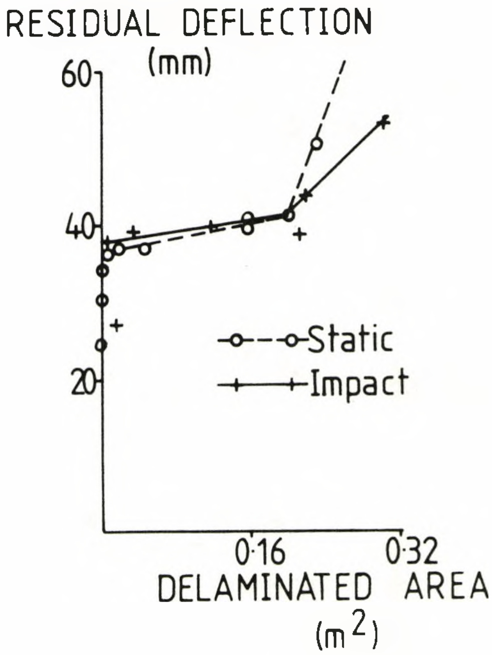

7.- MODELLING BY ANALYTICAL, FINITE ELEMENT AND DYNAMIC ANALYSIS METHODS.

This chapter deals with methods for predicting the displacement and stress distributions during elastic behaviour (i.e. up to first failure point) and predicting the load/time behaviour of the pipes during impact (89). The individual modelling techniques are detailed in the following sections, together with comparisons with experimental results, which will give an indication of the success or otherwise of the modelling technique under consideration.

7.1 Analytical method.

For an initial comparison with experimental work, a simple analytical model was considered (90) which allowed prediction of the deflection at first failure for the floor supported pipes. The model consisted of the system illustrated in fig. 7.1 where two equal and opposite point loads were applied at the pipe mid-point, allowing the deflection, d, to be calculated as shown below:-

$$d = 6.5\ P/Et\ (R/t)^{3/2}\ (L/R)^{-3/4} \quad (7.1)$$

where P is the experimental load to first failure, E the modulus of elasticity = 18GPa (91), t the wall thickness, R the inner pipe radius and L the pipe length. For the model to apply, R/t must be greater than 10 and L/R must lie between 1 and 18. Both constraints were satisfied for the large and small pipes so the equation was applied and the deflections predicted are listed in tables 7.3 and

Key to fig. 7.2.

Axis system (i)	local element axes.
Axis system (ii)	global Cartesian coordinate axes. (for preprocessor)
Axis system (iii)	global cylindrical coordinate axes. (for postprocessor).

Fig. 7.1 Analytical Pipe Model i.e System of pipe with two equal and opposite point loads applied.

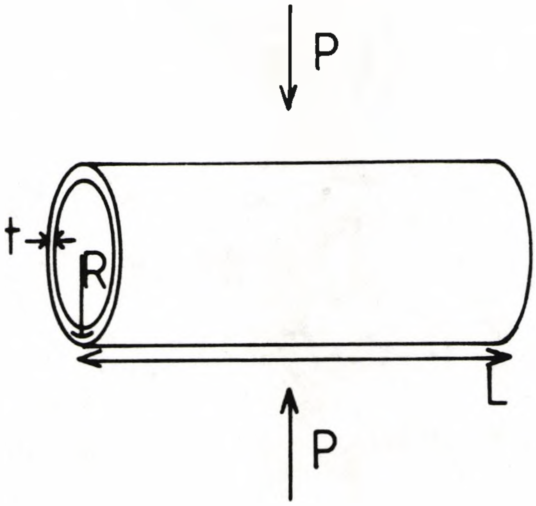

Fig. 7.2 Axis systems used in the finite element modelling.

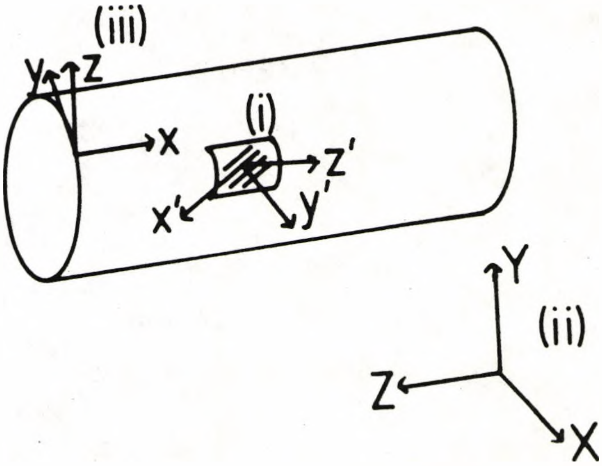

7.4 respectively, along with the experimental deflections to first failure and the deflections predicted by computer. This reveals that, despite being a very simple model, the analytical method shows good agreement with experiment.

7.2 Finite element methods.

Finite element analysis, using the NISA2 package (75), was used to predict both the stress fields and the displacements at first failure for all the full pipe sizes and support conditions considered. The elements used were 4-noded anisotropic laminated shell elements with the following local element axis system (see fig. 7.2):

x' - along the fibre direction

y' - in the plane transverse to the fibre direction

z' - in the plane normal to the fibre direction i.e. out of the plane.

and had 6 degrees of freedom per node.

The material properties used for the model (listed in table 7.1) are typical properties used as standards in modelling. Each of the three systems modelled will be considered separately.

7.2-1 Modelling the floor supported large pipe.

The large pipe model was constructed as being 1000mm long with an external diameter of 426mm and a wall thickness of 13mm. Isotropic gel coat layers 1.3mm thick were used, with the remaining 10.4mm thickness constructed as 8 composite layers, also 1.3mm thick, and

Table 7.1 Unidirectional Material Properties required for Modelling.

Material Property	Value for Composite layer	 Resin layer
Longitudinal Young's Modulus	3.86×10^{10}Pa	4×10^{9}Pa
Transverse Young's Modulus	8.27×10^{9}Pa	4×10^{9}Pa
Poisson's Ratio, v_{xy}	2.60×10^{-1}	3.30×10^{-1}
Shear Moduli (G_{xy}, G_{yz} and G_{xz})	4.14×10^{9}Pa	1.5×10^{9}Pa

Table 7.2 How the 20kN Load was Divided for Application to the Large Pipe Model.

Z position (mm)	X position (mm) 114	 79	 40	 0	 -40	 -79	 -114
0	39 500	41 1000	45 1500	1 2000	3 1500	5 1000	9 500
10	40 250	42 500	46 750	2 1000	4 750	6 500	10 250
20	136 125	138 250	142 375	98 500	100 375	102 250	104 125
-10	568 250	570 500	574 750	530 1000	532 750	534 500	538 250
-20	664 125	666 250	670 375	626 500	628 375	630 250	634 125

KEY : node numbers e.g. 39

load applied e.g. 500 (in Newtons).

Table 7.3 Comparison of Modelling with Experiments for the Floor Supported Large Pipes.

Method of Displacement Determination	Specimen	Displacment at 20kN (mm)
Experimental values	G3	9.75
	V2	10.00
	V3	8.50
Analytical solution		10.77
Computer solution		10.62

Table 7.4 Comparison of Modelling with Experiments for the Floor Supported Small Pipes.

Method of Displacement Determination	Specimen	Displacement at 6.75kN (mm)
Experimental values	P1	6.00
	P3	5.50
	T11	5.50
	T12	6.50
Analytical solution		4.73
Computer solution		4.87

Table 7.5 Comparison of Modelling with Experiments for the Cradled Small Pipes.

Method of Displacement Determination	Specimen	Displacement at 6.39kN (mm)
Experimental values	C1	3.88
	C2	3.50
	C3	3.75
Computer solution		3.68

oriented at ±55°. The support conditions of the pipe were modelled by restraining along its bottom line in X and Y and additionally the top centre node was restrained in X and Z to prevent rotation (where X, Y and Z are the global Cartesian coordinate axes required for the preprocessor - see fig. 7.2). The next step was to apply the load to first failure to the model, in this case 20kN. In order to recreate the experimental situation as closely as possible, this was initially applied as a line load in the X direction (i.e. transverse to the pipe axis). Then, to simulate the circular shape of the loading nose, the load was further subdivided parabolically in the Z direction. The loads actually applied to each node are shown in table 7.2. It should be noted that the X range is chosen to be ±114mm from experimental observations whereas the Z range of ±20mm simply represents the diameter of the loading nose.

The model was run successfully and examples of the output obtained can be seen in figs 7.3 and 7.4. It should be noted that a slight modification in the program allowed the results obtained for all three systems to be in a third axis system - see fig. 7.2 - which will be referred to as the global cylindrical coordinate system. This allowed stresses in the longitudinal (x) and hoop (y) directions of the pipe to be studied and thus was more meaningful than the preprocessor Cartesian axes system. Figure 7.3 represents the pipe deformation superimposed on the original pipe shape to show the squashing which occurs, and is viewed from the end of the

Fig. 7.3 FEA prediction of the deformation superimposed onto original pipe shape for large floor supported pipe.

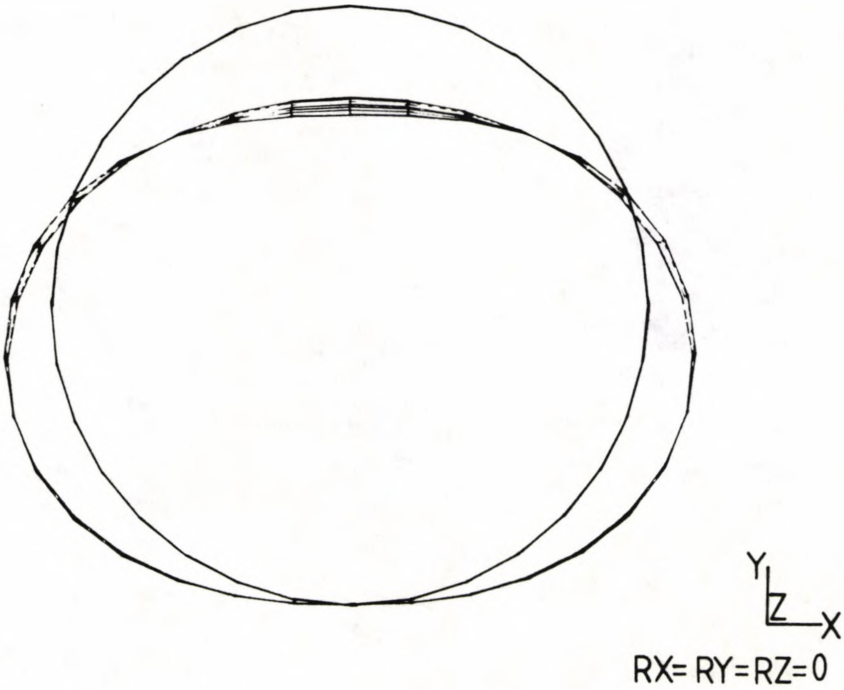

Fig. 7.4 FEA prediction of global shear stress for the large floor supported pipe.

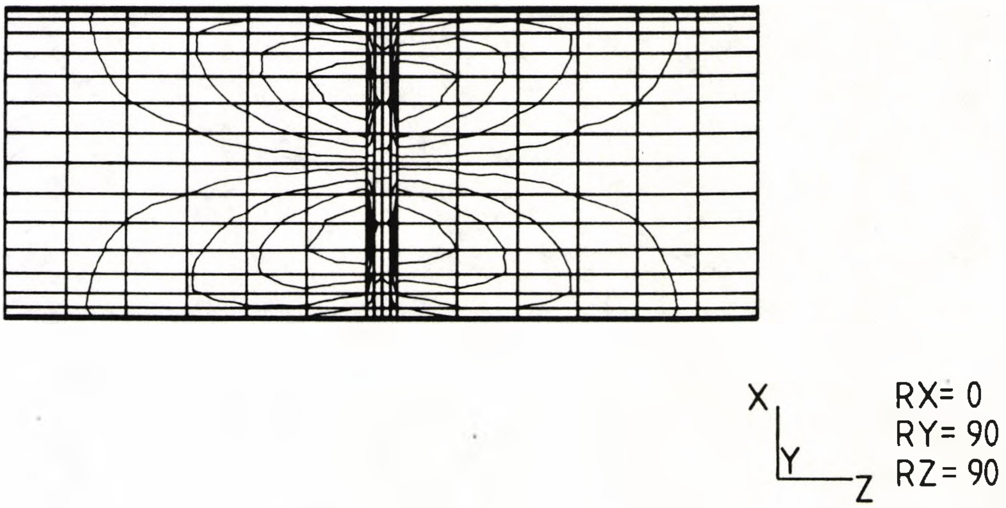

pipe (i.e. at a rotation of 0,0,0). The maximum deformation predicted is listed in table 7.3 along with, for comparison, the experimental values of displacement revealing a slightly lower prediction of 10.62mm than the analytical solution also quoted. Figure 7.4 represents the average shear stress through the layers, N_{xy}, at a rotation of (0,90,90) referred to (X,Y,Z) i.e. looking at the top of the pipe where the line load was applied.

7.2-2 Modelling the floor supported small diameter pipe.

The element mesh for the small pipes is shown in fig. 7.5. As in the large pipe, the central region where the load was to be applied was constructed with more elements for increased accuracy of prediction. The extra detail at the pipe ends was needed to simulate the cradled support condition (see section 7.2-3), since the same basic grid was used with only the restraints necessary to model the floor support and cradled support conditions being altered, along with the experimental value of the load to first failure, which differed slightly between the two systems.

The model pipe constructed was 500mm long with an external diameter of 162mm and a wall thickness of 6mm. Isotropic gel coat layers 1mm thick were used with the remaining 4mm thickness constructed as 8 composite layers 0.5mm thick and oriented at ±55°. The model was restrained in exactly the same way as the large diameter floor supported pipe, and the load to first failure, in this case 6.75kN, was also applied in the same manner. Experimental observation resulted in an X loading range for this model of ±55mm and the loading nose dimensions resulted in the Z loading range being ±12.5mm.

The model was run successfully and output similar to figs. 7.3 and 7.4 was obtained. The maximum deformation predicted is listed in table 7.4, again revealing increased accuracy of prediction when compared with the analytical solution calculated using equation 7.1. Also obtained from this run were plots of the individual layer stresses (S_{xy}) and examples of these are presented in figures 7.6, 7.7, 7.8, 7.9 and 7.10. All of the plots are for composite layers since in the two gel coat layers stresses were found to be very low. Figure 7.6 represents the first composite layer underneath the outer gel coat and angled at +55°.

Figures 7.7 and 7.8, which represent composite layers 5 and 6, are included because they demonstrate the antisymmetrical effects of two adjacent layers, one angled at -55° and the next at +55°. The remaining two figs. 7.9 and 7.10 concentrate on the inner composite layer (number 8) and show the stress contours generated in both the loading region and the surface in contact with the Instron base plate. [N.B. It can be seen that the N_{xy} and S_{xy} plots have different shapes and this is

Fig. 7.5 Element mesh for the small pipes.

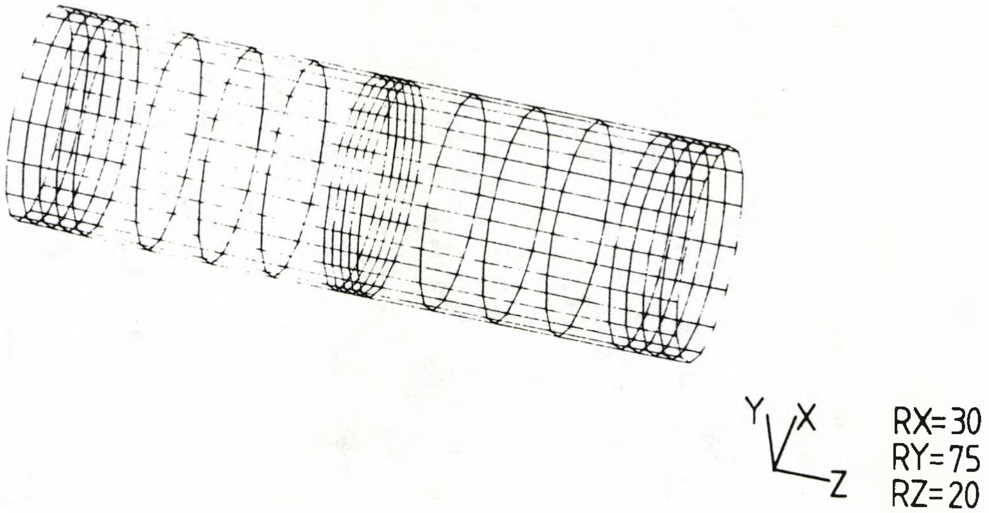

Fig. 7.6 FEA prediction of the shear stress in layer 3 of the small floor supported pipe.

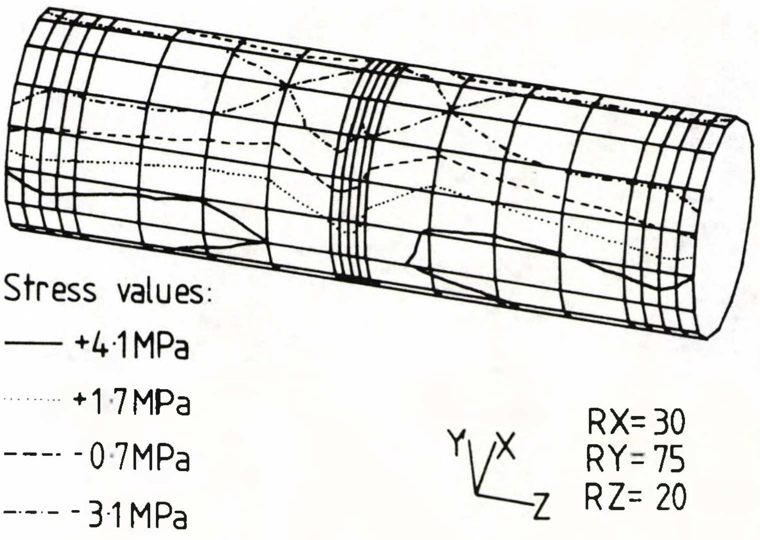

Fig. 7.7 FEA prediction of the shear stress in layer 5 of the small supported pipe.

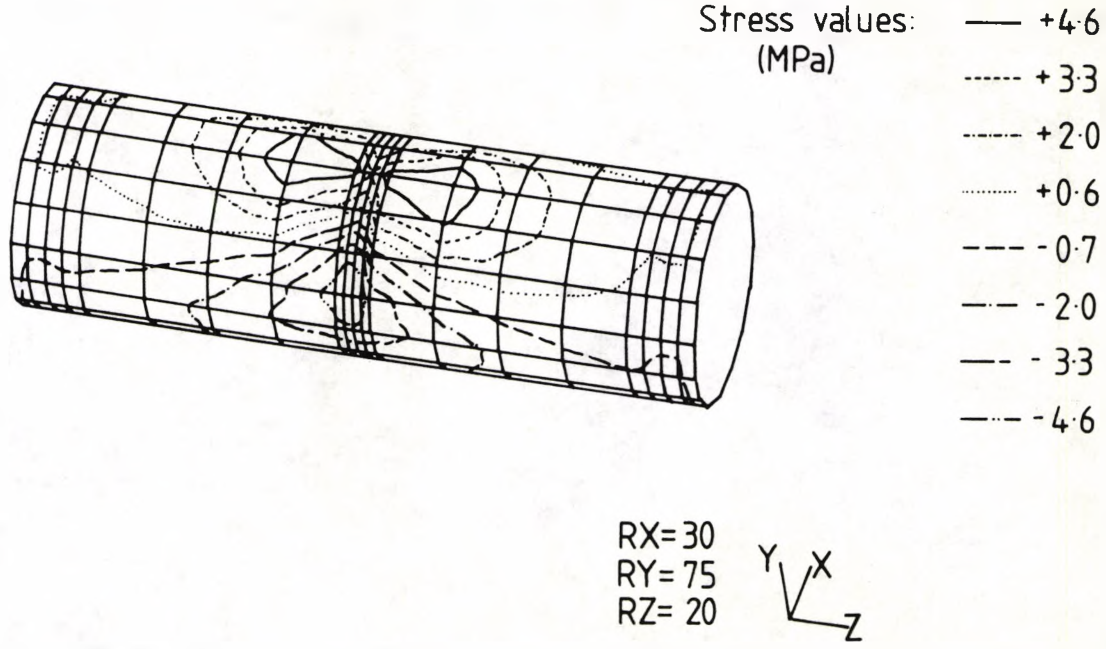

Fig. 7.8 FEA prediction of the shear stress in layer 6 of the small floor supported pipe.

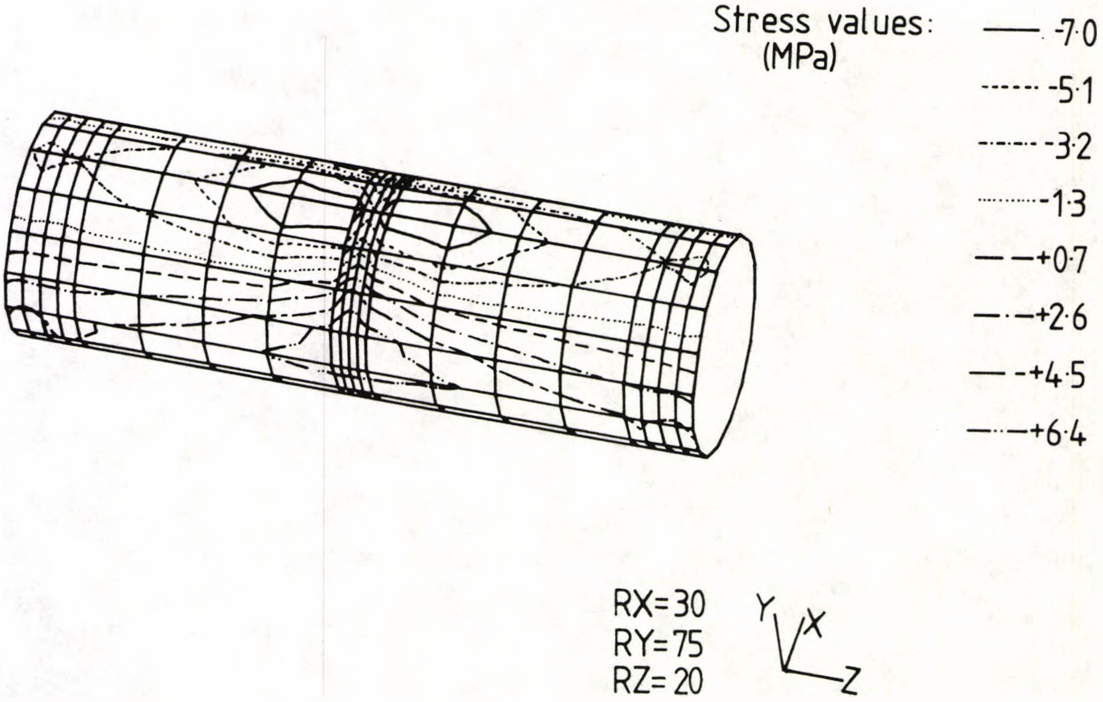

Fig 7.9 FEA prediction of the shear stress in layer 8 of the small floor supported pipe.

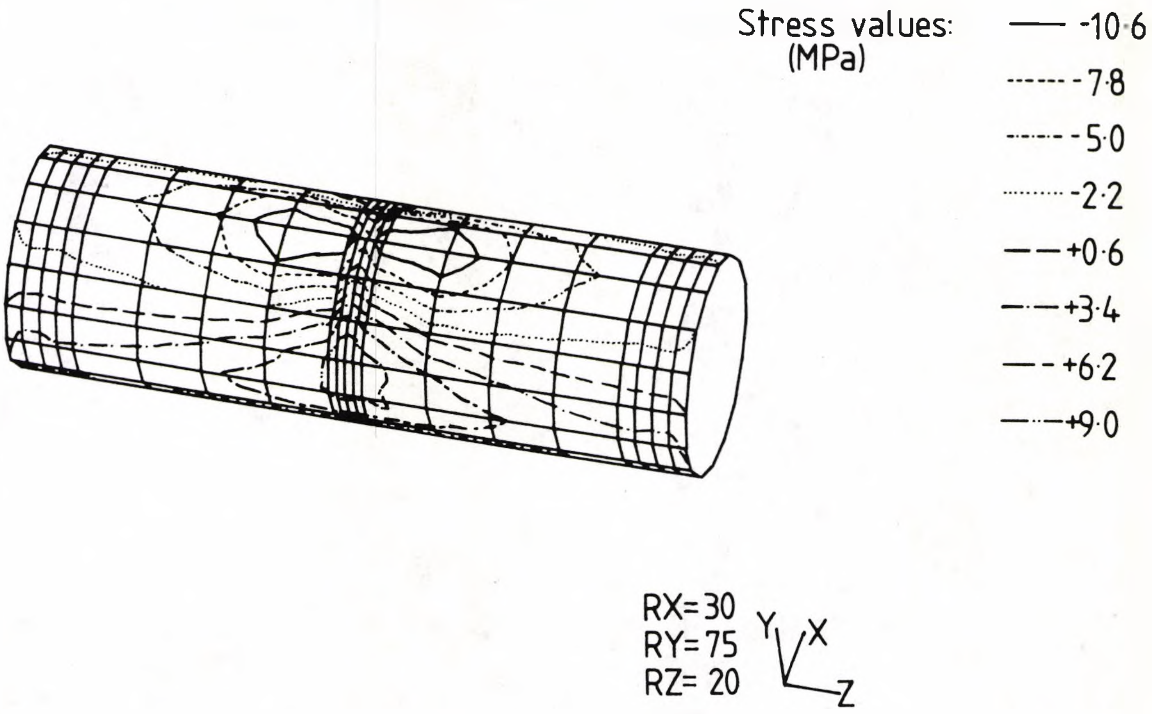

Fig. 7.10 FEA prediction of the shear stress in layer 8 of the small floor supported pipe rotated through 180° to reveal the surface in contact with the Instron base plate.

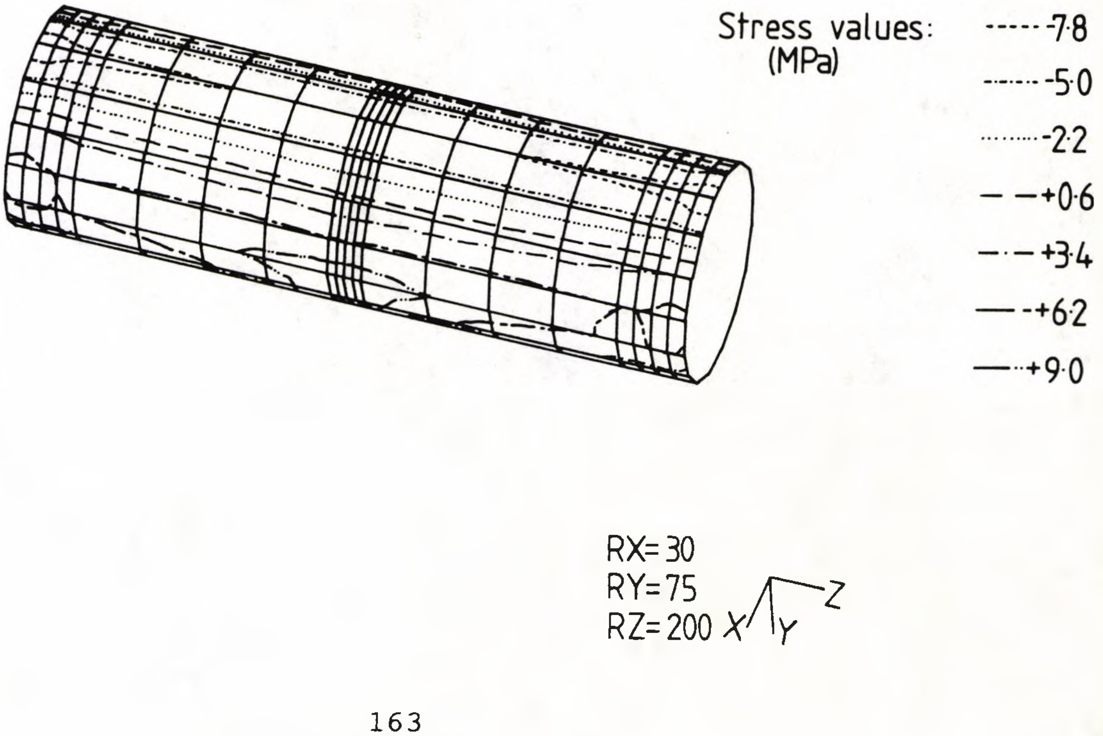

believed to be due to the antisymmetric nature of the stress patterns on the individual layers, which are added to produce the overall N_{xy} plots].

7.2-3 Modelling the cradled small pipe.

As has already been indicated, the same element mesh was used as in the small floor supported pipe with the following modifications. Firstly, all restraints were removed except the one on the top node, which was to prevent rotation. Initially, the cradles were simulated as in fig. 7.11 which involves restraining all the nodes within the following ranges: Z lies between 0 and 50mm, and between 450 and 500mm; Y lies between 0 and -78mm. There are two values of X for every value of Y, thus creating the correct cradle shape. [It should be noted that the Y and Z ranges were chosen simply from the actual cradle measurements of 50mm long and 80mm high]. All 90 nodes which lay in the required range were restrained in X and Y. Then, the experimental load to first failure, in this case 6.39kN, was applied in the same manner and over the same X and Z ranges as in the floor supported small pipe case.

The model was run but revealed a very low deformation of 1.25mm and interesting effects were observed in both the stress and deformation plots. Fig. 7.12 reveals the deformed shape viewed from the side (i.e. at a rotation of 0,90,0) and shows a predicted deformation upwards from the bottom surface. Much consideration provided the following explanation. When the load pushes the top surface downwards, the sides bow

Fig. 7.11 Element mesh for the small pipe with the initial restraints for the cradles indicated.

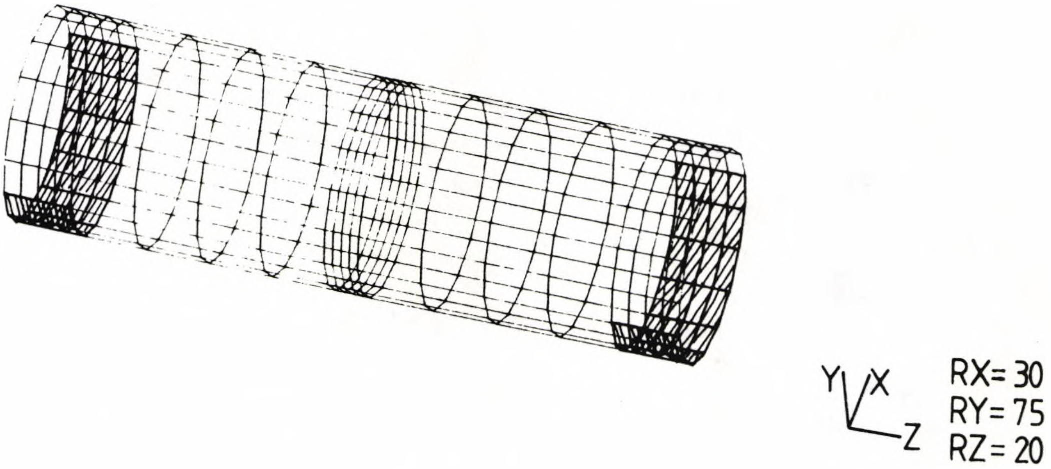

Fig. 7.12 FEA prediction of the deformation viewed from the side of the small pipe restrained as in fig. 7.11.

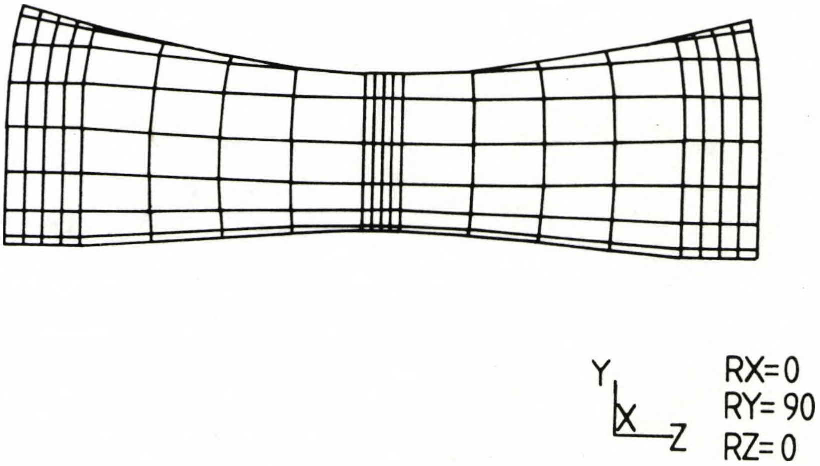

out easily but are extremely inflexible downwards. Thus, the bottom surface comes up because the centre of the pipe is effectively fixed i.e. is stationary. What is actually required is that the whole pipe be allowed to flex as in the experiments where it is not clamped into the cradles but just rests in them. Thus, the ends of the pipe can actually move downwards and sideways during the test, which they are prevented from doing in the original version of this model (see fig. 7.13 which schematically illustrates the difference between the original model and the real situation).

Using this information, it was then decided to restrain the nodes indicated in fig. 7.14 to allow the ends of the pipe to flex upwards. The restraints on the top node, in X and Z, were retained.

This model was then run successfully and output similar to figs. 7.3 (see fig 7.14a) and 7.4 was obtained. The maximum deformation predicted, 3.68mm, is listed in table 7.5 and shows very good agreement with the experimental values of deformation which lay between 3.5 and 3.88mm. [N.B. There is no analytical solution for this particular case]. Individual layer stress plots were again produced and examples of these are presented in figs 7.15, 7.16, 7.17 and 7.18. By referring to the equivalent figures for the floor supported pipe, it is possible to compare the two cases. Once again, the plots all represent composite layers since the stresses in the gel coat layers were found to be very low. Fig. 7.15 represents the first composite layer under the outer gel coat (i.e. it is

Fig. 7.14a FEA prediction of the deformation viewed from the side of the small pipe restrained as in fig. 7.14.

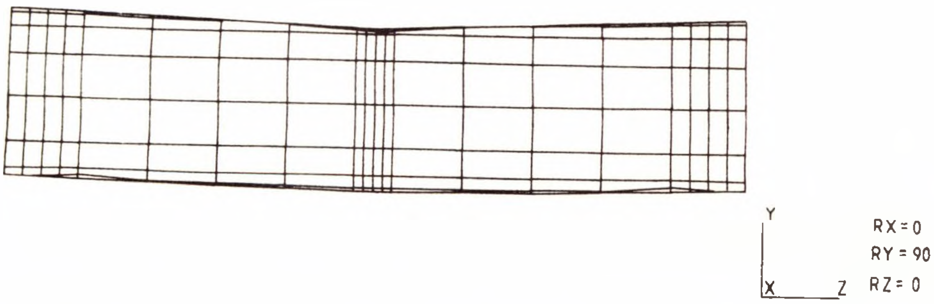

Fig. 7.13 Schematic comparing the initial model restraints with the real cradle support conditions.

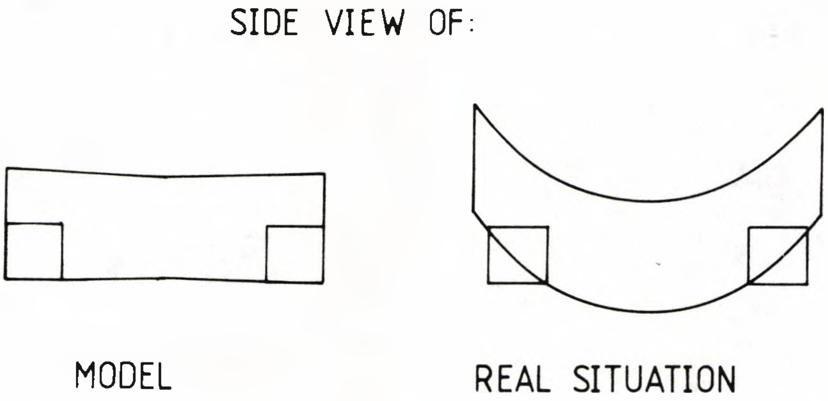

Fig. 7.14 Element mesh for the small pipe indicating the nodes restrained in the successful run to model the cradles.

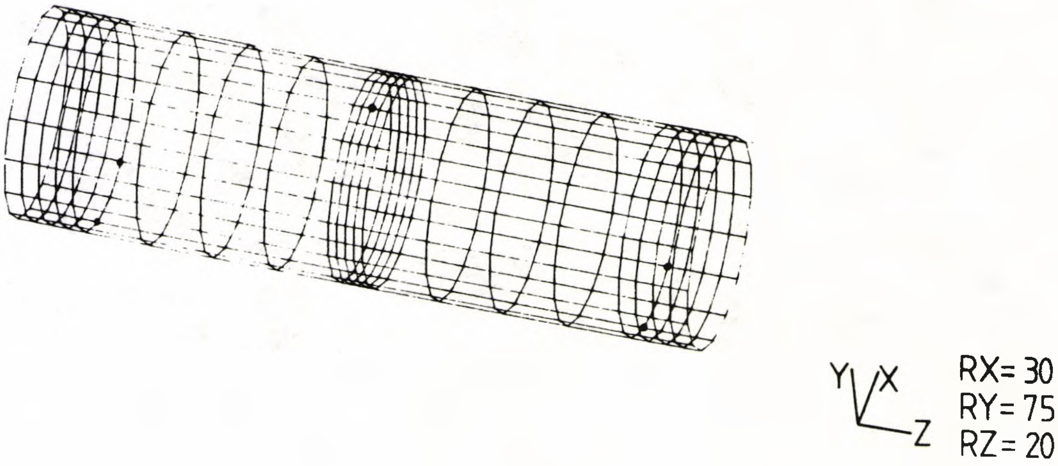

Fig. 7.15 FEA prediction of the shear stress in layer 3 of the small cradled pipe.

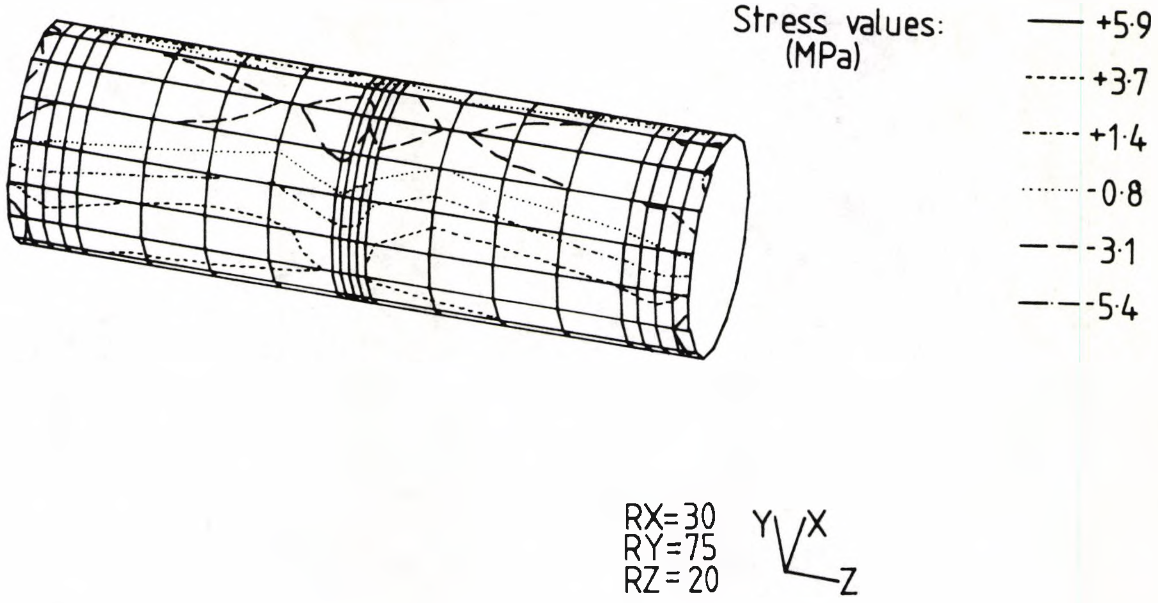

Fig 7.16 FEA prediction of the shear stress in layer 5 of the small cradled pipe.

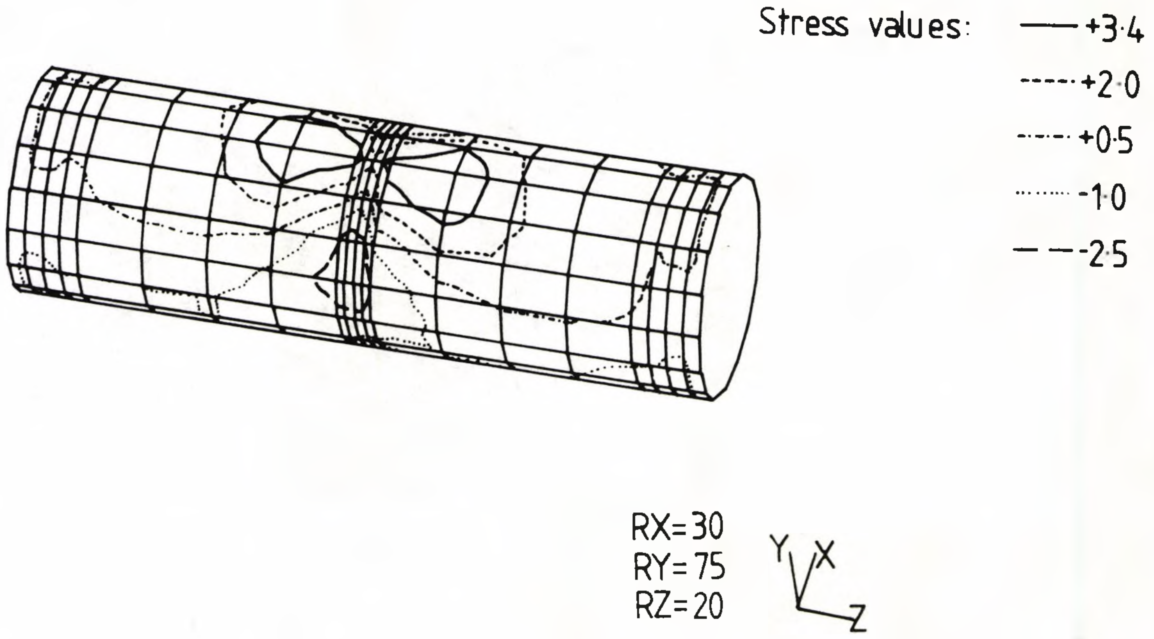

Fig 7.17 FEA prediction of the shear stress in layer 8 of the small cradled pipe.

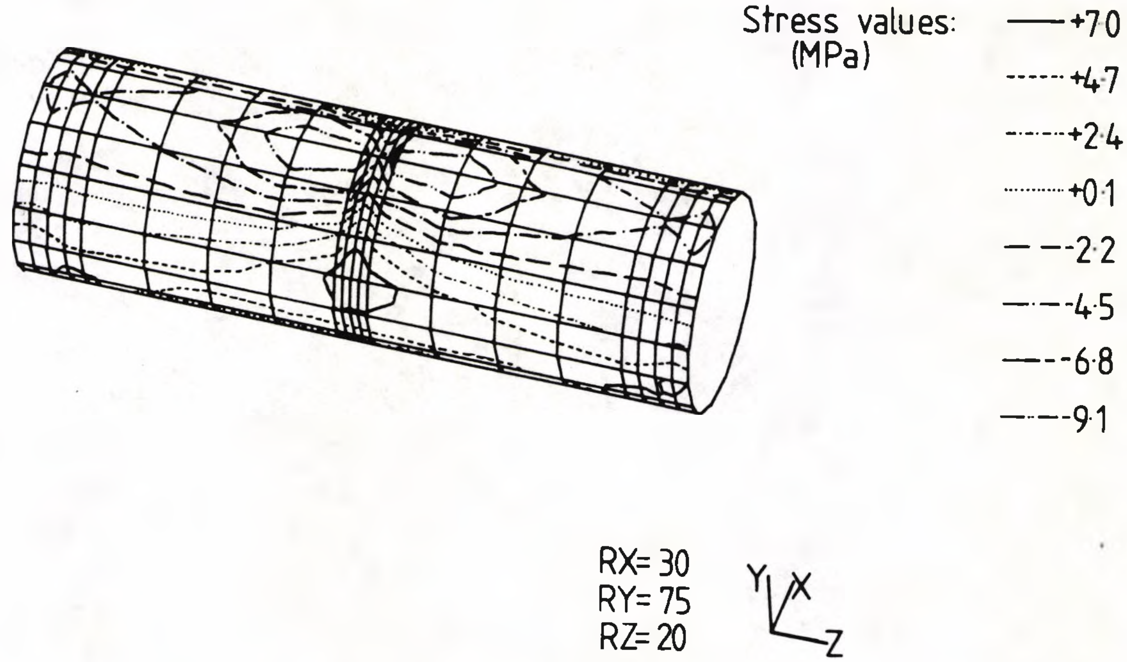

Fig. 7.18 FEA prediction of the shear stress in layer 8 of the small cradled pipe rotated through 180° to reveal the surface in contact with the cradles.

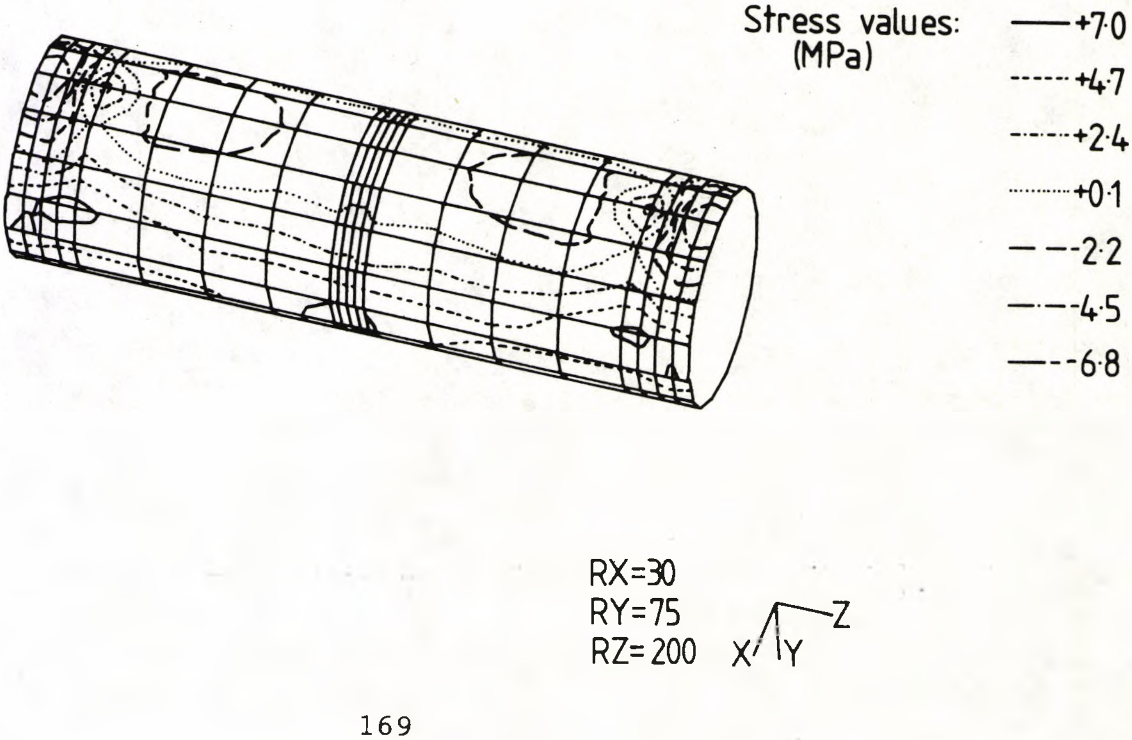

equivalent to fig. 7.6). It can be seen that the stresses generated are slightly lower than in the floor supported case.

Figs. 7.17 and 7.18 are included to compare the loading region and the region in contact with the cradles for the innermost composite layer, number 8. Fig. 7.18 shows very well the effects the cradles have on the stresses in the pipe and should be compared with fig. 7.10 showing the support side of the floor supported pipe i.e. that which is in contact with the Instron base plate.

In addition to predictions of the maximum deformation and overall and individual layer stress patterns, the variation of longitudinal stress (S_{xx}), hoop stress (S_{yy}) and inplane shear stress (S_{xy}) with thickness for the three systems modelled was also considered at selected nodes and elements.

Considering firstly the S_{xx} and S_{yy} variations with thickness, examples of these plots are shown in figs. 7.20 and 7.21, which are the longitudinal element stress and hoop element stress plots respectively for the small floor supported pipe. The positions of the elements under consideration (and their corresponding nodes) are shown in fig. 7.19 and this allows an explanation of the shape of the graphs to be made. When the test is underway, the region under the loading nose (including elements 193 and 221) will go from compression (negative

Fig. 7.19 Element mesh enlargement to show the selected node and element positions.

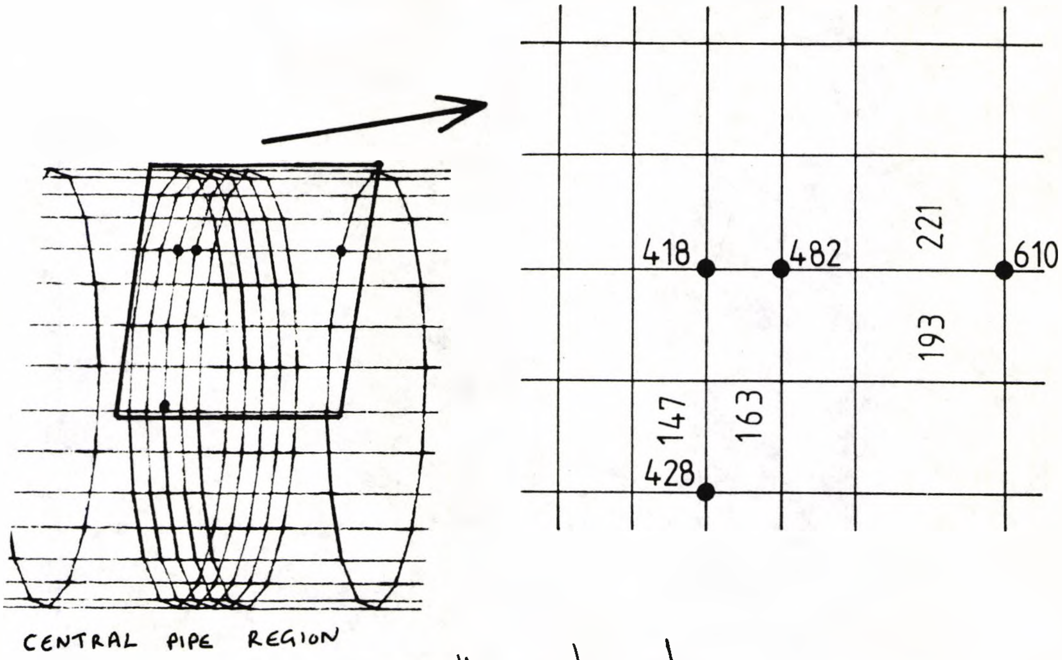

i.e. 418 is the centre node.

Fig. 7.20 Plot of longitudinal element stress against thickness for the small supported pipe.

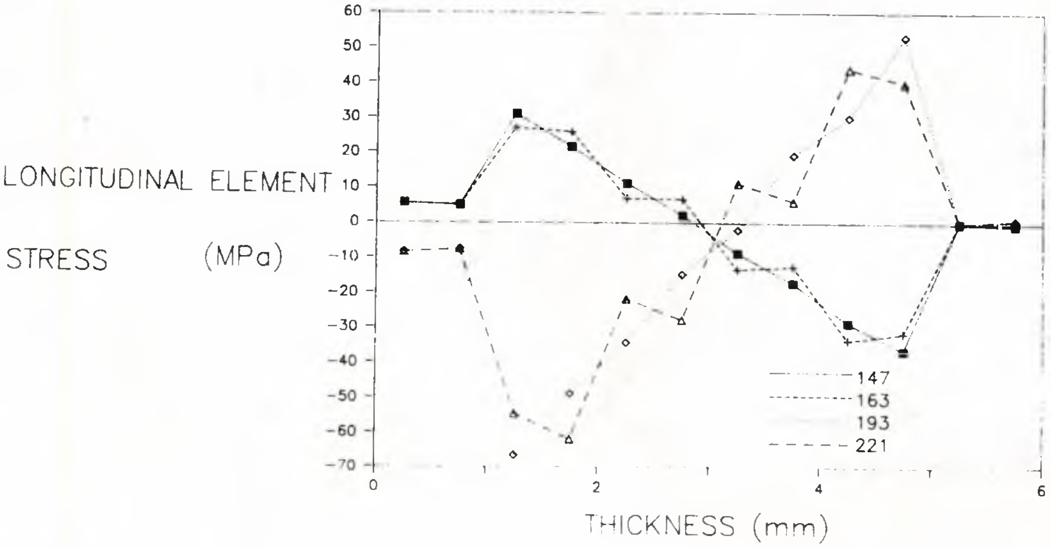

Fig. 7.21 Plot of hoop element stress against thickness for the small floor supported case.

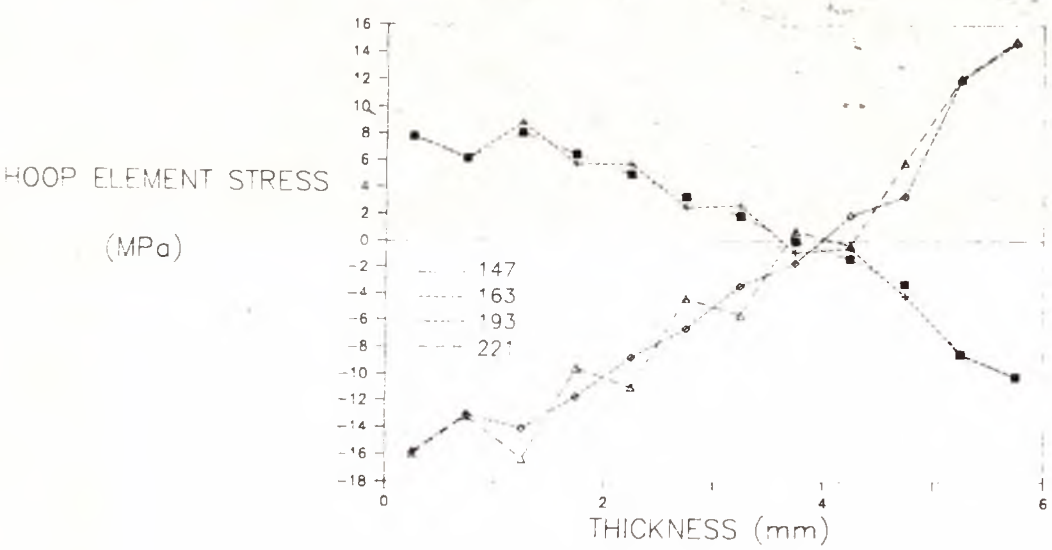

Fig. 7.22 Plot of nodal shear stress against thickness for the small floor supported pipe.

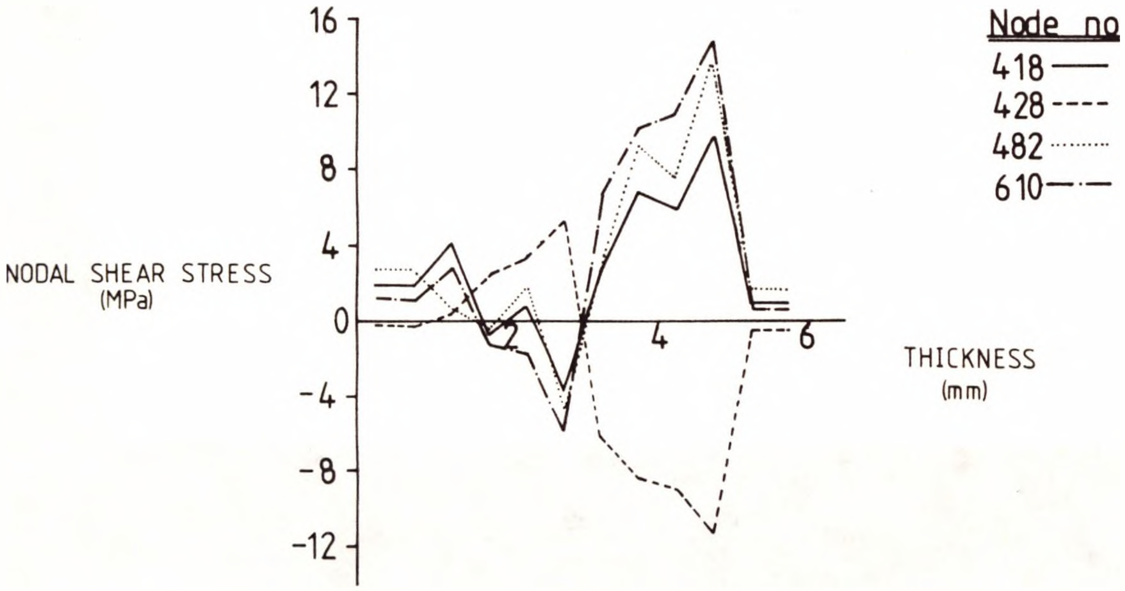

Delamination is a debonding process primarily resulting from unfavourable out of plane (through-the-thickness) stresses. These may be tensile, compressive or shear stresses, with tensile stresses thought to be the most common and effective delamination initiators. It is very useful to be able to predict between which layers the first delamination is likely to occur. The method suggested here is that the location of the first delamination is related to the difference in the inplane interlaminar shear stresses between adjacent layers, with the greatest difference resulting in the most likely location of the delamination. This is examined in the following pages, but it should be stressed at this point that the usual method of prediction would be to study the out of plane stresses (in particular the out of plane shear stresses) but this was not possible as the shell elements used in this analysis had no through the thickness capabilities.

stress values) to tension (positive stress values) through the thickness, whilst the region away from the nose (including elements 147 and 163) will begin in tension in the outer layers but will be in compression by the inner layers. This pattern is revealed in the plots included.

The same basic pattern is found when the S_{xy} plots are considered, as fig. 7.22 indicates. This is a plot of the nodal inplane shear stress against thickness for the floor supported small pipe and the location of the relevant nodes can be found by refering to fig. 7.19. As above, the change in sign can be explained by considering the change of stress state from tension to compression (and vice versa) at various positions around the pipe. What is particularly interesting about these S_{xy} plots is that they may provide a means of predicting between which layers delamination is most likely to occur. (see opposite page). Since failure is known to occur at the interface between two layers, this would suggest that the most important feature of fig. 7.22 is not the absolute values of shear stress but the difference in the values of shear stresses between adjacent layers. These result in the layers twisting across each other with a large difference in S_{xy} values resulting in a greater twisting effect and thus a greater chance of delamination. Observing fig. 7.22 reveals that the largest difference in shear stress between adjacent layers occurs at the pipe's centre, which points to delamination occurring at this interface first. Although it is tempting to continue this model by saying that the second largest difference in shear stress occurs at the innermost composite/resin interface, meaning that the next delamination would occur here, it should be noted that once the first delamination had taken place, this may alter the situation considerably. So, any prediction of the second (and subsequent) layers to delaminate may not be made with this simple model.

Although only the small floor supported pipe is considered here, it is interesting to note that virtually identical plots were obtained for both the large floor supported pipe and the small cradled pipe. The significance of this will be discussed later along with comparisons with the experimental situation.

At this stage, it is worth while pointing out some of the short comings of this model. The main problem is the lack of information in the out of plane (i.e. z) direction. It would have been interesting, for example, to view plots not only of S_{xy} but also of S_{xz}, S_{yz} and S_{zz} especially close to the interface. However, the laminated shell elements used in the model have no through-the-thickness capabilities. Thus it was decided to redo the model from scratch using 8-noded orthotropic solid brick elements, which would allow the out of plane information to be provided, whilst also giving the same stresses and deformations as the laminated shell model. The small pipe element mesh was used, with 6 elements in the thickness modelled as two gel coat and four composite layers, all 1mm thick (contrasted with 10 layers in the original model, eight of which were composites). The floor supported restraints were imposed on the mesh for an initial comparison with the previous model. The model was then run and the first drawback to using these elements was immediately apparent - the model took a very long time to run! Once the run had finished, the maximum displacement (found to be 2.50mm) was compared to that obtained for the floor supported case initially (i.e. 4.87mm), indicating the new model was not equivalent to the original laminated shell model. Several attempts at modifying and rerunning the solid brick model failed to result in anything like equivalence. Therefore, it was decided that due to the limited time available for computing in this particular project, the benefits of predicting stresses in the out of plane direction were outweighed by the time required to obtain them. It is strongly suggested, however, that use of the solid brick elements is pursued in any further modelling carried out in this particular geometry but it should be pointed out that in order to obtain what is actually required, i.e. the S_{xz} stresses at the interface, a very fine element mesh is needed in this region e.g it may be necessary to use as many as four elements per layer through the thickness. If the stresses are not made available close to the interface, this work will have no advantage over the modelling already done here.

Another drawback to the use of this particular package was that there is no capability for obtaining strain contour plots and data. These would have been very useful for comparing with the data from the strain gauged tests carried out in Chapter 5. It is possible to obtain displacement contour plots but these only yield information on where the top surface deforms.

However, the validation procedures carried out previously made this package much more trustworthy to use and this was considered more important than the shortfalls mentioned above.

7.3 Dynamic analysis.

This form of modelling was undertaken to examine the oscillatory behaviour of the small pipes under impact in both support conditions, and is important in determining the peak, transient loads in the pipe which may cause delamination initiation. This is caused by a combination of dynamic elastic response and the process of failure. At low velocities, elastic behaviour dominates and so dynamic behavior could be predicted by use of simple mass-spring models. Two models were considered.

7.3-1 Model A - a mass impacting a massless simply supported spring.

This model has previously been used by several groups of workers (see chapter 2, section 2.3-2) and regards the pipe as a massless spring being impacted by a mass, m, in this case the 38kg tup (see fig. 7.23b). From this approximation, the force, F_A, at any time ,t, can be calculated using

$$F_A = V_o(mk)^{\frac{1}{2}}\sin[(k/m)^{\frac{1}{2}}t] \qquad (7.2)$$

Fig. 7.23 Comparison of a) real situation with the mass-spring systems - b) model A, c) model B for a beam and d) model B for a ring.

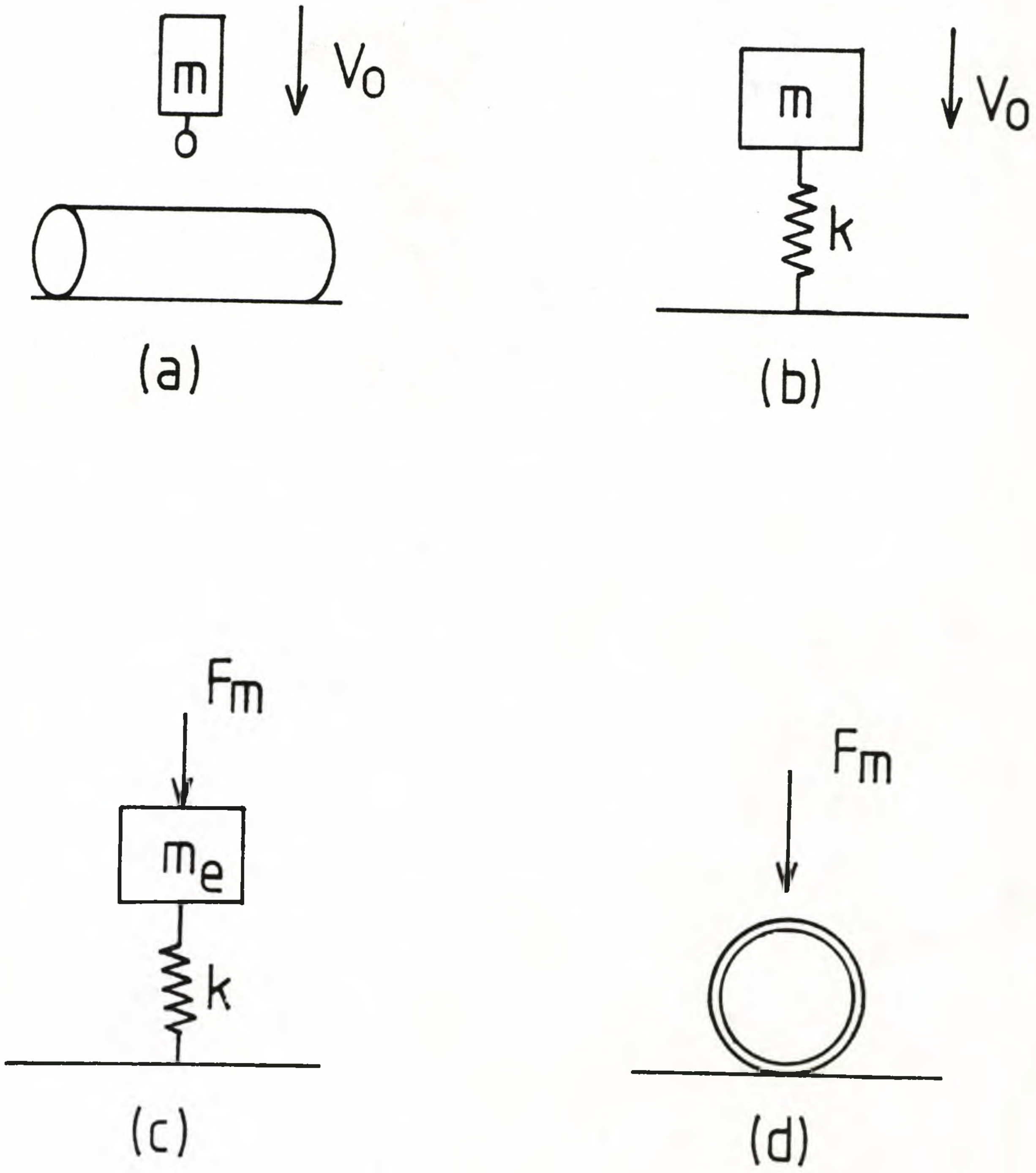

where V_o is the impact velocity and k the force constant of the pipe obtained from the average gradient of the force/displacement curve. To illustrate the success of this very simple model, table 7.6 lists the predicted and experimentally determined values of maximum force, F_M, and half period, $T_{\frac{1}{2}}$, for all the specimens considered. [For reference, IP1, IP3, IP5, IT11 and IT10 were the multiple bounce floor-supported specimens; S1, S5, S11 and S10 the single bounce floor-supported specimens and L7, L8, L9, L10, L3, L4, L5 and X2 the single bounce cradled specimens - see chapter 6].

It can be seen that, for the floor-supported specimens, good agreement is found between the predicted and actual values of F_M in all but three cases, these being IP1, IP5 and S10. In the case of IP5 and S10, poor prediction is probably due to pipes with an uneven cross-section being used, resulting in wall thickness variations of up to 1mm from one end of the pipe to the other. The probable reason for poor prediction in the case of IP1 is interference in the velocity/time history caused by the impact mechanism. This latter phenomenon manifests itself as a "blip" in the force/time history and is responsible for the inability to obtain actual $T_{\frac{1}{2}}$ values in many of the single bounce tests.

It should also be noted at this point that the poor reproducibility in nominally equivalent tests (i.e. the multiple and single bounce floor-supported tests, in particular S11 with IT11 and S10 with IT11) has already been noted and will be discussed in chapter 8.

Table 7.6 Predictions from Mass-spring Model A using a single linear value of k.

Specimen	V_o	k	Maximum force(N)		Half Period(ms)	
Number	(m/s)	($x10^6$N/m)	Actual	Predicted	Actual	Predicted
IP1	1.08	2.80	30470	11200	-	11.65
IP3	3.04	1.47	26000	22850	14.87	16.10
IP5	4.45	1.87	48240	37900	10.62	14.35
IT11	6.25	0.66	34940	31600	22.20	24.10
IT10	7.89	0.58	39350	37300	21.74	25.70
S1	1.10	2.20	9770	10120	-	13.05
S5	4.41	0.66	21490	22060	-	23.50
S11	6.10	0.45	21170	25230	22.60	28.80
S10	7.97	0.72	26370	41670	22.89	22.89
L7	1.00	3.58	10990	11660	9.80	10.50
L8	1.90	1.52	14030	14440	-	15.60
L9	2.91	1.13	16800	19050	-	18.10
L10	4.33	1.29	30680	30260	-	17.10
L3	5.81	1.08	30860	37180	-	18.60
L4	5.03	0.89	25290	29240	17.37	22.55
L5	6.39	0.80	24890	35220	-	21.65
X2	6.21	0.83	26930	34660	14.60	21.26

Considering now the cradled pipe tests, prediction appears to be less accurate at full damage than for the partial damage tests, and is definitely inferior to predictions for the full damaged floor supported specimens. This point is underlined by figs. 7.24 and 7.25, which compare experimental and predicted force/time curves for a fully damaged floor supported specimen (namely IT11) and a fully damaged cradled specimen (L4) respectively.

A second set of predictions using this model was also undertaken in an attempt to improve the accuracy, particularly in the prediction of $T_{\frac{1}{2}}$, where this was possible. These were performed by not representing k as a single average value as above, but by allowing it to vary as the slope of the force/displacement curve varied. This approach was used with some success by Christoforou et al (33). The predictions of F_M and $T_{\frac{1}{2}}$ for all the specimens are listed in table 7.7. This reveals very well how the model improves prediction of the tail of the force/time curve after peak load, resulting in either better or equal $T_{\frac{1}{2}}$ values in all but two possible cases. Maximum force prediction is also improved in 4/5 of the multiple bounce floor-supported specimens and is vastly improved in 3/4 of the full damaged cradled specimens i.e. L3, L4 and L5. [In the case of X2, to accomodate prediction of the very low half period of 14.60ms, the changes required in gradient result in the very high force prediction].

The next stage was to plot the experimental and

Fig. 7.24 Experimental and predicted force/time curves for IT11 using model A with a linear k value.

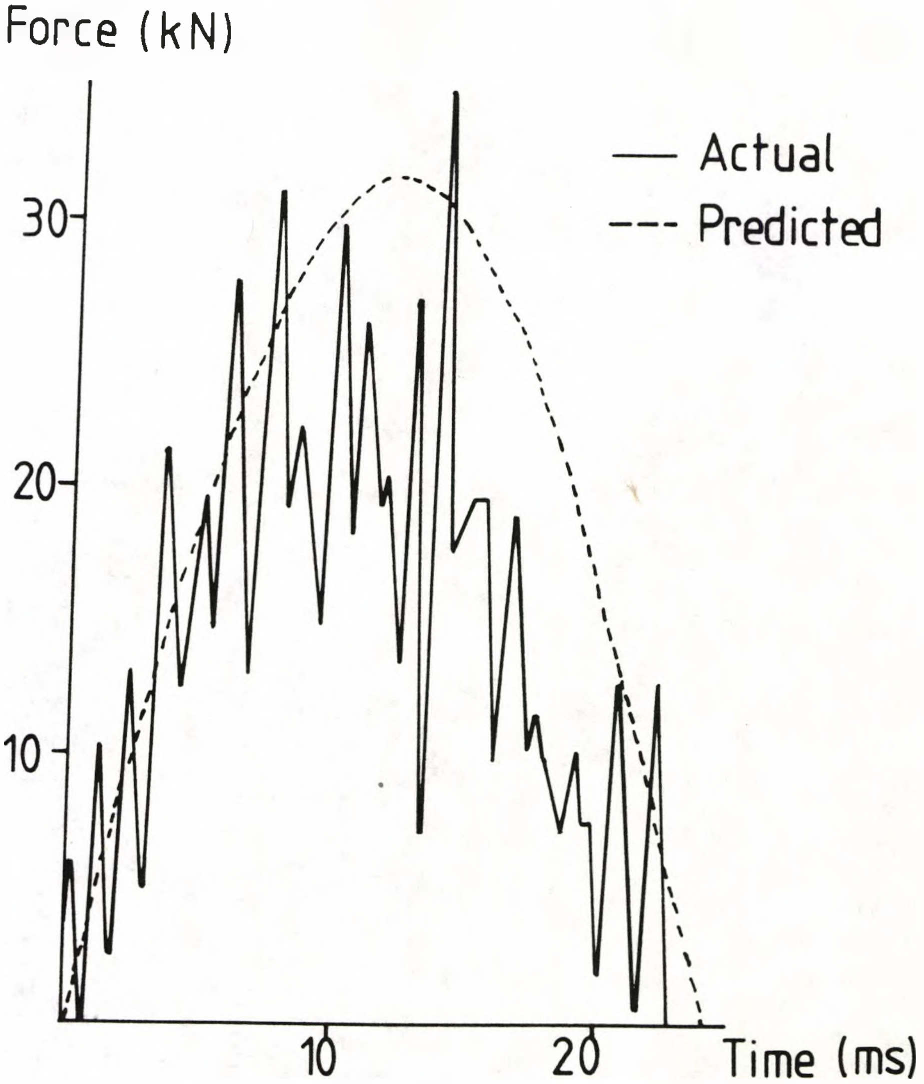

Fig. 7.25 Experimental and predicted force/time curves for L4 using model A with a linear k value.

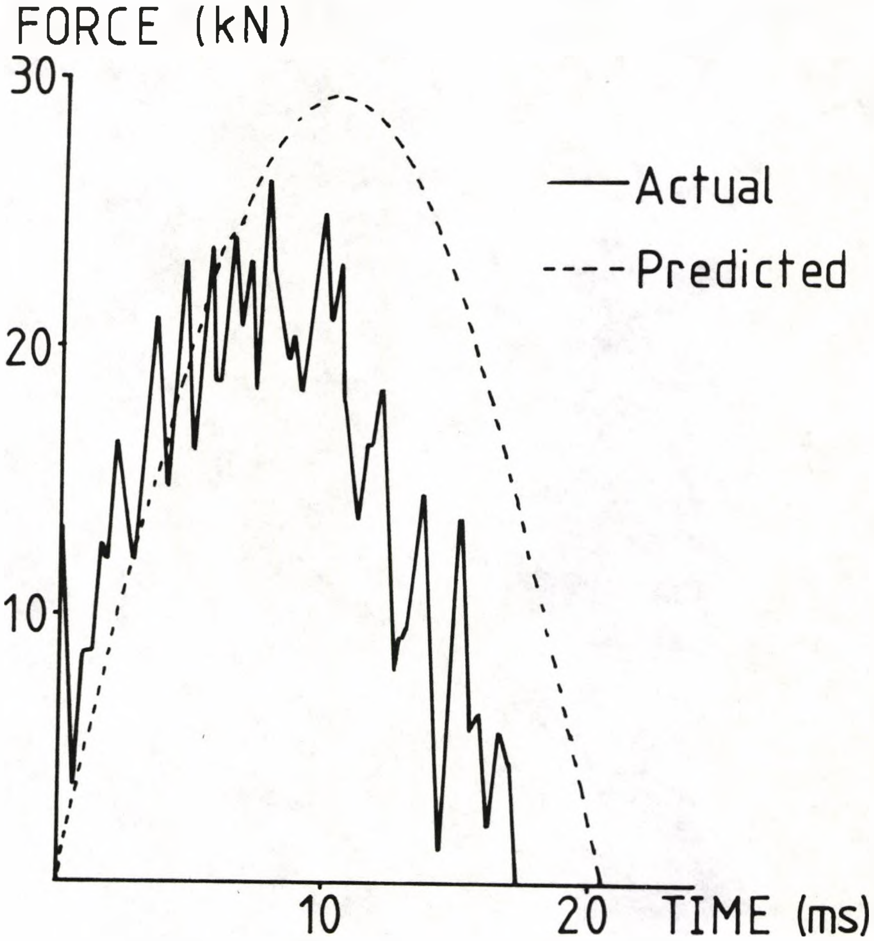

predicted force/time curves to see if, along with the trend of improved prediction of general behaviour characterised by improved F_M and $T_{\frac{1}{2}}$ values, this method provides a more accurate means of modelling the force/time curve. Figure 7.26 shows the actual and predicted curves for IT11 (similar plots being obtained for all specimens), and reveals that varying the gradient does improve general behaviour predictions but only slightly.

In order to look more closely at the pipe oscillations as opposed to general behaviour, model B was employed.

7.3-2 Model B - a massive simply supported beam subjected to a ramp load.

In this model, the pipe is characterised as an effective mass, m_e, with a linear spring (see fig. 7.23c), the effective mass being derived from beam theory as $m_e = 17/35 \times m_b$, where m_b is the beam mass. The mass is subjected to a ramp load of maximum value F_M and rise time, $t_r = \pi/2(1/w_n)^{\frac{1}{2}} = \pi/2(m/k)^{\frac{1}{2}}$, m being the tup mass as above. From this approximation, the force, F_B, at any time, t, can be calculated from

$$F_B = F_M \quad \frac{t}{t_r} + \frac{1}{w_n' t_r} \sin(w_n' t) \qquad (7.3)$$

It should be noted that in the above formula, $w_n' = (k/m_e)^{\frac{1}{2}}$, as the frequency is calculated for the pipe unlike the rise time value which is dependent on the tup mass, m, as stated above.

Table 7.7 Predictions from Mass-spring Model A using a Non-linear k Value.

Specimen Number	V_o (m/s)	Maximum force (N) Actual	Maximum force (N) Predicted	Half Period (ms) Actual	Half Period (ms) Predicted
IP1	1.08	30470	46123	-	14.80
IP3	3.04	26000	26487	14.87	15.60
IP5	4.45	48240	44856	10.62	10.70
IT11	6.25	34940	34754	22.20	21.60
IT10	7.89	39350	44022	21.74	19.00
S1	1.10	9770	19790	-	13.05
S5	4.41	21490	19130	-	27.50
S11	6.10	21170	27431	22.60	25.50
S10	7.97	26370	32560	22.89	29.25
L7	1.00	10990	11600	9.80	10.60
L8	1.90	14030	19900	-	10.70
L9	2.91	16800	12740	-	26.70
L10	4.33	30680	25600	-	20.20
L3	5.81	30860	28420	-	24.20
L4	5.03	25290	27200	17.37	22.05
L5	6.39	24890	29210	-	26.20
X2	6.21	26930	51280	14.60	13.20

Fig. 7.26 Experimental and predicted force/time curves for IT11 using model A with a non-linear k value.

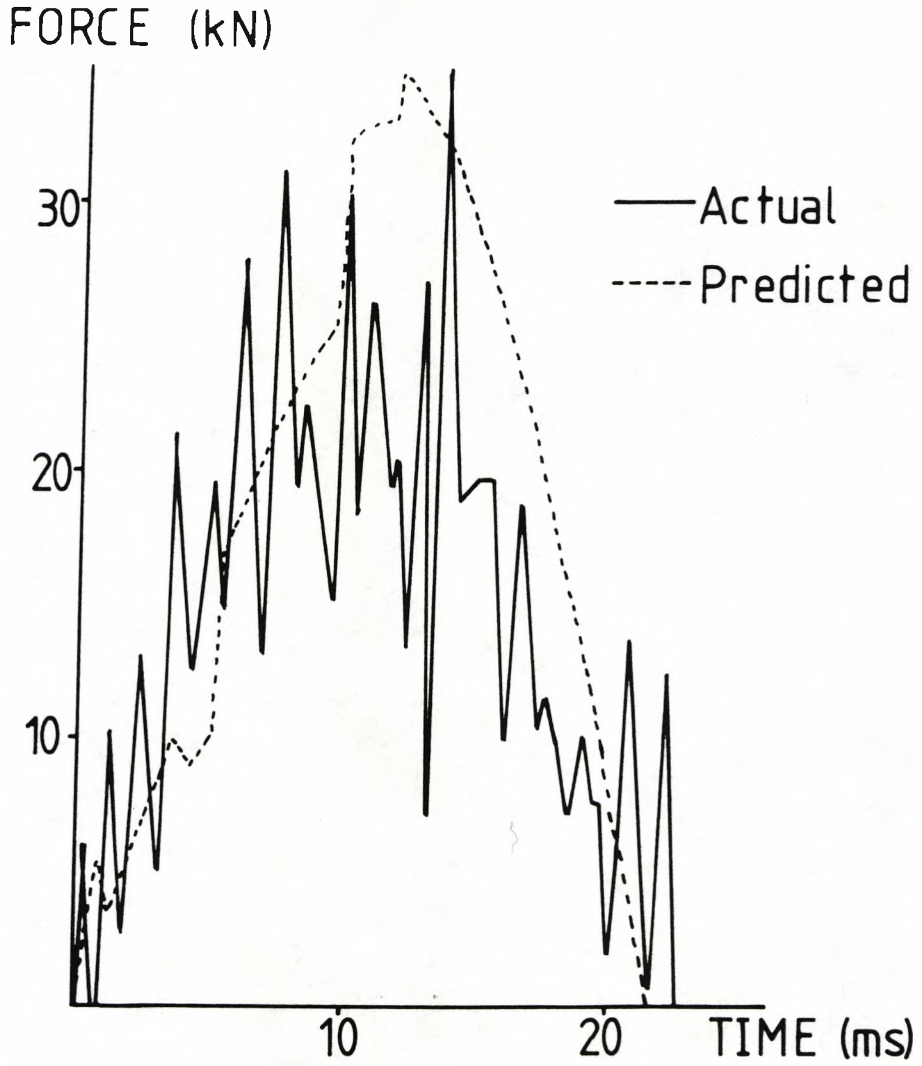

This model also allows the calculation of the period of oscillation, T_n, since $T_n = 2\pi/w_n' = 2\pi(m_e/k)^{\frac{1}{2}}$. The actual and predicted values of T_n are listed in table 7.8, and the actual and predicted force/time curves were plotted for each specimen. Reference to table 7.8 and fig. 7.27 (an example of superimposing the experimental and predicted force/time curves, namely IT11) reveals that although a reasonable general fit is obtained, T_n was not well predicted.

In a further attempt to improve T_n prediction, the model was then modified to represent a ring undergoing flexural vibrations (see fig. 7.23d). In this case, the general frequency formula is

$$w_n' = 2\pi f_i = 2\pi \times \frac{1}{2\pi}\left(\frac{EIi^2(1-i^2)^2}{pAr^4(1+i^2)}\right)^{\frac{1}{2}} \qquad (7.4)$$

This can be further simplified since it is known that for the mode of vibration required i=2 (92). Thus,

$$w_n' = \left(\frac{36EI}{5pAr^4}\right)^{\frac{1}{2}} \qquad (7.5)$$

where E is the modulus previously used in analytical work ($=1.8\times10^{10}$Pa), I the moment of inertia, r the pipe radius, p the density (previously measured as 1.91×10^3kg/m^3) and A the cross-sectional area. Initially, the pipe was considered to be a composite ring and this predicted T_n to be 0.34ms. Reference to table 7.9 reveals that this underpredicts the oscillation period though it is an improvement on the beam approximation.

A final attempt at increasing the accuracy was made by considering the pipe to be a purely resin ring of density 1.25×10^3kg/m^3 (91). This is a valid assumption

Table 7.8 Predictions from Mass-spring Model B using a Beam Approximation.

Specimen Number	m_e (kg)	t_r (ms)	w_n' (s^{-1})	Oscillation Period (ms) Actual	 Predicted
IP1	1.12	5.84	1581	1.50	3.98
IP3	1.11	8.05	1153	1.40	5.45
IP5	1.08	7.14	1317	1.70	4.77
IT11	1.11	12.02	770	1.10	8.16
IT10	1.12	12.82	720	1.10	8.73
S1	1.12	6.53	1403	0.94	4.48
S5	1.09	11.92	779	1.11	8.07
S11	1.12	14.43	632	0.96	9.94
S10	1.08	11.41	818	0.89	7.68
L7	1.43	5.11	1582	0.87	3.97
L8	1.43	7.85	1032	1.33	6.09
L9	1.45	9.10	884	1.28	7.10
L10	1.43	8.53	950	1.21	6.61
L3	1.45	9.31	863	1.13	7.28
L4	1.31	10.26	823	1.09	7.63
L5	1.32	10.83	777	1.16	8.09
X2	1.43	10.63	761	0.98	8.26

Fig. 7.27 Experimental and predicted force/time curves for IT11 using beam model B.

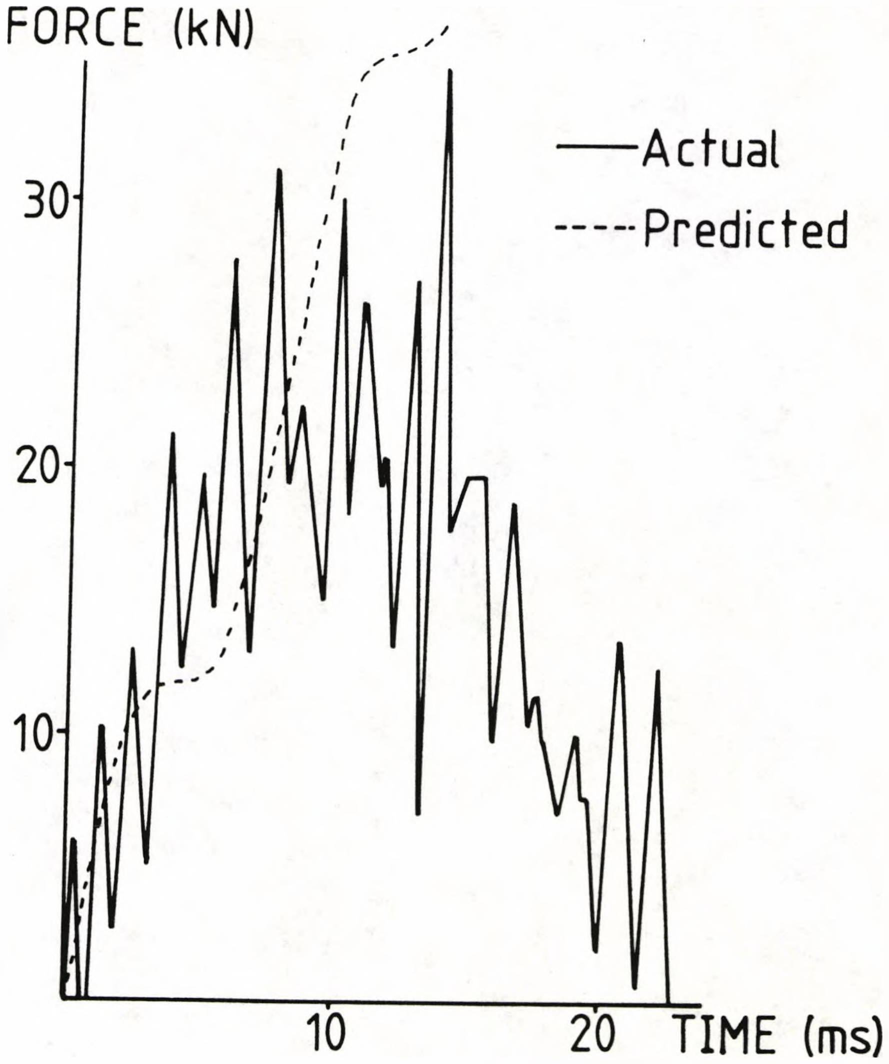

since the modulus of the resin (= $4x10^9$Pa) is closer to the pipe's transverse Young's modulus (=$8.27x10^9$Pa), which is more important when considering the flexural ring vibration mode than the longitudinal modulus. [The latter, at E_x = $3.86x10^{10}$Pa, is closer to the "analytical" composite modulus of $1.8x10^{10}$Pa]. For the above reason, it was expected that the resin ring prediction of T_n would be closer to the experimental values than the composite ring approximation. Reference to table 7.9 reveals this to be so, with T_n predicted as 0.58ms. Thus, the experimental values are found to lie between the beam and ring models, with, as expected, the resin ring model (and thus the ring mode of vibration) being the closest approximation to actual behaviour.

Superimposing the oscillations onto the initial rising ramp (i.e. plotting the F_B values for both ring models) has, however, proved less than successful, even in the best possible case, L7, see figs. 7.28a and b. This limited success is simply because the oscillations are not due to the inertial effects of the specimen alone, but arise from other sources, such as the vibrations of the impacting system itself. This was as expected.

Table 7.9 Predictions from Mass-spring Model B using a Ring Approximation.

Specimen Number	Prediction of period of oscillations (ms) Actual	Composite ring	Resin ring
IP1	1.50	0.34	0.58
IP3	1.40	0.34	0.58
IP5	1.70	0.34	0.58
IT11	1.10	0.34	0.58
IT10	1.10	0.34	0.58
S1	0.94	0.34	0.58
S5	1.11	0.34	0.58
S11	0.96	0.34	0.58
S10	0.89	0.34	0.58
L7	0.87	0.34	0.58
L8	1.33	0.34	0.58
L9	1.28	0.34	0.58
L10	1.21	0.34	0.58
L3	1.13	0.34	0.58
L4	1.09	0.34	0.58
L5	1.16	0.34	0.58
X2	0.98	0.34	0.58

Fig. 7.28 Experimental and predicted force/time curves for L7 using:

a) the composite ring model B.

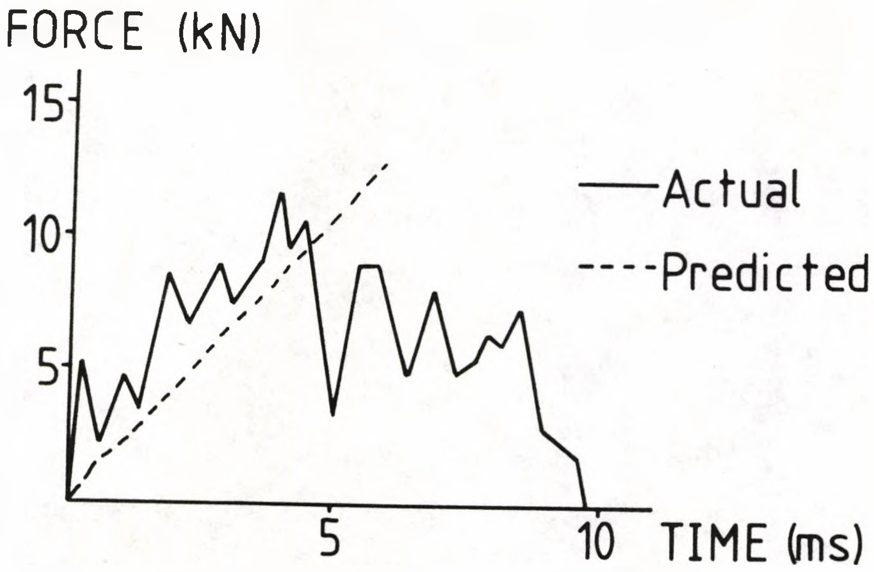

b) the resin ring model.

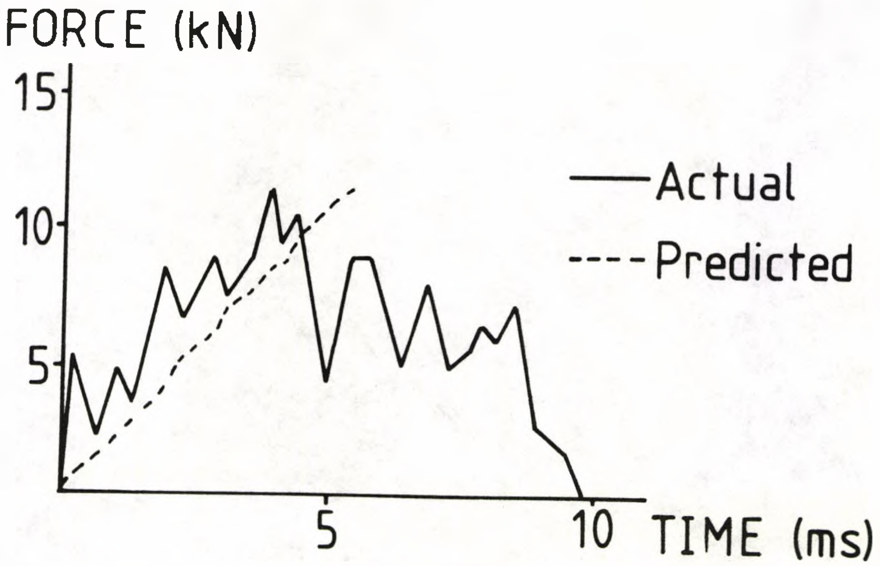

8. DISCUSSION.

This chapter serves to gather together the information obtained in the previous chapters (4 to 7) and to discuss the relevance of these results.

8.1 Testing of pipe sections.

Considering initially the floor-supported tests conducted on the 1/16th large diameter pipes and the 1/8th small diameter pipes, all of length 500mm, both geometries produced the same localised crush damage whether impact or static tests were performed. It consisted of a crater and gel coat cracking on the upper surface and delamination had initiated. This damage occurred very early in the tests (e.g at around 7kN for the small diameter pipes) despite the tests being continued to 95kN and shows up as a failure on the load/displacement curve (see fig. 4.2). This first failure is also seen in the testing of the half pipe sections at around the same peak load (5.68 to 8.40kN),

(see fig. 4.4). The results from the half pipe tests also confirm the weakness of the dark resin pipes, now known to be mainly due to their poor construction which leads to weak interlaminar and intralaminar bonding. Furthermore, the microscopy carried out in this section reveals that the failure mechanism does not involve fibre splitting as the cracks induced follow the fibre/matrix interface. Since this is known to be the weakest in the dark resin pipes, it is no surprise that these fail at the lowest loads.

The most interesting results from this section of work came from the three point bend testing of the 65mm span specimens. These tests were performed in the hope that a very simple geometry could be used to obtain correlations between residual properties and damage parameters, in this case the damage length and incident energy. The first thing to note is that there is a linear relationship between these two parameters, which has been noted before (e.g. by Liu (84) for glass/epoxy, Kevlar/epoxy and carbon/epoxy plates and by Christoforou, Swanson, Ventrello and Beckwith (33) for carbon/epoxy cylinders, all under low velocity impact conditions). Secondly, correlations were found between the residual properties and the damage parameters (see fig. 4.9 - 4.11). Residual peak load and gradient both decrease with increasing damage, whilst residual deformation increases with increasing damage after a certain value is reached. Before this point - about 12mm damage length caused by 11J of incident energy - increasing the damage has no effect on the deformation. This cutoff point corresponds to failure in the initial tests. The two sets of results are complimentary. Upon retest, the graphs reveal that the specimens become weaker and less stiff the more initial damage is done. Up to the energy needed to cause failure initially, this fall in stiffness and strength has no effect on the deformation needed to cause residual failure (i.e. failure in the residual tests). Beyond this point, the specimens have lost so much stiffness and strength that they need to deform further to cause failure.

8.2 Testing of large diameter pipes.

8.2-1 Static tests.

As can be seen from fig. 5.7, the static load/displacement curve for these pipes reveals a first failure point (marked 1) which, as in the 1/16th 400mm and 1/8th 150mm internal diameter pipe sections and half pipe tests, corresponds to the onset of damage. The damage takes the same form as in the above two tests and also occurs non-catastrophically. Observing the numerical information in table 5.3 shows that this failure occurs at a much higher load (between 14.25 and 19.75kN for the 9/10mm thickness pipes and between 17.50 and 24.50kN for the 12/13mm thickness pipes, excluding the video 3 pipe which will be discussed separately) than those quoted for the 1/16th 400mm and 1/8th 150mm internal diameter pipe sections and half pipe tests, but the latter are thinner (wall thickness of 6mm). Therefore, a more meaningful comparison would be with the tests conducted on 1/16th large diameter pipes. These underwent first failure at between 12.80 and 15.50kN, which shows reasonable agreement with the large diameter complete pipes of the same thickness (9/10mm).

[N.B. The pipe thickness must be carefully measured before testing as the above shows it is a very important parameter. This is underlined by the data in tables 5.3 and 5.4, which show that the thicker the specimen, the stiffer it is throughout the duration of the test. This was expected, since the variation in wall thickness is due to more reinforced layers being present in the 12/13mm thickness pipes.]

The first failure of the specimens was further investigated by performing two variations on the static test theme (strain-gauging and damage process observations) to study how the failure actually occurs.

Considering firstly the strain gauged tests, examples of the output from these is presented in figs. 5.8 - 5.11. These spotlight the strain variations with gauge type (axial or hoop) and gauge position. Fig. 5.10 illustrates the variations for hoop and axial gauges placed axially from the pipe midpoint in the first test. The three axial gauges show, apart from an initial very small negative region for gauge 9, positive (i.e. tensile) strains, while the hoop gauges show negative (i.e. compressive) strains. Although the main features can be picked out easily in all but the trace for gauge 14, it is interesting to note that the effect of distance is clearly discernible. Gauges 13 and 14 are the furthest (ie 400mm) away from the loading region and have the smallest strains (indeed for gauge 14, there is almost no strain trace at all). This emphasises the very localised effect that the static tests produce. Fig. 5.11 considers the variations for gauges placed in the hoop direction from the midpoint of the pipe in test 2. Here, all the strains are small and tensile with the largest strains recorded at 300mm distance in the hoop direction. Very small strains were recorded 100mm from the loading region. This is explained by considering the shape of the pipe as it deforms during the tests, which changes from circular to ellipsoid. It is this bowing out of the pipe that leads to the highest strains being furthermost from the loading region.

Figs. 5.10 and 5.11 confirm what was already expected i.e. the localised nature of the damage along the pipe axis and the effect the change in pipe shape has during testing. However, the most interesting data generated forms fig. 5.8 as this does provide new information about the process of failure for the pipes. This figure illustrates strain variations for a strip of gauges positioned at 25mm axially from the pipe midpoint. All the gauges were of the axial type and eight of the ten available were used. The traces show the initial failure at 14.25kN, marked with a change in gradient, very well. After this point, large tensile strains were observed for all 6 gauges, with the furthest positioned gauge showing the smallest strains, in agreement with fig. 5.10. [It should be noted that the "strange" behaviour exhibited by gauges 1 and 2 at around 19kN and 21kN respectively is due to the gauges being destroyed by the loading nose]. However, it is the strain variation before first failure which is the most informative and so this part of the curve was enlarged to produce fig. 5.9. It was expected that the main feature of this graph would be a sudden change in gradient at around 14.25kN (i.e.

the value for first failure from the corresponding load/displacement curve). However, there is a sudden change in behaviour well before this point at around 12kN, which is also the value on the load/displacement curve where non-linear behaviour begins. Based on these findings, a plausible theory for the first failure process can be put forward. This is that the first event is local crushing, marked by slight non-linearity of the load/displacement curve and the sudden change in the load/strain plot (see fig. 5.9). This acts as a precursor to delamination initiation i.e. the process involves two distinct steps. [N.B. The delamination initiation causes the drop in load on the load/displacement curve at 14.25kN.] This theory suggests that the original idea that first failure was mainly due to initial crush but also marked the onset of delamination growth and that these two events are concurrent is not applicable.

It should be noted at this point that although only four of the graphs generated from the strain-gauged tests are considered here and in spite of the variation in pipe thickness already discussed, exactly the same trends exist in all three tests completed.

The above tests yielded new information about the first failure process. The video tests, performed to monitor delamination growth, yield information about the second failure. This is caused by the growth of the major delamination, the process of which is illustrated in figs. 5.12 - 5.14. For all pipes tested, initially only very slow, non-symmetric growth is observed. This is hardly visible at all using the video frame advance button. For tests 1 and 3, there is a period after this of initial creeping when the growth speeds up slightly. In these two cases, the major delamination is a single event, occurring in just 2 milliseconds. The process is slightly different in test 2. Here, the major delamination is a two-part process, each part taking 2ms to occur. So, from the video observations, it can be concluded that once the crush and delamination initiation processes have occurred, the next process is slow, creeping growth. This may give way to slightly faster growth before the major delamination occurs, the latter taking place within 2ms. If the video is left running, the process of very slow growth begins again.

The damage patterns were recorded at test end by taking periphery photographs using the backlighting technique. This proved a very successful method of mapping the delaminations (see fig. 5.15).

There is one question left unanswered when considering static tests and this is why did the video 3 pipe produce such a different failure mechanism to the other 6 pipes tested i.e. why should it fail with an initial catastrophic failure? As already noted, this catastrophic failure has been seen before, but only for half pipes. Therefore, the question becomes what is different in either the test conditions or in the pipe itself for video pipe 3? Looking initially at the test conditions, there are two things to comment on. The first is the crosshead speed during the experiment which was 50mm/min. This could induce the different failure mechanism but it did not do so in the case of the other two videoed pipes. The second test condition was the pipe length (2.5m). Again, this is not likely to be the cause of the change in failure pattern because the strain gauges have shown how localised the damage is. Therefore, test conditions are not the cause of the variation. If the video is observed, it seems that the delamination growth is as in the other two cases. However, if the numerical information from the load/displacement curves is observed (see tables 5.3 to 5.5), these give some indication as to the different behaviour. The pipe is the stiffest of all those considered and its first failure load is much higher than the other pipes of this thickness. It could be that the failure is catastrophic because the precursor stage does not take place i.e. the resin did not yield. Then, increasing the load and thus the energy causes the pipe to fail and since more energy has been applied, it must be somehow dissipated. This then causes catastrophic failure. If this is the case, catastrophic failure here is due to a very different process than the believed geometric reason for this failure in the half pipes.

8.2-2 Pipe-drop impact tests.

As already stated, very little additional information was available from these tests but there are a few points of interest arising from them. Firstly, almost all the deformation under the loading nose is recovered after impact. This was also found in the static tests. The actual damage observed at test end is similar to that seen in equivalent energy static tests, but a greater number of delaminations providing a greater total area of damage were found in the impact tests. This could be due to pipe drop and not drop weight tests being carried out, or could be a feature of impact failure as opposed to static failure, but insufficient information is available to reach any conclusions. Since no drop weight tests have been carried out for this pipe diameter, it was hoped that the small diameter pipes would either have the same area of damage for the static and impact tests (and therefore show that the differences were due to performing pipe drop and not drop weight tests) or different areas of damage. The latter would show that impact and static tests for the floor-supported geometry are not equivalent as was originally hoped. This does emphasise the need for drop weight tests to be carried out for the large diameter pipes in any future work undertaken. [N.B. It should be noted that the difference in areas of damage is not due to the multiple bounce nature of the tests. Although the pipe did hit the nose more than once, it did not do so in the same position. This resulted in a trail of separate delaminations down the pipe length which did not affect the initial damage pattern.]

8.3 Testing of small diameter pipes.

8.3-1a Initial tests on floor-supported pipes.

The first thing to note is that these small diameter pipes exhibit a first failure point at around the same peak load as in the half pipes and "flat" bars of the same wall thickness (see fig. 6.7a). The damage sustained by the pipes is of the same nature as that seen in all previous floor-supported tests on both sections and large diameter complete pipes i.e. a crush crater and gel coat cracking were found on the upper resin surface and delamination had initiated. After this failure point, the load/displacment curve continued with a less steep gradient, with progressive delamination and crush damage occurring. No final catastrophic failure process was observed since the remainder of the pipe continued to support a load even after major damage and well beyond any practical design limits had been passed. Once the load was removed, nearly all the deformation was recovered.

The dynamic curves show reasonable agreement with their equivalent static curves (see fig. 6.2a). Although it is not possible to pick out the first failure point due to the oscillations on the curve, similar damage is seen if a partial test to this energy is performed. Comparing the damage at test end with that in the impact tests reveals that damage is very similar with the only differences being degree of severity. The multiple bounce tests, as suspected, were the most badly damaged, with the static tests having the least delaminations.

For damage observations, performing partial tests and using the backlighting technique to reveal the delaminations has proved a very useful tool. To supplement this information, destructive analysis was carried out (for the specimen details, see section 6.1-3). After first failure (see figs. 6.13a and b), a crazing pattern was observed. This has previously been seen in flat laminates (10), (21), (25).

Delamination has occurred throughout the specimen thickness and not, as expected, between just two layers. However, the growth of one of these delaminations must be more favourable since, after a load of 15kN in the static tests and in the single bounce tests at a load equivalent to 20kN in the static tests, a single delamination is seen to extend around the middle layer (see fig. 6.14). By test end, the damage seen in the specimens was very severe. For the static tests, up to three major delaminations (depending on pipe type) were observed, whereas for the impact tests, nearly all the layers had delaminated for equivalent energies. This appears to indicate that equivalent static and impact tests do not produce equivalent damage as was originally hoped, but this point will be further investigated when considering the residual property tests.

Before this is done, there are two points of interest arising from the numerical data extracted from the load/displacement curves (see tables 6.6a and b, 6.7

and 6.8). The first is a further indication of the need for good quality control, with the static test data for pipes of two different wall thicknesses (6mm and 5mm) quoted. The 5mm thickness pipes fail at loads of around 14kN, with the thicker pipes (due to their having more reinforced layers) failing at much higher loads of between 27.3 and 32.5kN.

The second point of interest is the differences in data for the single and multiple bounce impact tests, which had been performed on what appeared to be identical pipes as far as wall thickness (6mm) and resin colour (medium) were concerned. There are several possible reasons for this. Firstly, it is possible that the pipe from which the single bounce test specimens were cut had been damaged either during delivery, storage or sectioning but this is not likely to be the case since any damage would have been revealed by the backlighting technique. A further possible reason for the differences in data arises from the extraction of the numerical information from the load/displacement curves. This is a definite source of error since it is dependent on the ability of the experimentalist to obtain the data and on the raw data itself e.g. it is easier (and more accurate) to read the graphs if the largest sensible peak load scale is used and the deflection scale is adjusted to give an initial slope on the load/displacement curve of around 45°. However, although these points must be taken into account, it should be noted that this is not believed to be a factor here since, once the differences were revealed, the raw data for both sets of tests was rechecked for major inaccuracies and none were found. A final possibility for the differences is that the pipe used for the single bounce tests was in some undetectable way weaker than that used for the multiple bounce tests, and this is the most likely explanation for the observed variations between the multiple and single bounce tests.

8.3-1b Residual property tests on floor-supported pipes.

For the partial damage tests i.e. those conducted to before the second failure point, retests produced new delaminations. However, once the second failure point had been passed in the original tests, no new delaminations were formed upon retest: the existing delaminations simply increased in size, with the multiple bounce impact tests producing delamination lengths of up to 360mm. Therefore, this indicates that after the second major failure, all the layers between which delamination is going to occur have delaminated and beyond this point the only process which can occur is growth of the existing delaminations.

The main reason for performing these tests was to look at the effect of initial tests on the strength and stiffness of the pipes (i.e. to measure their residual properties). It was originally hoped that the static and equivalent energy impact tests would produce identical plots, meaning that static tests alone could be performed and the results from these used to assess the impact performance of the pipe. Regarding figs. 6.16, 6.17, 6.18

and 6.19 reveals that this is not so, although behaviour is similar in all cases. The best agreement between static and impact residual properties is seen in fig. 6.18, which plots residual gradient against incident energy (6.18a) and against delamination area (6.18b). Here, all three sets of data points (i.e. from the static, single bounce and multiple bounce impact tests) follow the same pattern of an initial rapid drop in gradient, followed by a much slower drop with increasing amounts of damage. As expected, the multiple bounce impact tested specimens were the least stiff, followed by the single bounce impact specimens and then the static specimens. What is very interesting is that when the residual gradient is plotted against the area of damage, (6.18b), the three curves all tend to one common value of about 0.14N/mm, indicating that there is a lower limit of stiffness which the pipe retains and that this limiting value is the same independent of the original test method. Fig. 6.17 shows the plots of residual peak load against the two damage parameters, and this is not as expected. Both graphs show that as soon as first failure has occurred, the peak load attained on retest falls, but to different values depending on the original test type, i.e. to 18kN for the static tests and to 13kN for the impact tests. These two values of residual peak load then remain constant despite increasing amounts of damage and even despite the second failure. This indicates that the first failure (already known to mark the onset of delamination initiation) is a very significant event as far as the floor-supported pipe's strength is concerned in spite of the very small amount of damage visible at this point. This is important to note when deciding if the pipe has been damaged enough to take it out of service. Fig. 6.19 plots residual deflection against the two damage parameters and in this case behaviour appears to be very different for the static and single bounce impact tests. The static curve shows a plateau region before the deformation needed to cause failure increases more rapidly. The impact curves do not mirror this behaviour at all, with the residual deflection against incident energy data being very difficult to represent graphically (see fig. 6.19a). Fig. 6.19b, which plots residual deflection against delamination area, appears to be a straight line, which may indicate that the initial plateau region as seen in the static tests is missing in this case. This is possibly due to the greater amount of damage done by impacting as opposed to performing static tests. Fig. 6.16 underlines this by showing that both the total and projected delamination areas are smaller for equivalent energies in the static tests than in either of the two impact test types, for all specimens tested. A possible reason for this is the actual duration of the tests. In the static tests, the load is applied slowly (i.e. at a rate of 5mm/min) and the pipe is able to deform gradually. In the impact tests, the load is applied over a much shorter period and so the gradual deformation process does not occur, resulting in the pipe being more badly damaged. The gradual deformation process is aided by the deflection of the pipe ends to an elliptical shape (as predicted by NISA2) and it is interesting to see what effect this has on the pipe damage. This can be assessed by seeing what effect not allowing the ends to deform has i.e. in the cradled tests.

The overall comment for this support condition is that the static and impact tests are not equivalent. Thus without knowing the differences i.e. without actually performing the tests, it is not possible to use static tests to model impact behaviour, except to study the effect of damage on the gradient, which is a measure of the pipe's stiffness. It was also hoped that the impact tests could be modelled by performing static tests on a very simple geometry (i.e. the 1/8th small diameter pipes with a test span of 65mm supported in three point bend configuration). This was also not possible, as even the general trends observed in these tests were not seen in the complete pipe tests.

8.3-2a Initial tests on cradled pipes.

The first thing to note here is that once again a two-part failure process exists, with the static load/displacement curve (see fig. 6.20) having a similar shape to that obtained for the floor-supported small diameter pipes. It is interesting to note that the first failure point occurs at around the same peak load (7.50 - 8.50kN) as all other tests performed on pipes and pipe sections of the same wall thickness. This points to this failure process (consisting of local crush damage and delamination initiation) being independent of support conditions. After this failure point, the load/displacement curve continued with a steep gradient, with progressive delamination and crush damage occurring. As in the floor-supported case, a second failure point did occur and this was also not catastrophic, with the pipe still capable of supporting a load. The second failure point occurred at a lower load for the cradled pipes (18.70 - 20.75kN as opposed to 27.30 - 32.50kN for the floor-supported pipes). This is believed to be due to the cradles restricting the pipe's transverse deformation i.e. not allowing the pipe's ends to deform to an elliptical shape. This may result in higher stresses being generated, which would thus result in the pipe failing at lower loads.

The dynamic load/displacement curves agreed very well with their equivalent static case, although as in the floor-supported tests, it is not possible to pick out the first failure point due to the oscillations on the curve.

Comparing the damage at test end in the static tests with that in the impact tests reveals that damage is very similar, but is slightly more severe in the latter case. For both cradled test types, damage is far less severe than in the equivalent floor-supported pipe tests. Thus the effects of restraining the pipes in the cradles appears to be to cause them to fail at lower loads and for lower energies, by not allowing the pipe to deform transversely. The second failure is then achieved at lower energies, meaning that the resultant delamination areas are smaller than their floor-supported counterparts.

To supplement the information gained by performing partial damage tests and then analysing the delamination patterns using the back-lighting technique, destructive analysis was carried out (for the specimen details, see section 6.2-3). Both static and impact tests revealed very similar damage and delamination areas up to the second failure point, with the former agreeing very well with that seen for the floor-supported condition. At first failure, for example, a very localised crazing pattern was observed throughout the specimen thickness exactly like that seen for the floor-supported tests. The damage observed after the second failure had occurred was, as already discussed, much less severe when the cradles were used to restrain the pipes, and differences were observed between the cradled static and single bounce impact test specimens. In the static tests, one major delamination was observed at around the central layer, whilst in the single bounce impact tests, by full specimen damage two major delaminations were observed in layers 4 and 10, compared with the equivalent floor-supported cases, where delamination was found to extend to virtually all layers. This appears to indicate that equivalent static and impact tests produce equivalent damage only up to before second failure. After this, the single bounce impact specimens become slightly more badly damaged than their equivalent static tests, but it could be possible that for at least part of the energy range, static tests could be used to model the impact behaviour. This point will be further investigated when considering the residual property test results.

8.3-2b Residual property tests on cradled pipes.

Upon retest, the damage sustained was found to follow the same pattern as for the floor-supported pipes. For partial damage tests, i.e. those conducted to before the second failure point, retests produced new delaminations. Once this second failure had been passed in the original tests, however, no new delaminations were found on retest, with the existing delaminations simply growing. This indicates that once second failure has occurred, all the layers between which delamination is going to occur have delaminated.

The main reason for performing these tests was to look at the effects of the initial tests on the strength and stiffness of the pipes (i.e. to measure their residual properties). As with the floor-supported tests, it was originally hoped that the static and equivalent energy impact tests would produce similar plots, meaning that the static tests alone could be performed and the results from these used to assess the impact performance of the pipe. Regarding figs. 6.22, 6.23, 6.24 and 6.25 reveals that, unlike the floor-supported case, this is a distinct possibility, especially for the residual gradient (fig. 6.24) and the residual deflection (fig. 6.25). The former shows the same general pattern as in the floor-supported pipe cases, with the gradient showing a steep decline followed by a much slower drop with increasing amounts of damage. Here, agreement between static and impact tests is good despite the initial very high gradients seen in the impact tests. Agreement between the two test types is also very good for the residual deflection plots (see fig. 6.25) until an incident energy of 600-620J and a delamination area of around $0.2m^2$. Before this point, which corresponds to specimens originally tested to beyond second failure, the curves show a very gradual increase in the amount of deflection needed to cause failure upon retest (i.e. from 36.5 - 42mm). Beyond this point, there is a sharp upturn in the values of the deflection needed to cause residual failure, which ties in very well with the observation that delamination growth, which requires increasing deflections, is occurring in this area. It is interesting to note that at this point, the curves for the static and impact tests begin to separate, this being especially noticeable when residual deflection is plotted against delamination area, fig. 6.25b. This finding is underlined by the total and projected area of damage against incident energy plots (figs. 6.22a and b respectively). Here, there is reasonable agreement for the originally partially damaged specimens with the curves separating for the test specimens originally taken to full damage. This is especially pronounced for the projected area of damage against incident energy plots, indicating that there is more delamination growth for the impacted specimens than those originally statically tested. These curves all indicate that static tests can be used to model impact behaviour for specimens tested up to the level equivalent to cause second failure if the deflection is the required parameter, or for all but the first data points if the gradient is the required parameter.

The final residual property to consider is the peak load (see fig. 6.23). These curves are very different to the floor-supported plots, with the residual peak loads falling gradually for both test types instead of falling suddenly to a constant value. As far as modelling the impact behaviour by performing static tests, this is perhaps possible for slightly damaged specimens. However, as the damage increases, the two curves separate, with the residual peak load falling to 19.75kN for the static retests and 17.50kN for the impact retests. This is possibly due to the impacted specimens being slightly more badly damaged than the equivalent statically tested specimens, resulting in the impacted specimens being able to support less load on retest.

This property apart, the original hope of being able to perform static tests to model impact behaviour has been achieved for this support condition at least for a majority of the energy range for both the residual gradient (a measure of the pipe's stiffness) and residual deflection. These findings show the effect of not allowing the pipe ends to deform by restraining them in the cradles. If the pipe is restrained, static and impact behaviour is very similar. Remove the restraints, i.e.

perform floor-supported tests, and it is no longer possible to model impact behaviour using equivalent static tests. This underlines the idea mentioned earlier that the differences in behaviour for the floor-supported static and impact tests is due to the ability of the pipe to deform at its ends, since when the pipe is not allowed to deform in this manner, behaviour is similar for the two test types.

It was also hoped that the impact tests could be modelled by performing static tests on a very simple geometry (i.e. the 1/8th small diameter pipes with a test span of 65mm supported in three point bend configuration). This is a possibility in this case (unlike the floor-supported condition) since the same general trends are observed (compare figs. 6.23, 6.24 and 6.25 with figs. 4.9, 4.10 and 4.11). However, more work is needed on these two test types to determine any possible scaling factors and to firmly establish the similarites between the two geometries. This is a definite candidate for future work.

8.4 Modelling by analytical, finite element and dynamic analysis methods.

8.4-1 Analytical method.

The point to note here is the effectiveness of the very simple analytical solution (see equation 7.1). In the floor-supported cases, this gives a good first approximation for both the large and small diameter pipes, predicting displacements of 10.77mm and 4.73mm respectively. These compare very favourably with experimental values of between 8.50 and 10.00mm for the large diameter pipes and between 5.50 and 6.50mm for the small diameter pipes. It is unfortunate that no equivalent simple analytical solution could be found for the cradled support condition.

8.4-2 Finite element methods.

Using NISA2 to predict the situation at first failure has proved successful for both displacement and stress behaviour. Considering the former, NISA2 allows the values of displacement up to first failure to be well predicted, with figs. 8.1 and 8.2 illustrating the very good agreement for the large and small diameter floor-supported pipes respectively. These plots reveal several interesting points. Firstly, fig. 8.1 shows that although behaviour is well predicted up to first failure, in order to predict beyond this point, a change to the pipe's properties would need to be inputed to cope with the loss of stiffness caused by delamination initiation. Secondly, both plots illustrate the very significant effect of varying the pipe's wall thickness, since both consider two different wall thicknesses. [N.B. In fig. 8.1, the NISA2 prediction and the experimental load/displacement plots for pipes 1 and 2 consider pipes of wall thickness 13mm whilst pipe 3 had a wall thickness of 12mm]. The plots both indicate that the thicker the pipe, the stiffer it is (i.e. the higher the gradient of the load/displacement curve), which was as expected. Finally, it can be seen that the NISA2 predictions do not go

Fig. 8.1 Comparison of the experimental and predicted load/displacement plots for the large diameter pipes.

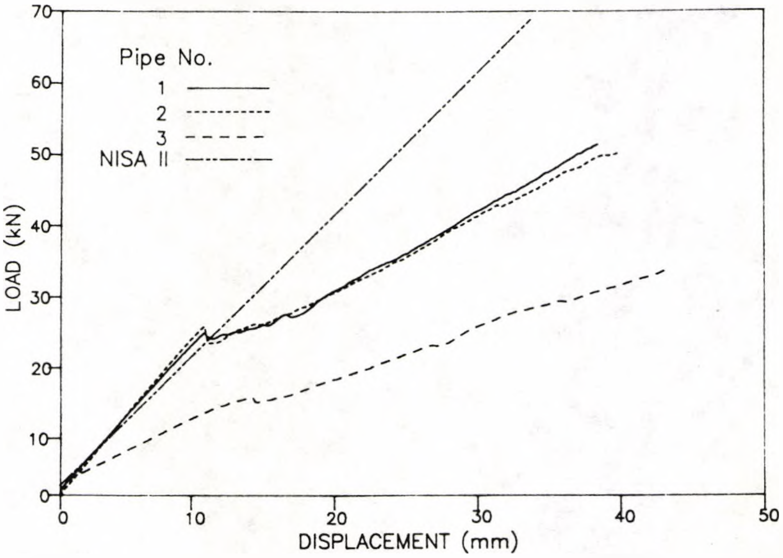

Fig. 8.2 Comparison of the experimental and predicted load/displacement data to first failure for the small diameter pipes.

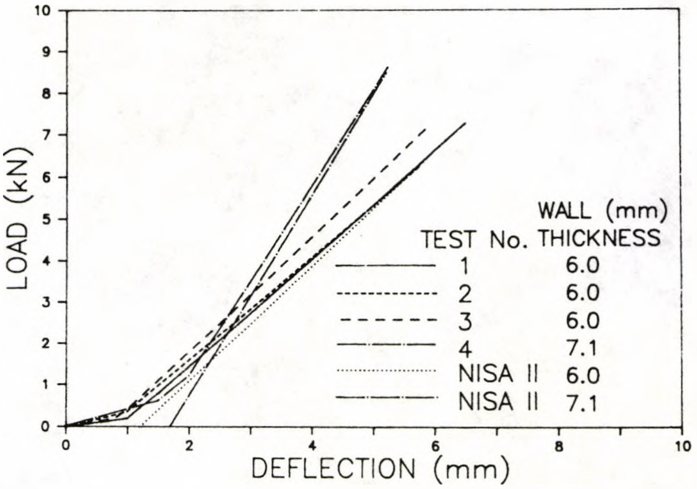

through the origin in fig. 8.2. This is simply because no account is taken of the initial portion of the curve, which is due to the initial stages of the test i.e. to the first irreversible resin indentation and the compliance of the Instron. The NISA2 data should actually start after this region, but has been extrapolated back to cross the y axis.

Comparing the analytical and finite element predictions of displacement at first failure for the floor supported condition shows that the finite element method only improves prediction very slightly (see tables 7.3 and 7.4). This further underlines the usefulness of the simple analytical solution.

Turning to the cradled support condition, prediction of the displacement at first failure to be 3.68mm shows excellent agreement with the experimental values of between 3.50 and 3.88mm, with the predicted value actually lying within the experimental range.

In all cases (i.e. for both pipe diameters and both support conditions), the deformed shape of the pipe is very well predicted (see fig. 7.3).

As far as prediction of stress behaviour is concerned, the first plots generated were of the average inplane shear stress through the pipe layers, an example of which is shown in fig. 7.4. If these are compared with the experimental delamination patterns (for examples, see figs. 6.8 - 6.10 and 6.21), it can be seen that prediction of the type of "butterfly" patterns which are obtained experimentally is achieved. More accurate predictions of the stress patterns have been obtained by looking at the stress contours on each layer through the pipe thickness (see chapter 7 for several examples). One very interesting feature of these plots is that they identify the antisymmetric effect found experimentally between two adjacent layers with different orientations (i.e. ±55°). It should be noted that predictions of both the average shear stress and individual layer stresses are obtained for all the pipe diameters and support conditions considered.

In addition to predictions of the average overall and individual layer stress patterns, the variation of longitudinal stress (S_{xx}), hoop stress (S_{yy}) and inplane shear stress (S_{xy}) with pipe thickness for the three systems modelled was also considered at selected nodes and elements. Examples of the S_{xx} and S_{yy} plots can be seen in figs. 7.20 and 7.21 with the variations with thickness being purely due to shell bending in the pipe when the load is applied. This has already been discussed in chapter 7, along with the possible significance of the S_{xy} against thickness plots (see fig. 7.22).

These plots are interesting because they may be used to predict the order of delamination. This has already been thoroughly discussed in chapter 7, with the central layers being predicted as the most likely to delaminate due to the highest difference in shear stresses between adjacent layers occurring there for both pipe diameters in either support condition. This prediction is backed by experimental evidence in the form of sectioning partially damaged pipes. Fig. 6.14 reveals that the first layers to delaminate for the floor-supported small diameter pipes are the central layers, in complete agreement with the above prediction. Agreement was also found for the large diameter floor-supported pipes and the small diameter cradled pipes.

Overall, NISA2 has proved a very useful tool for modelling this particular geometry, with very good predictions of deformation obtained.

8.4-3. Dynamic analysis.

Five different systems were used for the dynamic analysis (see fig. 7.23) and each will be discussed here in turn.

Considering how simple model A is (illustrated in fig. 7.23b and characterised by equation 7.2), it gives a very good first approximation to experimental behaviour. This is particularly true for the floor-supported specimens (see fig. 7.24), where the predicted values of maximum force and half period agree very well except when specimens with uneven cross-sections are used (e.g. IP5 and S10) or when there is interference in the velocity/time history caused by the impact mechanism (see table 7.6). The latter has caused considerable problems in data gathering, particularly in obtaining the experimental $T_{\frac{1}{2}}$ values. It is suggested that in any further work, the design of the single bounce mechanism takes this into account. However, enough data was available here to allow the general trends for each model to be considered. Use of model A proved less accurate when characterising the behaviour of the cradled specimens (see table 7.6 and fig. 7.25). This is probably due to the very high average k values for the cradled specimens, which cause over prediction when fully damaged specimens are considered.

If the latter is the case, then allowing k to vary as the slope of the force/displacement curve varies (i.e. by introducing a non-linear k) will improve prediction. This approach was used previously with some success by Christoforou et al (33) and did allow the tail of the force/time curve to be very well predicted here (see fig. 7.26). This is the strength of this version of model A and results in improved prediction of the half period, particularly for the full damaged cradled specimens (see table 7.7). The maximum force is also better predicted, generally, using this version of the model.

Model B was used primarily in an attempt to predict the period of oscillation, T_n, of the pipe. The first version of this model (illustrated in fig. 7.23c and characterised by equation 7.3) considered the pipe as the effective mass of a beam and did not predict T_n very well, particularly in the fully damaged cases for both support conditions (see table 7.8). The model was then modified to represent a ring undergoing flexural vibrations (see fig. 7.23d). Considering a composite ring, T_n was predicted to be 0.34ms. This is an improvement on the beam model, but is still not very close to the experimental values. A final attempt at increasing the accuracy was made by considering the pipe to be a resin ring. This resulted in a T_n value of 0.58ms, which is a slight improvement.

Overall, it can be seen that the experimental values of T_n lie between the two models - beam and ring - with the pure resin ring model being closest to the experimental values. This indicates that the pipe itself is undergoing a mixture of beam and ring flexural vibration modes under impact, with its behaviour dominated by the ring mode. As already noted, superimposing the oscillations onto the initial rising ramp has proved less than successful for all three versions of model B (see figs. 7.27 and 7.28a and b).

However, despite the disadvantages mentioned here, behaviour has been well characterised by these two simple models A and B and prediction has been improved by considering simple variations i.e. by using a non-linear force constant in model A and by considering a ring and not a beam in model B.

9. CONCLUSIONS AND SUGGESTIONS FOR FUTURE WORK.

The tests and modelling carried out in this work have allowed the failure process of the specimens to be very well defined. All complete pipes and pipe sections tested either statically or impacted and in either the floor-supported or cradled support condition undergo a very localised first failure.

Use of strain gauges has allowed this failure to be studied and it is now known to be due to local crush, which causes the resin to yield. This acts as a precursor to delamination initiation. The first failure produced very localised damage which does not appear significant but tests have shown that it has a very significant effect on the pipe strength in the floor-supported condition, reducing it suddenly to a load which remains constant despite increasing amounts of damage. After this first failure, delamination growth continues very slowly, with the specimens undergoing second failure or reaching a peak load, depending on their geometry. Although these tests were conducted statically, they do give an indication to dynamic behaviour, since if equivalent impact tests are performed, damage of a similar nature is obtained.

One of the major aims of the project was to assess if it was possible to model impact behaviour with static behaviour for complete pipes in the two support conditions. Analysing the damage caused by backlighting and by sectioning, and performing the residual property tests revealed that this is possible for the cradled support condition over the majority of the energy range considered. However, when the pipe is not restrained in the cradles (i.e. is floor-supported), the pipe deforms transversely to different degrees depending on whether it is being statically tested or impacted. This results in the two test types not being equivalent and thus static behaviour cannot be used to model impact behaviour for this support condition.

A second point considered to facilitate characterisation of the pipe's impact behaviour was to perform static tests on pipe sections and use these to model impact behaviour. For the cradled case, residual property tests for very small pipe sections revealed similar trends to those for the complete pipes and so this is a distinct possibility. However, not enough work has been carried out here to draw any solid conclusions and this is suggested as an area for future development. A further experimental area for future work is to perform a series of drop weight tests on the large diameter pipes to assess if there are any differences between these and the pipe drop tests already conducted. Further to this, it would be interesting to perform cradled tests - both static and impact - on the large diameter pipes since the support conditions are seen to have a significant effect on the failure loads, residual properties and extent of damage in loaded pipes. Further consideration of these effects is required when considering the installation of such pipes in off-shore and marine top-side situations where low velocity impacts readily occur.

All three modelling systems carried out in this project have proved successful, with the deflection at first failure being well predicted by a simple analytical solution and by finite element modelling with the NISA2 package for all pipe diameters and support conditions. The latter has also proved very useful in modelling stress behaviour at first failure and may have produced a means of predicting between which layers delamination is likely to occur. The finite element model can therefore be expected to predict the mechanical behaviour of such pipes in more complex loading conditions. It is suggested that, if time is available, the system be refined to use solid brick elements to look more closely at the behaviour at the layer interfaces with special reference to obtaining the through-the-thickness shear stresses. Dynamic analysis has involved two very simple mass/spring models (with several slight variations), which have worked well in predicting the impact response of the pipes.

Overall, the work conducted in this project has characterised the failure process, provided three successful means of numerical modelling and indicated that it is possible for static tests to be used to model impact behaviour for the cradled support condition. Simplifying the experimental work further by performing static tests on sections of pipes and using scaling factors to predict behaviour may also be possible for the cradled condition and this is strongly recommended for future development.

Having identified the types of failure mechanism and how they affect the residual properties future work should include the consideration of different resin systems to reduce the area or number of delaminations. It is obviously a disadvantage to have a situation where there is very little, if any, obvious surface damage to the pipe, masking significant areas of delamination beneath. Work should therefore be considered that examines the new surface coatings that indicate the possibility of internal delamination by showing more obvious, pronounced surface crush damage.

APPENDIX. PROGRAM TO GATHER STRAIN DATA.

```
10  !THIS PROGRAM IS DESIGNED TO MEASURE THE  STRAIN FROM
20  !A PIPE UNDER TRANSVERSE COMPRESSION STATIC TESTING
30  OPTION BASE 1
40  GOSUB Init
50  GOSUB Setplot
60  T0=TIMEDATE
70  GOSUB Meas
80  GOSUB Plo
90  GOSUB Data1
100 GOTO 70
110 STOP
120 Init:  !SUBROUTINE TO INITIALISE LOGGER AND VARIABLES
130        DEG
140        OUTPUT 709;"RST"
150        OUTPUT 709;"REAL STR_REF(12)"
160        OUTPUT 709;"USE 0"
170        OUTPUT 709; "CONFMEAS STRUN, 100-109, 200-201,
180        INTO STR_REF"
190        OUTPUT 709;"CONFMEAS DCV,300,303"
200        ENTER 709;Iload,Idisp
210        DIM Str1(12),Name$[15],Data_var$(2000)[160]
220        N=1
230        INPUT "PLEASE INPUT DATA FILE NAME" ,Name$
240        CREATE ASCII Name$&":,1500,2",400
250        ASSIGN @Path TO Name$
260        RETURN
270 Setplot:   !SUBROUTINE TO SET UP THE SCREEN PLOT
280            GRAPHICS ON
```

```
290             GINIT
300             GCLEAR
310             VIEWPORT 20,110,20,80
320             WINDOW 0,50,-15000,15000
330             FRAME
340             AXES 1,1000,0,0,10,5
350             CLIP OFF
360             FOR I=10 TO 50 STEP 10
370             MOVE I,0
380             LORG 6
390             CSIZE 3.5
400             LABEL I
410             NEXT I
420             FOR I=-15000 TO 15000 STEP 5000
430             MOVE 0,I
440             LORG 8
450             LABEL I
460             NEXT I
470             MOVE 25,-1000
480             LORG 6
490             LABEL "LOAD (kN)"
500             MOVE -1,25000
510             LABEL "STRAIN (us)"
520             RETURN
530 Meas:           !SUBROUTINE TO TAKE STRAIN MEASUREMENT
540                 OUTPUT 709;"CONFMEAS STRQ,100,109.200-
550                 201,REF STR_REF,GF2E-6
560                 ENTER 709;Str1(*)
570                 OUTPUT 709;"CONFMEAS DCV,300,303"
```

```
580                  ENTER 709;Load,Disp
590                  T3=TIMEDATE-T0
600                  RETURN
610 Plo:                 !SUBROUTINE TO PLOT  THE DATA FROM
620                      !THREE GAUGES
630                      PEN 2
640                      PLOT -(Load-Iload)*5,Str1(7)
650                      PEN 3
660                      PLOT -(Load-Iload)*5,Str1(9)
670                      PEN 6
680                      PLOT -(Load-Iload)*5,Str(11)
690                      RETURN
700 Data1:                   !SUBROUTINE TO STORE DATA
710                          L=(Load-Iload)*5
720                          D=(Disp-Idisp)*2
730                          OUTPUT Data_var$(N) USING "X,
740                          2D.2D,X,2D.2D,X,12(S2D.2DE,X),
750                          X,4D,X,4D";L,D,Str1(*),T3,N
760                          N=N+1
770                          ON KEY 0 LABEL "STOP" GOTO Fin
780                          IF N=2000 THEN GOTO Fin
790                          RETURN
800 Fin:                         !SUBROUTINE  FOR  DATA
810                              !STORAGE
820                              OUTPUT @Path;Data_var$(*)
830                              ASSIGN @Path TO *
840              END
```

REFERENCES

1. Grim, G.C.: "Shipboard experience with GRP pipes in Shell fleet vessels", The second International Conference on Polymers in a Marine Environment, Oct. 1987, Institute of Marine Engineers, (1988).

2. "New profiles", Shell World, (Feb. 1988), p10-14.

3. Guiton, J.: "An all-GRP piping, support and walkway system for tanker weather deck applications", The second International Conference on Polymers in a Marine Environment, Oct. 1987, Institute of Marine Engineers, (1988).

4. Cooper, L.T.: "Development, manufacture and applications of glass reinforced plastic pipes", Anti-Corrosion Methods and Materials, v25, n2, p3-10, (1978).

5. Wavin Repox B.V., JC Kellerlaan 3, PO Box 5, 7770 AA Hardenberg, The Netherlands.

6. Rolston, J.A.: "Fiberglass composite materials and fabrication processes", Chemical Engineering (New York), v87, (Jan. 28 1980), p96-110.

7. Lee, H. and Neville, K.: "Handbook of Epoxy Resins - Chapter 2: An Introduction to Epoxy Resins", p1-8, (1967), McGraw-Hill, NY.

8. Haddad, G.N.: "Recent innovations in PVC-FRP composite pipes" 32nd Annual Technical Conference (1977) Reinforced Plastics/Composites Institute, section 5-F, p1-12.

9. Marks, P.R.: "The fire endurance of glass-reinforced epoxy pipes", The second International Conference on Polymers in a Marine Environment, Oct. 1987, Institute of Marine Engineers, (1988).

10. Sjöblom, P.O., Hartness, J.T. and Cordell, T.M.: "On low-velocity impact testing of composite materials", J. Comp. Mat., Vol 22, (Jan 1988), p30 -52.

11. Caprino, G., Crivelli Visconti, I. and Di Ilio, A.: "Composite materials response under low velocity impact", Composite Structures, Vol 2, (1984), p261-271.

12. Sharma, A.V.: "Low velocity impact tests on fibrous composite sandwich structures", Test Methods and Design Allowables for Fibrous Composites ASTM STP 734, Chamis,C.C. (ed.), American Society for Testing and Materials, 1981, p54-70.

13. Novak, R.C. and DeCrescente, M.A.: "Impact behaviour of unidirectional resin matrix composites tested in the fibre direction", Comp. Mat.: "Testing and Design (2nd Conference), ASTM STP 497, American Soc. for Testing and Materials, (1972), p311-323.

14. Yeung, P. and Broutman, L.J.: "The effect of glass-resin interface strength on the impact strength of fiber reinforced plastics", Polymer Engineering and Science, (Mid-Feb 1978), Vol 18, No 2, p62-72.

15. Chamis, C.C., Hanson, M.P. and Serafini, T.T.: "Impact resistance of unidirectional fiber composites", Comp. Mat.: Testing and Design (2nd Conference), ASTM STP 497, American Society for Testing and Materials, (1972), p324-349.

16. Therberge, J.E. and Hall, N.T.: "Impact behaviour of glass fortified thermoplastic", Modern Plastics, Vol 46, (1969), No 7, p114-127.

17. Vincent, P.I.: "Testing for brittle fracture", Trans. Plast. Inst., Vol 30, No 87, (June 1962) p157-164.

18. Dorey, G.: "Impact damage in composites - development, consequences and prevention", ICCM6/ECCM2, Vol 3, Elsevier Applied Science, (1987), p3.1-3.26.

19. Broutman, L.J. and Rotem, A.: "Impact strength and toughness of fiber composite materials", Foreign Object Damage to Composites, ASTM STP 568, (1975), p114-133.

20. Boll, D.J., Bascom, W.D., Weidner, J.C. and Murri, W.J.: "A microscopic study of impact damage of epoxy-matrix carbon-fibre composites", J. Mat. Sci., Vol 21, (1986), p2667-2677.

21. Cantwell, W.J. and Morton, J.: "Detection of impact damage in CFRP laminates", Composite Structures, Vol 3, (1985), p241-257.

22. Cantwell, W.J., Curtis, P.T. and Morton, J.: "An assessment of the impact performance of CFRP reinforced with high-strain carbon fibres", Composite Science and Technology, Vol 25, No 2, (1986), p133-148.

23. Caprino, G.: "Residual strength prediction of impacted CFRP laminates", J. Comp. Mat., Vol 18, (Nov 1984), p508-518.

24. Dorey, G., Sidey, G.R. and Hutchings, J.: "Impact properties of carbon fibre/Kevlar 49 fibre hybrid composites", Composites, Vol 9, (Jan 1978), p25-32.

25. Verpoest, I., Marien, J., Devos, J. and Wevers, M.: "Absorbed energy, damage and residual strength after impact of glass fibre epoxy composites", ICCM6/ECCM2, Vol 3, (1987), p3.485-3.493.

26. Myers, F.A.: "Impact response of SMC/BMC composites", 37th Annual Conf. Reinforced Plastics/Composites Institute, SPI, Part 1-C, (Jan 1982), p1-12.

27. Rotem, A.: "Residual flexural strength of FRP composite specimens subjected to transverse impact loading", SAMPE Journal, (March/April 1988), p19-25.

28. BSI: BS 5480 "Specification for glass fibre reinforced (GRP) pipes and fittings for use for water supply or sewage : Part 2 Design and Performance Requirements" (1982).

29. ASTM D2444-80 "Standard test method for impact resistance of thermoplastic pipe and fitting by means of a tup (falling weight)".

30. Cann, J.M.: "The assessment of impact resistance of rigid PVC pipes - part 1", British Plastics, (1963), Vol 36, Part 9, p516-521.

31. Cann, J.M.: "The assessment of impact resistance of rigid PVC pipes - part 2", British Plastics, (1963), Vol 36, Part 10, p579-582.

32. Lloyd, B.A. and Knight, G.K.: "Impact damage sensitivity of filament-wound composite pressure vessels", JANNAF Meeting, New Orleans LA, (Aug 1986), p7-15.

33. Christoforou, A.P., Swanson, S.R., Ventrello, S.C. and Beckwith, S.W.: "Impact damage in carbon/epoxy composite cylinders", 32nd Annual SAMPE Symposium, (April 6-9 1987), p964-973.

34. Christoforou, A.P. and Swanson, S.R.: "Strength loss in composite cylinders under impact", Transactions of the ASME, Vol 110, (April 1988), p180-184.

35. Joshi, S.P.: "Impact-induced damage initiation analysis: an experimental study", Proc. Amer. Soc. for Composites, (Sept 25-29 1988), p325-333.

36. Malvern, L.E., Sun, C.T. and Liu, D.: "Delamination damage in central impacts at subperforation speeds on laminated Kevlar/epoxy plates", Composite Materials: Fatigue and Fracture, Second Volume, ASTM STP 1012, Paul A. Lagace, Ed, American Society for Testing and Materials, Philadelphia, (1989), p387-405.

37. Sheldon, W.H.: "Non-destructive (NDE) of impact damage in thick graphite composite aircraft structures", SAMPE, Vol 24, Book 1, (1979), p372-376.

38. Maass, D. and Hoon, D.: "Design of composite tubular structures for impact damage tolerance", 30th National Symposium, (March 19-21 1985), p1294-1308.

39. Peraro, J.S.: "Predictions of end-use impact resistance of composites", Instrumented impact testing of plastics and composite materials, ASTM STP 936, S.L. Kessler, G.C. Adams, S.B. Driscoll and D.R. Ireland, Eds, (1987), p187-216.

40. Graves, M.J. and Lagace, P.A.: "Damage tolerance of composite cylinders", SAE Tech Paper Series 830776, (April 1983).

41. Bader, M.G., Harrison, R.P. and Hinton, M.J.: "Deformation and failure of thin walled filament wound GRP tubes subjected to transverse indentation", University of Surrey report.

42. Manders, P.W., Bader, M.G., Hinton, M.J. and Flower, P.Q.: "Mechanisms of impact damage in filament-wound glass-fibre/epoxy resin tubes", Mech. Behav. of Mater., Proc. of the Int. Conf., 3rd (ICM3), v3, Cambridge, Engl., (Aug 20-24 1979).

43. Harrison, R.P. and Bader, M.G.: "Simulated impact damage in filament wound glass-fibre reinforced tubes", University of Surrey report.

44. Hodgkinson, J.M., Vlachos, N.S., Whitelaw, J.H. and Williams, J.G.: "Drop-weight impact tests with the use of laser-doppler velocimetry", Proc. R. Soc. Lond., A379, (1982), p133-144.

45. Ruiz, C. and Mines, R.A.W.: "The Hopkinson pressure bar: an alternative to the instrumented pendulum for Charpy tests", International Journal of Fracture, Vol 29, (1985), p101-109.

46. Ireland, D.R.: "Procedures and problems associated with the reliable control of the instrumented impact test", ASTM STP 563, (1974), p3-29.

47. Baker, A.A., Jones, R. and Collinson, R.J.: "Damage tolerance of graphite/epoxy composites", Composite Structures, Vol 4, (1985), p15-44.

48. Proulx, D., Roy, C. and Zimcik, D.G.: "Assessment of the state of the art of non-destructive evaluation of advanced composite materials", Canadian Aeronautics and Space Journal, v31, part 4, (Dec 1985), p325-334.

49. Henneke, E.G. II and Russell, S.S.: "Impact damage detection and evaluation of active and passive thermography and stereo X-ray radiography in advanced composite panels", 14th Symposium on Non-destructive evaluation, San Antonio USA, (April 1983).

50. Murphy, R.V. and Mitchell, A.B.: "Development of an effective non-destructive examination method to detect lack of bond between mating surface of fiberglass piping", Res. Rep. Can. Electr. Assoc. 85-310G-31, (Jul 1985), 81p.

51. Prakash, R.: "Non-destructive testing of composites", Composites, Vol 11, n4, (Oct 1980) p219-224.

52. Blom, A.F. and Gradin, P.A.: "Radiography" Chapter 1 of Non-destructive testing of fibre-reinforced plastic composites, Vol 1, Ed. John Summerscales, (1987), Elsevier.

53. Rose, J.L. and Shelton, W.: "Composite reliability", ASTM STP 580, (1975), p215-226.

54. Sendeckyj, G.P., Maddux, G.E. and Tracy, N.A.: "Comparison of holographic, radiographic and ultrasonic techniques for damage detection in composite materials", ICCM2, (1978), The Metallurgical Society of AIME, p1037-1056.

55. Maddux, G.E. and Sendeckyj, G.P.: "Holographic techniques for defect detection in composite materials", ASTM STP 696, (1979), p26-44.

56. Hagemaier, D.J. and Fassbender, R.H.: "Non-destructive testing of advanced composites", Materials evaluation, Vol 37, (June 1979), p43-49.

57. Rummel, W.D., Tedrow, T. and Brinkerhoff, H.D.: "Enhanced X-ray stereoscopic NDE of composite materials", AFWAL-TR-80-3053.

58. Stinchcombe, W.W.: "Nondestructive examination of damage accumulation processes in composite laminates", Composites Science and Technology, Vol 25, No 2, (1986), p103-118.

59. Wyrick, D.A. and Adams, D.F.: "Damage sustained by a carbon/epoxy composite material subjected to repeated impact", Composites, Vol 19, No 1, (Jan 1988), p19-27.

60. Elber, W.: "Failure mechanics in low velocity impacts on thin composite plates", NASA-TP-2152, (May 1983), 26p.

61. Stone, D.W. and Clarke, B.: "Nondestructive evaluation of composite structures - an overview", ICCM6/ECCM2, Vol 1, Elsevier Applied Science, (1987), p1.28-1.59.

62. Scott, I.G. and Scala, C.M.: "A review of non-destructive testing of composite materials", NDT International, V15, n2, (April 1982), p75-86.

63. Shelton, C.G. and Marks, P.R.: "Failure of ductile interlayer composites: high resolution X-radiographic examination using an opaque penetrant", J. Mat. Sci. Letters, Vol 7, (1988), p673-675.

64. Caprino, G., Crivelli Visconti, I. and Di Ilio, A: "Elastic behaviour of composite structures under low velocity impact", Composites, Vol 15, No 3, (July 1984).

65. Ross, C.A., Malvern, L.E., Sierakowski, R.L. and Takedo, N.: "Finite-element analysis of interlaminar shear stress due to local impact", Recent Advances in Composites in the United States and Japan, ASTM STP 864, J.R. Vinson and M. Taya, Eds., American Society for Testing and Materials, Philadelphia, (1985), p355-367.

66. Cristescu, N., Malvern, L.E. and Sierakowski, R.L.: "Failure mechanism in composites impacted by blunt-ended penetrators", Foreign Object Impact Damage to Composites, ASTM STP 568, (1975), p159-172.

67. Gosse, J.H. and Mori, P.B.Y.: "Impact damage characterization of graphite/epoxy laminates", Proc. Amer. Soc. for Composites 3rd Conference, (25-29 Sept, 1988), p344-353.

68. Tiu, W.P., Gott, J. and Breckell, T.H.: "Residual static strength prediction of impacted composite laminates", CAD in Composite Material Technology, p337-359.

69. Kliger, H.S., Forristall, G.Z. and Vinson, J.R.: "Stresses in circular cylindrical shells of composite materials subjected to localized loads", AF-AFOSR-TR-73-0494, (1973).

70. Chao, C.C., Tung, T.P. and Lee, S.C.: "Response of orthotropic shells subjected to impact loadings", Advanced Composite Materials and Structures, (19-23 May '86), p705-716.

71. Chang, F.K. and Kutlu, Z.: "Mechanical behaviour of cylindrical composite tubes under transverse compressive loads", 32nd International SAMPE Symposium, (April 6-9 1987), p698-707.

72. Chang, F.K. and Kutlu, Z.: "Strength and response of cylindrical composite shells subjected to out-of-plane loadings", J. Comp. Mat., Vol 23, (Jan '89), p11-31.

73. Christoforou, A.P., Swanson, S.R. and Beckwith, S.W.: "Lateral impact of composite cylinders", Composite Materials: Fatigue and Fracture, Second Volume ASTM STP 1012, Paul A. Lagace, Ed, American Society for Testing and Materials, Philadelphia (1989), p373-386.

74. Hoa, S.V., Yu, C.W. and Sankar, T.S.: "Analysis of filament wound vessel using finite elements", Composite Structures, Vol 3, (1985), p1-18.

75. NISA2, Engineering Mechanics Research Corporation, 1707, W. Big Beaver, Troy, MI 48084, USA.

76. "NISA2/DISPLAY2 - A family of general purpose finite element programs for pc, mini, supermini, mainframe and super computers", Finite Element News, Issue no. 5, (Oct. 1987), p64-69.

77. Kothawala, K.S.: "NISA2/DISPLAY2 - The largest fully integrated family of general purpose finite element programs for pc, mini, supermini, mainframe and super computers", Finite Element News, Issue no. 4, (Aug. 1988), p5-11.

78. Cervenka, A. and Marks, P.R.: "The effect of the stacking sequence on tensile properties of PEEK/carbon fibre laminates", 6th Annual Meeting of the Polymer Processing Society (Composite section), Nice, France, (April 17-20 1990).

79. Marks, P.R.: private communication, Shell research Ltd., Thornton Research Centre, PO Box 1, Chester.

80. "Benchmark", newsletter of National Agency for Finite Element Methods and Standards, National Engineering Laboratory, Glasgow (Oct. 1989).

81. Shivakumar, K.N., Elber, W. and Illg, W.: "Prediction of impact force and duration due to low-velocity impact on circular composite laminates", ASME J. of Applied Mechanics, Vol 19, (1985), p674-680.

82. Suaris, W. and Shah, S.P.: "Inertial effects in the instrumented impact testing of cementitious composites", Cement, Concrete and Aggregates, Vol 3, No 2, (1981), p77-83.

83. McQuillen, E.J., Gause, L.W. and Llorens, R.E.: "Low velocity transverse normal impact of graphite epoxy composite laminates", J. Comp. Mat., Vol 10, (1976), p79-91.

84. Liu, D.: "Impact-induced delamination - a view of bending stiffness mismatching", J. Comp. Mat., Vol 22, (July 1988), p674-691.

85. Rotem, A: "The strength of laminated composite materials under repeated impact loading", J. Composites Technology and Research, Vol 10 (No 2), (Summer 1988), p74-79.

86. Fernando, G.: private communication, University of Bath.

87. BSI: BS 2782 Plastics: Part 10 Glass reinforced plastics: Method 1005 Determination of flexural properties - three point method.

88. Ainsworth, K.L. and Evans, K.E.: "Transverse impact of filament-wound pipes", Composite Structures 5, Elsevier, (1989), p333-345.

89. Ainsworth, K.L. and Evans, K.E.: "The measurement and modelling of filament wound pipes undergoing transverse impacts", Proc. 4th International Conference on Fibre Reinforced Composites, Inst. Mech. Eng., (1990), p143-148.

90. Roark and Young: "Formulas for stress and strain", 5th Edn, (1975), Table 31, No 8, p495.

91. Wavin Repox B.V.: "Engineering guide for Wavistrong filament wound epoxy pipe and fittings", Table 11-h, p8, (1987).

92. Timoshenko, S., Young, D.H. and Weaver, W. Jr.: "Vibration problems in engineering", Chapter 5, Wiley and Sons, (1974), p476-481.